UNIVERSITY OF VERONA

DEPARTMENT OF COMPUTER SCIENCE

DOCTORAL PROGRAM IN COMPUTER SCIENCE

XXXVIII cycle (2022)

DOCTORAL THESIS

A NOVEL REPRESENTATION TO REDUCE COMPLEXITY IN TRACTOGRAPHY

S.S.D. IBIO-01/A

PhD Candidate
Ilaria Gabusi

Ilaria Gabusi

PhD Supervisor
Prof. Alessandro Daducci

PhD Coordinator
Prof. Umberto Castellani

Thesis Reviewers
Prof. Kurt Schilling
Vanderbilt University
Medical Center, USA

Prof. Dogu Baran Aydogan
University of Eastern Finland, FI

Examination Committee
Prof. Chiara Maffei
Massachusetts General Hospital and
Harvard Medical School, USA

Prof. Alberto De Luca
UMC Utrecht, NL

Contents

Acronyms

3D three-dimensional.

ACT Anatomically Constrained Tractography.

AD Axial Diffusivity.

ADC Apparent Diffusion Coefficient.

CHARMED Composite Hindered and Restricted Model of Diffusion.

CNS Central Nervous System.

COMMIT Convex Optimization Modeling for Microstructure Informed Tractography.

CSD Constrained Spherical Deconvolution.

CSF Cerebrospinal Fluid.

CV Coefficient of Variation.

DCT Discrete Cosine Transform.

dMRI Diffusion-weighted Magnetic Resonance Imaging.

dPDF diffusion Probability Density Function.

DTI Diffusion Tensor Imaging.

FA Fractional Anisotropy.

FLAIR Fluid-Attenuated Inversion Recovery.

FN False Negative.

FOD Fiber Orientation Distribution.

FP False Positive.

GM Gray Matter.

GT Ground Truth.

HARDI High-Angular-Resolution Diffusion Imaging.

HCP Human Connectome Project.

iFOD2 second-order integration over FODs.

ISBI International Symposium on Biomedical Imaging.

LiFE Linear Fascicle Evaluation.

MCMC Markov-Chain Monte Carlo.

MD Mean Diffusivity.

MRI Magnetic Resonance Imaging.

MTsat Magnetization Transfer Saturation.

MVF Myelin Volume Fraction.

MWF Myelin Water Fraction.

MySD Myelin Streamline Decomposition.

NMR Nuclear Magnetic Resonance.

NNLS Non-Negative Least Squares.

NODDI Neurite Orientation Dispersion and Density Imaging.

NOS number of streamlines.

ODF Orientation Distribution Function.

PGSE Pulsed-Gradient Spin Echo.

PNS Peripheral Nervous System.

PTT Parallel Transport Tractography.

QBI Q-ball Imaging.

RD Radial Diffusivity.

RF Radio Frequency.

RMSE Root Mean Squared Error.

ROI Region of interest.

SD Spherical Deconvolution.

SET Surface-Enhanced Tractography.

SH Spherical Harmonics.

SIFT Spherical-deconvolution Informed Filtering of Tractograms.

SMT Spherical Mean Technique.

SNR Signal-to-Noise Ratio.

TE Echo Time.

TP True Positive.

TR Repetition Time.

WM White Matter.

List of Figures

Chapter 1

Introduction

Understanding the structural organization of the *human brain* is a fundamental goal in neuroscience. White matter forms the communication architecture of the brain, connecting gray matter areas through a complex wiring of axonal fibers. Mapping these pathways *in vivo* provides essential insight into how information is integrated and transferred across brain regions, as well as how these processes are altered in neurological disorders. Among non-invasive imaging techniques, *Diffusion Magnetic Resonance Imaging* has become the most powerful tool for investigating brain microstructure and connectivity. This particular magnetic resonance signal reflects the random motion of water molecules, providing information about the underlying tissue geometry and allowing the inference of fiber orientations, as well as the reconstruction of large-scale anatomical connections through tractography.

Tractography algorithms estimate the trajectories, called streamlines, of white matter fiber bundles by following the dominant diffusion directions derived from the local signal. Over the past two decades, tractography has revolutionized neuroimaging research, enabling the in vivo exploration of brain connectivity and the investigation of its relationship with function, cognition, and disease. However, despite these advances, tractography remains an indirect and model-dependent technique, as it infers pathways from estimated orientations rather than directly visualizing axons. As a result, it is sensitive to noise, algorithmic choices, and acquisition parameters. Several methodological *limitations* still constrain the anatomical and quantitative reliability of tractography. Among these, there is a lack of biological specificity because streamlines represent simplified geometric entities that do not exactly correspond to real axonal bundles in the brain. Moreover, to ensure the recovery of true positive trajectories, tractography pipelines typically generate tractograms with millions of streamlines, introducing substantial redundancy that creates computational problems and increases storage requirements, besides making it difficult to interpret the results. This is further complicated by high algorithmic variability, meaning that distinct tracking methods and parameter choices often yield unreliable reconstructions. Indeed, even starting with the same data, they provide very different estimates. Finally, there is the issue of quantification, as the number of streamlines connecting two regions does not directly reflect the strength or density of the underlying anatomical connections.

To move toward a more quantitative interpretation of the reconstructions, recent research has focused on integrating tractography with microstructural models of the diffusion signal. This has led to the emergence of *microstructure informed tractography*, in which each streamline is associated with a quantitative weight reflecting its contribution to the measured signal. One of the most representative and flexible frameworks in this family is the Convex Optimization Modeling for Microstructure Informed Tractography (COMMIT), which formulates the tractography quantification problem as a global optimization. By estimating the combination of streamline contributions that best explains the acquired diffusion data, COMMIT provides a biophysically grounded estimation of structural connectivity. Although these approaches represent a significant step forward in the quantification of tractography reconstructions, they also face important computational and conceptual challenges. The total number of streamlines produced by whole-brain tractography results in large and redundant linear systems that are difficult to manage efficiently. Moreover, streamlines are still treated as one-dimensional entities with constant properties along their path, overlooking the spatial uncertainty of real white matter bundles. These limitations, together with the high algorithm- and parameter dependency, motivate the development of new techniques capable of linking the geometry of tractography with the acquired diffusion signal in a compact and robust manner.

The central objective of this thesis is to introduce and exploit a new way of representing tractography reconstructions: the *blurred streamlines representation*. When many millions of pathways are generated to avoid false negatives, the resulting high level of redundancy among streamlines translates into collinearity in the linear systems used by microstructure informed tractography formulations, potentially biasing the estimation of microstructural properties. To address this issue, clustering is employed to identify and remove streamlines that are highly similar to one another. Then, instead of treating the remaining centroids as simple polylines in three-dimensional space, the proposed approach reformulates the notion of a streamline by assigning it a spatial extent through a blurring function. This effectively transforms the streamline from an infinitesimally thin trajectory into a spatially extended structure that captures the collective contributions of neighboring fibers. This concept provides a unified and computationally efficient foundation for developing new tractography methods that are more robust, anatomically consistent, and quantitatively meaningful. The first part of the thesis (Chapter 3) presents the theoretical formulation and validation of the blurred streamlines representation on both synthetic and in vivo data, demonstrating its ability to drastically reduce redundancy while preserving anatomical detail and improving numerical stability.

Building on this foundation, the second part of the thesis (Chapter 4) introduces a novel approach that leverages the blurred streamlines representation to combine tractograms generated by different tracking algorithms and let them work in synergy with the aim of reducing the considerable variability present in reconstructions obtained from the same data. By incorporating the strengths of individual methods and compensating for their specific biases, this method yields a unified tractogram that more accurately reflects the underlying anatomy, thereby enhancing the robustness of structural connectivity estimates. The final part of the thesis (Chapter 5) explores how the computational efficiency and flexibility of the blurred streamlines representation enable more advanced developments, including an adaptive global tractography method and new extensions of COMMIT for modeling pathological conditions such as diffuse axonal degeneration.

Overall, this thesis aims to address key limitations of current tractography by bridging the gap between local diffusion signal modeling and global white matter architecture. Through the introduction of the blurred streamlines representation and its derived applications, the work contributes to the development of a more quantitative, biologically grounded, and computationally efficient framework for studying brain connectivity in both health and disease.

Chapter 2

Background

2.1 Overview of the human brain

The *brain* is one of the most complex and efficient structures in biology and regulates virtually all functions of the human body (Hofman, 2014). Together with the spinal cord, it forms the Central Nervous System (CNS), which is capable of transforming external stimuli into sensations, generating movement, and supporting higher cognitive functions such as memory, reasoning, and communication (Colom et al., 2010; Wickens, 2014). The CNS is complemented by the Peripheral Nervous System (PNS), which connects the brain and spinal cord to the rest of the body through nerves and receptors, mediating both sensory input and motor output (Purves et al., 2004). Despite major advances in neuroscience, much about its organization remains unclear, although rapid progress continues thanks to new technologies and methods (Fan, 2021).

The nervous system contains a wider variety of cell types than any other organ system (Purves et al., 2004). Its primary units are *neurons*, specialized for the transmission of electrical signals over long distances through action potentials. A typical neuron consists of a cell body (soma), dendrites, and an axon, as illustrated in Figure 2.1 (Rockland, 2002). The *soma* contains the nucleus and most cell's organelles. *Dendrites* arise from it, forming an elaborate branching structure that receives input from other neurons.

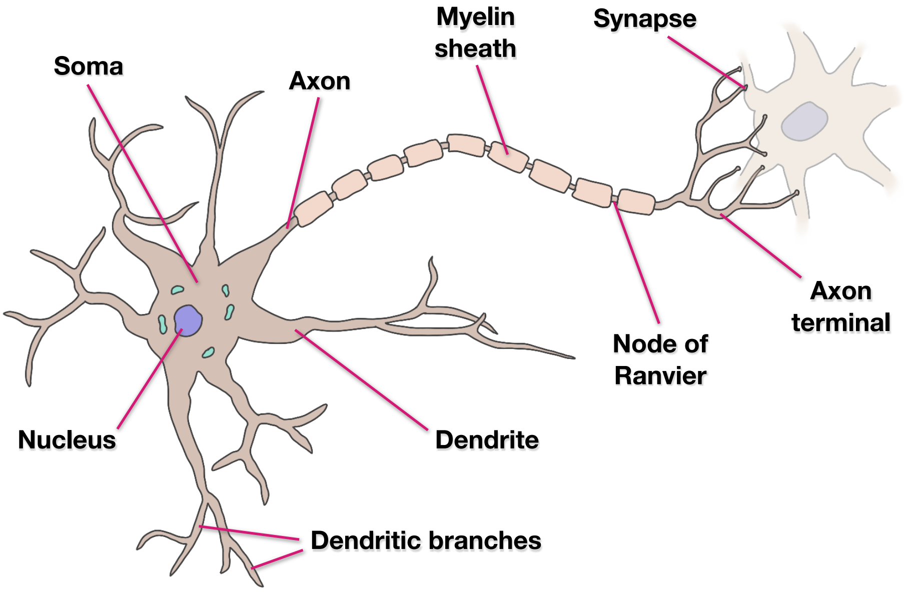

Figure 2.1: Schematic representation of a typical neuron. Dendrites receive inputs, the soma integrates them, and the axon transmits the signal. Myelin sheaths, formed by glial cells, speed up conduction and are interrupted at the nodes of Ranvier.

Communication occurs at synapses, where, without actual physical contact, neurotransmitters released by one cell bind to receptors on the postsynaptic cell (Purves et al., 2004). The *axon* is a single extension responsible for signal conduction. It can reach distant target cells, sometimes elongating up to tens of centimeters. Many axons are wrapped by a *myelin* sheath, formed by oligodendrocytes in the CNS and Schwann cells in the PNS. Myelin, being an insulating material, greatly increases conduction speed by enabling saltatory propagation between the nodes of Ranvier, where myelination is interrupted, and action potentials are regenerated (Fields, 2010). Alongside neurons, the brain contains abundant *glial cells*. Glia do not generate action potentials but support and modulate neuronal activity. They help maintain the ionic environment, regulate neurotransmitter uptake, support recovery after injury, and contribute to immune defense. The main types are astrocytes, oligodendrocytes, and microglia, which together outnumber neurons in the human brain (Purves et al., 2004).

At the tissue level, brain regions are broadly classified as Gray Matter (GM) and White Matter (WM), as shown in Figure 2.2. GM is composed of neuronal cell bodies, dendrites, unmyelinated axons, glia, and capillaries, and is responsible for information processing and integration. It is found in the cerebral and cerebellar cortices as well as in deep subcortical nuclei (Purves et al., 2004). In contrast, WM consists mainly of myelinated axons, which give it its characteristic pale color and form the communication infrastructure linking distant GM regions (Fields, 2010). When axons follow common trajectories, they form WM fiber bundles or tracts. As illustrated in Figure 2.3, these tracts can be classified as *association fibers*, which connect cortical regions within the same hemisphere (e.g., the Arcuate Fasciculus); *commissural fibers*, which link homologous regions across hemispheres (e.g., the Corpus Callosum); and *projection fibers*, which connect the cortex to deeper GM structures and the spinal cord (e.g., the Corticospinal Tract) (Catani and Thiebaut de Schotten,

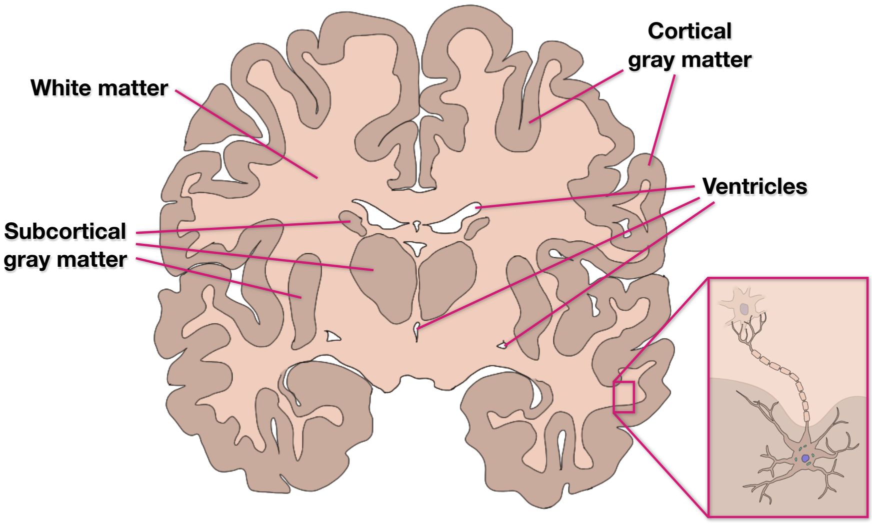

Figure 2.2: Coronal section of the brain showing Gray Matter (GM, darker), White Matter (WM, lighter), and ventricles filled with Cerebrospinal Fluid (CSF). GM (both cortical and subcortical) contains neuronal cell bodies and dendrites, while WM consists mainly of myelinated axon tracts connecting distant regions.

2012; Wycoco et al., 2013).

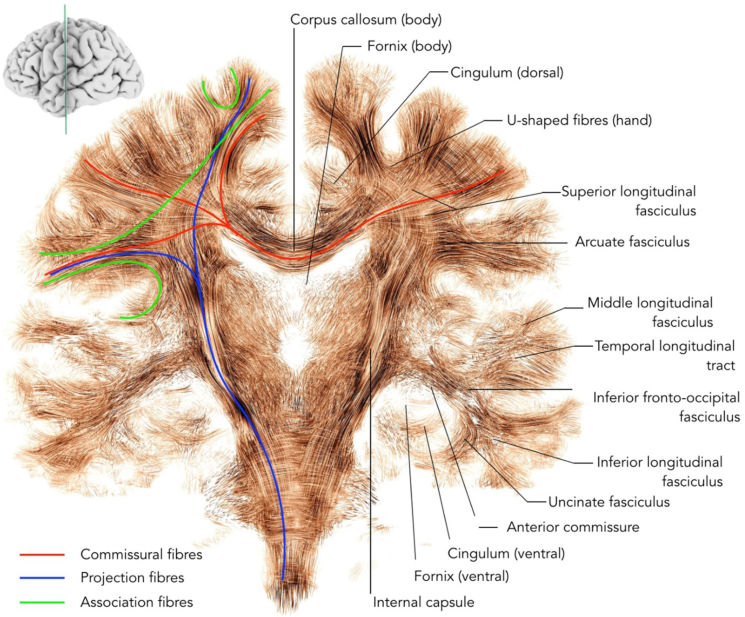

Figure 2.3: Classification of WM fibers and major tracts. Association fibers connect regions within the same hemisphere, commissural fibers link homologous regions across hemispheres, and projection fibers connect the cortex to deeper GM structures and the spinal cord. From (Catani, 2025)

The CNS is anatomically subdivided into the cerebral hemispheres, diencephalon, cerebellum, brainstem (midbrain, pons, and medulla), and spinal cord (Purves et al., 2004). The cerebrum is the largest component and is organized into two hemispheres. Each hemisphere is folded into gyri and sulci that increase the cortical surface area. The cerebral cortex is traditionally divided into four main *lobes*: frontal, parietal, temporal, and occipital, shown in Figure 2.4. These subdivisions are associated with distinct but interconnected sensory, motor, and cognitive functions (Gray and Lewis, 1918). The CNS is further protected by three meningeal layers: dura mater, arachnoid mater, and pia mater. The subarachnoid space between the latter two contains Cerebrospinal Fluid (CSF), which cushions the brain and circulates through the ventricular system (Purves et al., 2004).

The interaction between local GM processing and long-range WM con-

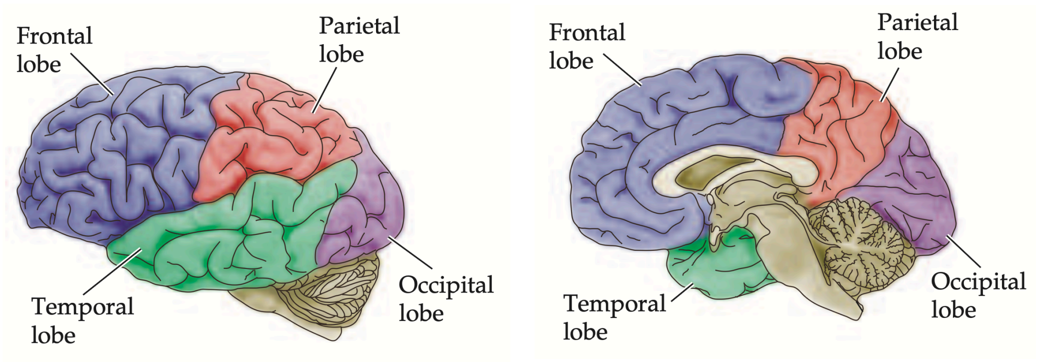

Figure 2.4: Anatomical organization of the cerebral cortex into lobes. Two sagittal views (lateral and medial) of the cerebrum showing the four main lobes: frontal, parietal, temporal, and occipital. Adapted from (Purves et al., 2004).

nectivity gives rise to the brain's remarkable functional repertoire, enabling thought, learning, memory, and coordinated behavior (Bassett and Gazzaniga, 2011). This structural organization has long been a central focus of neuroscience: early studies relied on dissections, whereas modern approaches employ non-invasive imaging techniques, such as Magnetic Resonance Imaging, which now allow the study of brain wiring *in vivo* (Jones, 2010b).

2.2 Magnetic resonance imaging

Magnetic Resonance Imaging (MRI) is one of the most powerful non-invasive methods to study brain structure and function in vivo. Its unique strength lies in the fact that the image contrast does not arise from X-ray attenuation or from direct electrical activity, but from the intrinsic physical properties of atomic nuclei, particularly hydrogen protons in water. Because the brain is largely composed of water, MRI provides a highly sensitive tool to explore its architecture and physiology (Berger, 2002; Roberts, 1959).

The foundation of MRI is *Nuclear Magnetic Resonance (NMR)*, a physical phenomenon that occurs when certain elements interact with a magnetic field (Lauterbur, 1973; Mansfield, 1977; Rabi et al., 1938). Specifically, most of the time MRI is employed to detect the resonance of the hydrogen nuclei (protons), which are the most abundant element in human tissues, due to their presence in water and fat. NMR relies on two intrinsic nuclear properties: magnetism and spin angular momentum. *Magnetism* arises from the fact that protons carry charge and generate a tiny magnetic field. In the absence of an external magnetic field, these magnetic moments are randomly oriented. When a strong static magnetic field B_0 is applied, however, they partially align with it, revealing the second property: *spin angular momentum*, analogous to angular momentum in classical mechanics but applying to nuclei with an odd number of protons and neutrons. As shown in Figure 2.5, when placed in B_0 protons precess around B_0's direction at a characteristic frequency, known as the *Larmor frequency*:

$$\omega_0 = \gamma B_0 \, , \tag{2.1}$$

where γ is the gyromagnetic ratio, a nucleus-specific constant.

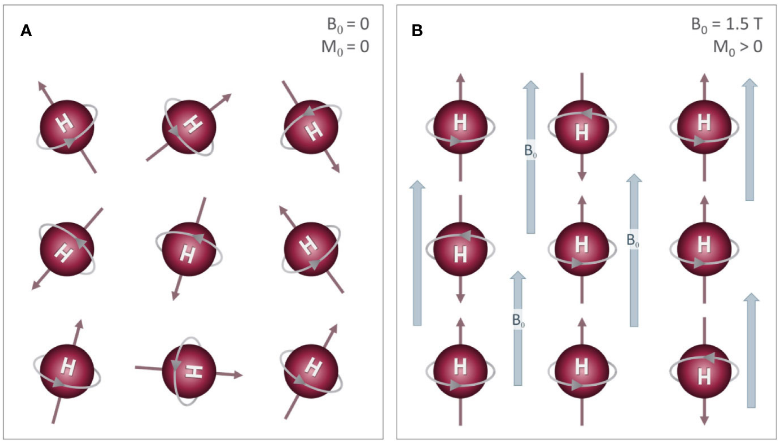

Figure 2.5: Spin alignment and precession under an external magnetic field (B_0). In the absence of B_0, proton magnetic moments are randomly oriented; when the field is applied, they align preferentially parallel to B_0, generating a small net magnetization (M_0). From (Shaffer et al., 2020).

In equilibrium, more spins align parallel (low-energy state) than antiparallel (high-energy state) to B_0, resulting in a small *net magnetization vector* M. This vector is collinear with B_0 and therefore cannot be directly detected.

To measure it, an additional perturbation is required to rotate M away from the longitudinal axis, making it detectable by Radio Frequency (RF) coils. A short RF pulse at the Larmor frequency ω_0 creates a secondary magnetic field B_1 perpendicular to B_0. This temporarily disturbs the equilibrium and flips the net magnetization vector M by 90° into the transverse plane. When the RF pulse is switched off, the system relaxes back to equilibrium, generating a time-varying signal that can be detected by receiver coils. The relaxation of M occurs through two main mechanisms at the same time t:

$$M_z(t) = M\left(1 - e^{-t/T_1}\right), \tag{2.2}$$

$$M_{xy}(t) = M_{xy}(0)e^{-t/T_2}, \tag{2.3}$$

The first, known as *longitudinal or spin-lattice relaxation*, describes the recovery of the longitudinal magnetization (M_z) along B_0 with a time constant T_1. The second, called *transverse or spin-spin relaxation*, describes the loss of phase coherence among spins in the transverse plane (transverse magnetization M_{xy}), leading to signal decay with a time constant T_2 (Grover et al., 2015). These relaxation properties vary across tissues, producing contrast between GM, WM, and CSF (Bitar et al., 2006).

All MRI images contain contributions from both longitudinal (T_1) and transverse (T_2) relaxation, but the differences can be enhanced or minimized by adjusting the *acquisition parameters*, particularly the Echo Time (TE), which defines when the signal is sampled, and the Repetition Time (TR), which defines how frequently the RF excitation is applied. By manipulating TE and TR, it is possible to obtain images with different contrasts. For instance, T_1-weighted images (short TE and short TR) highlight fat-rich tissues and provide excellent anatomical detail, T_2-weighted images (long TE and long TR) emphasize fluid-filled regions, and proton-density (PD)–weighted images (short TE and long TR) are mainly sensitive to the density of hydrogen nuclei and are less commonly used in brain imaging. As shown in Figure 2.6, in the brain, T_1 contrast results in WM appearing brighter than GM, with CSF dark, whereas in T_2 contrast the opposite holds: CSF is bright, GM has higher intensity than WM, and WM appears darkest. A further variant is Fluid-Attenuated Inversion Recovery (FLAIR), in which an additional inversion pulse suppresses the CSF signal, thereby improving the visibility of periventricular lesions such as those found in multiple sclerosis (Bitar et al., 2006).

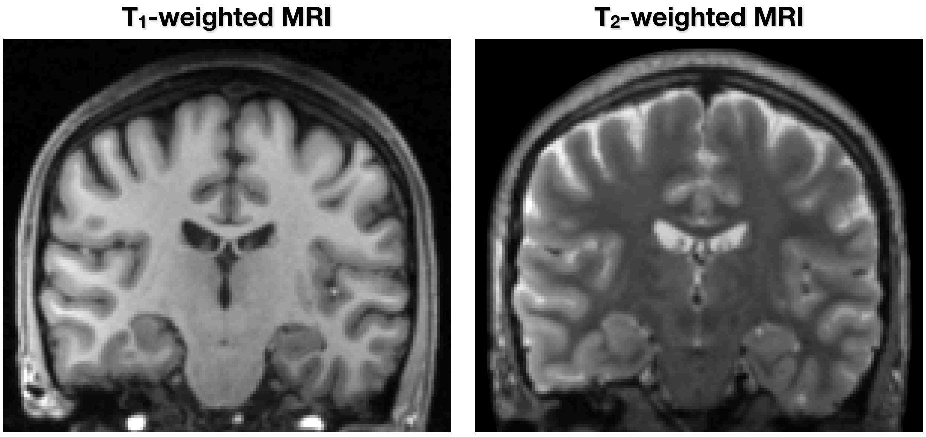

CSF	**Dark**	**Bright**
WM	**Light**	**Dark gray**
GM	**Gray**	**Light gray**
Fat	**Bright**	**Light**

Figure 2.6: Comparison of T_1-weighted and T_2-weighted images. These two MRI contrasts probe different tissue properties. Variations in relaxation times cause differences in signal intensity, allowing tissues such as gray matter, white matter, and cerebrospinal fluid to appear with distinct brightness levels in each image. Data from the FMRIB software library.

In practice, the magnetic field B_0 is never perfectly homogeneous. As a result, adjacent spins precess at slightly different frequencies, leading to a progressive loss of phase coherence in the transverse plane and a faster signal decay. To compensate for this effect, Hahn (1950) introduced the *spin echo* sequence. After the initial RF excitation, a 180° RF pulse is applied midway between excitation and TE. This inverts the spin phases and effectively rephases them, producing a measurable echo at TE (Figure 2.7). The spin echo concept was later extended in diffusion imaging with the Pulsed-Gradient Spin Echo (PGSE) sequence by Stejskal and Tanner (1965) (see Figure 2.9 and Section 2.2.1 for more details).

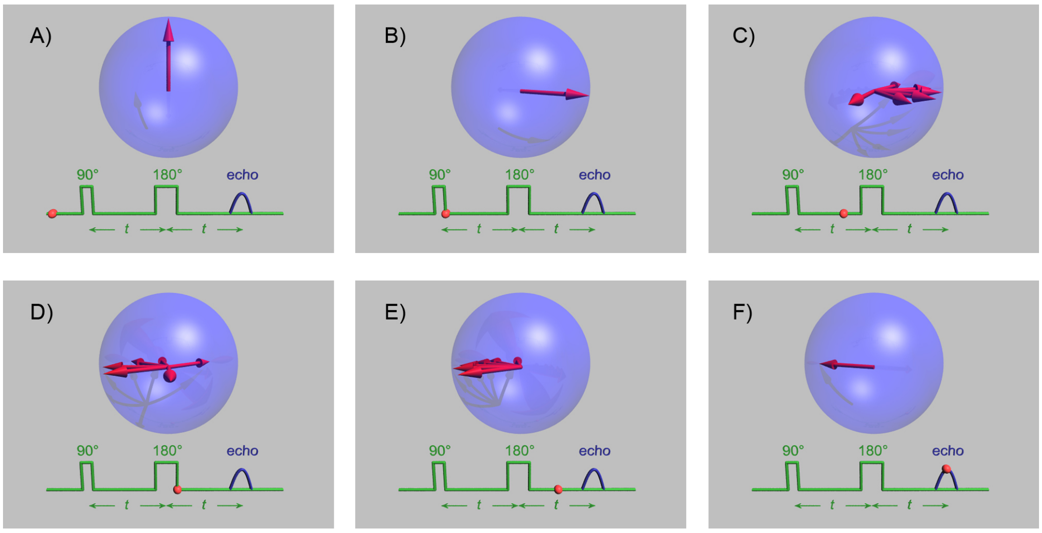

Figure 2.7: Spin echo sequence and spin rephasing. Initially (A-B), spins are tipped into the transverse plane and gradually dephase due to magnetic field inhomogeneities (C). After a 180° refocusing pulse (D), the phases invert, and the spins rephase (E), generating an echo at time TE (F), which restores coherence and recovers the signal. Image by Gavin W Morley, from Wikimedia Commons (`https://commons.wikimedia.org/wiki/File:SpinEcho_GWM_stills.jpg`), licensed under CC BY-SA 3.0.

Finally, to reconstruct the final image, three types of gradients are typically employed: the slice-selection gradient, which allows the excitation of a specific tissue slice; the frequency-encoding (readout) gradient, which maps position along one axis into distinct frequencies; and the phase-encoding gradient, which assigns positional information along the orthogonal axis by introducing controlled phase shifts. During acquisition, data are collected in Fourier space, or k-space, where one axis corresponds to frequency encoding and the other to phase encoding. Each point in k-space does not represent a single spatial location, but rather encodes spatial frequency information about the entire object. A two-dimensional inverse Fourier transform reconstructs each slice, and stacking multiple slices provides a three-dimensional (3D) representation of the brain (Mansfield, 1977).

2.2.1 Diffusion-weighted magnetic resonance imaging

Diffusion-weighted Magnetic Resonance Imaging (dMRI) is a specialized MRI technique sensitive to the microscopic random motion of water molecules in biological tissues (Basser et al., 1994b; Le Bihan et al., 1986). This motion, known as *diffusion*, is strongly influenced by the microstructural environment, including cell membranes, myelin, and extracellular space, as shown in Figure 2.8. As a result, dMRI provides indirect information about tissue organization that cannot be obtained from conventional T_1- or T_2-weighted images (Jones, 2010b).

In a free, unrestricted medium, molecular diffusion is *isotropic*, meaning that water molecules move with equal probability in all directions. The displacement of molecules follows a Gaussian distribution, and the mean squared displacement $\langle r^2 \rangle$ is proportional to the diffusion coefficient D:

$$\langle r^2 \rangle = 2Dt \quad (\text{in 1D})\,, \quad \langle r^2 \rangle = 6Dt \quad (\text{in 3D})\,. \tag{2.4}$$

In biological tissues, however, diffusion is hindered or restricted by microstructural barriers (Figure 2.8). This leads to *anisotropy*, where diffusion is easier along some directions than others (Basser et al., 1994a; Bihan et al., 1993). Specifically, in CSF, water diffuses almost freely and appears isotropic. Instead, GM, diffusion is moderately hindered, and in WM, axonal membranes and myelin sheaths constrain water displacement, making diffusion strongly anisotropic (i.e., restricted). This property underlies the sensitivity of dMRI to the architecture of brain tissues.

Diffusion weighting was introduced through the *Pulsed-Gradient Spin Echo (PGSE) sequence* (Stejskal and Tanner, 1965), illustreted in Figure 2.9. Two equal and opposite gradient pulses are applied around a spin-echo refocusing pulse. Spins that remain stationary are fully rephased, while those that diffuse accumulate phase shifts that cannot be completely refocused, leading to signal attenuation. This attenuation follows the Stejskal–Tanner equation:

$$S = S_0 e^{-bD}, \tag{2.5}$$

where S_0 is the signal without diffusion weighting, D is the diffusion coefficient, and b is the diffusion weighting factor. The b-value depends on the gradient

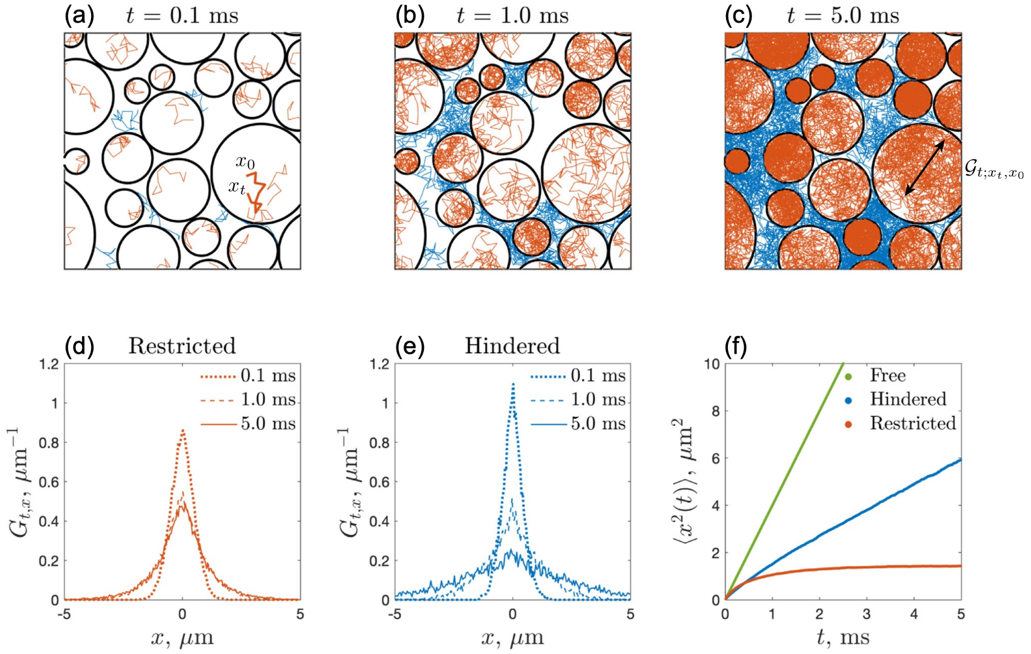

Figure 2.8: (a–c) Schematic illustration of water diffusion in different microstructural environments. Inside cells, diffusion is restricted by the cell membrane, whereas in the extracellular space, it is hindered by surrounding barriers and other cellular components. (d–e) Plots of the probability distribution ($G_{t,x}$) of molecular displacements along one direction (x) in the two environments. At short diffusion times (t), they are approximately Gaussian, but at longer times, restricted diffusion becomes non-Gaussian and stabilizes, reflecting the finite geometry of the compartment. (f) The mean squared displacement $\langle r^2 \rangle$ increases linearly with time for free diffusion (green), more slowly for hindered diffusion (blue), and reaches a plateau at long t for restricted diffusion (orange), as molecules encounter barriers that limit displacement. From (Novikov et al., 2025).

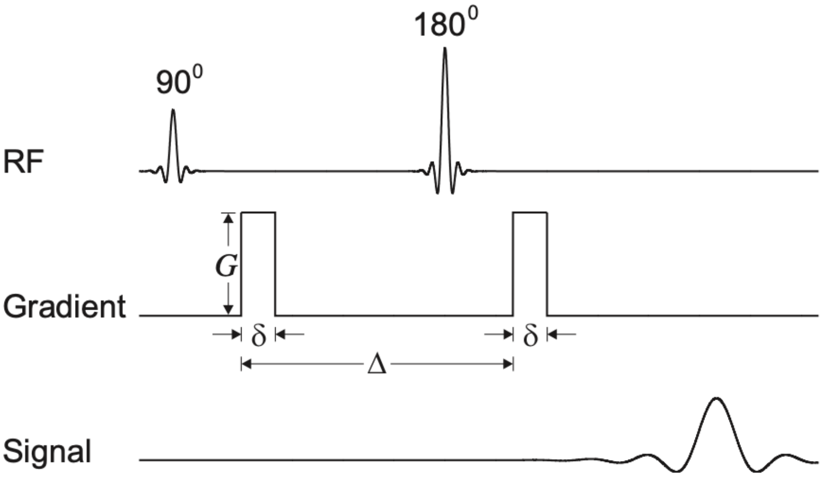

Figure 2.9: Pulsed-Gradient Spin Echo (PGSE) sequence. Two gradient pulses are applied around a spin-echo, causing signal attenuation for diffusing spins while stationary spins are fully rephased. The timing of the pulses (Δ and δ) controls sensitivity to water motion, enabling diffusion-weighted imaging. From (Basser and Özarslan, 2009).

strength (G), duration (δ), and separation (Δ):

$$b = \gamma^2 G^2 \delta^2 (\Delta - \delta/3). \tag{2.6}$$

The *b-value* plays a critical role in determining diffusion contrast. At low b-values, the signal resembles conventional T_2-weighted images. As shown in Figure 2.10, increasing the b-value enhances sensitivity to water motion: tissues with restricted diffusion remain bright (relatively hyperintense), while regions with free diffusion attenuate more rapidly. However, at the same time, higher b-values reduce the Signal-to-Noise Ratio (SNR) (Grebenkov, 2007). For this reason, diffusion MRI studies typically acquire data at multiple b-values and along multiple gradient directions. The diffusion-sensitizing gradient defines the direction along which the diffusion is encoded, enabling the characterization of tissue anisotropy. This property is especially prominent in WM, where diffusion is less hindered along the axonal direction than perpendicular to it. The effects of diffusion anisotropy can be seen in Figure 2.10. For example, the Corpus Callosum region exhibits marked signal attenuation when the diffusion gradient is applied along the left-right direction. This occurs because the axonal fibers within this tract are predominantly oriented in the same direction, connecting the two cerebral hemispheres. Moreover, since the diffusion coefficient measured by dMRI is not that of free water, Apparent Diffusion Coefficient (ADC) maps can be computed from such data, providing voxel-wise quantitative measures of diffusivity.

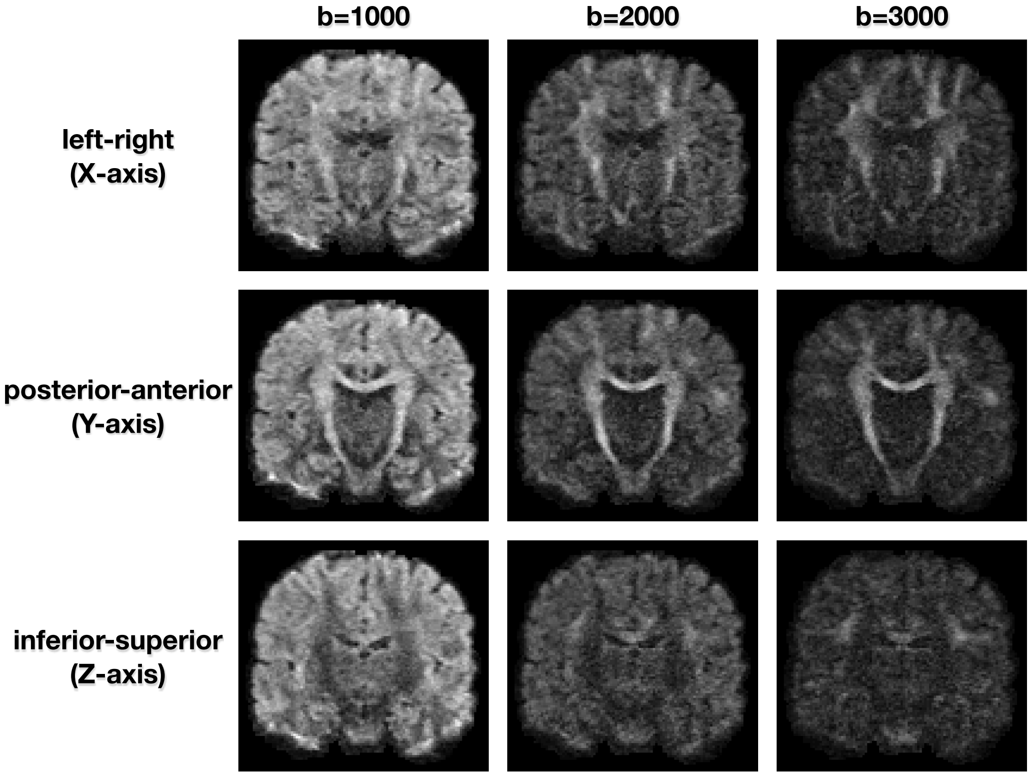

Figure 2.10: Example of diffusion-weighted MRI of the human brain (coronal slice). Increasing the diffusion weighting (b-values = 1000, 2000, and 3000 s/mm^2) accentuates differences in water mobility, while different structures can be appreciated by measuring the diffusion in different directions. Data from subject ID 103818 of the Human Connectome Project test-retest dataset (Van Essen et al., 2013a).

In summary, dMRI complements conventional MRI by examining the physical hindrance of water motion rather than relaxation properties. This unique sensitivity has made dMRI indispensable in both clinical practice — for example, in the early detection of ischemic stroke and tumor characterization — and research, where it provides insights into neurodevelopment, plasticity, and connectivity (Fan, 2021).

2.3 Using dMRI to study brain connectivity

2.3.1 From diffusion signal to local models

While the diffusion-weighted signal encodes information about water mobility (Section 2.2.1), the link between the measured signal and the underlying tissue microstructure is not direct. Each voxel in a diffusion-weighted image contains contributions from millions of water molecules moving within a complex ensemble of intra- and extracellular compartments. Therefore, models are needed to interpret signal attenuation in terms of physical tissue properties (Basser et al., 1994b; Novikov et al., 2019).

In general, the *q-space* is a 3D space where the position of each diffusion value is defined by the vector $\mathbf{q}$:

$$\mathbf{q} = \gamma\delta\mathbf{G}/2\pi\,, \tag{2.7}$$

which has a direction defined by the gradient vector $\mathbf{G}$ (Callaghan, 1996; Hagmann, 2005). Consequently, for a fixed diffusion time $t = \Delta - \delta/3$, it is related to the b-value by $b \sim \mathbf{q}^2$. Then, the observed dMRI signal attenuation $E(\mathbf{q})$ measured in the position $\mathbf{q}$ can be expressed as:

$$E(\mathbf{q}) = S(\mathbf{q})/S_0\,, \tag{2.8}$$

where S_0 is the baseline signal measured without diffusion weighting, i.e., $b = 0$. This quantity is indirectly related to the ensemble average propagator $P(\mathbf{r})$, which represents the probability that a water molecule is displaced by $\mathbf{r}$ during the diffusion time t. This propagator is also called diffusion Probability Density Function (dPDF), and the signal attenuation can be expressed as its Fourier transform:

$$E(\mathbf{q}) = \int_{\mathbb{R}^3} P(\mathbf{r})\, e^{-2\pi i \mathbf{q}^T \mathbf{r}}\, d\mathbf{r}\,. \tag{2.9}$$

This relation assumes that the diffusion gradient is infinitely short (i.e., Dirac pulse) and the full q-space is sampled (Callaghan et al., 1988). In practice, neither condition can be met: diffusion gradients have finite duration and strength, only a limited number of directions and b-values can be acquired, and SNR constraints prevent dense sampling of q-space (Basser et al., 1994b; Mori and Tournier, 2014). As a consequence, it is not possible to reconstruct the true ensemble average propagator directly, and simplified models of diffusion are employed to interpret the signal.

2.3.1.1 Diffusion tensor imaging

Under the assumption of Gaussian diffusion, water motion can be characterized by a single scalar parameter known as the ADC, which quantifies the average diffusivity of water molecules in all directions (Le Bihan et al., 1986; Le Bihan, 1991). While this model provides valuable information about the overall ability of water to move, particularly useful for detecting pathological changes such as ischemic stroke, it cannot capture directional dependence in tissues where diffusion is anisotropic, such as the WM. To overcome this limitation, the scalar diffusion coefficient can be generalized to a second-order symmetric tensor that accounts for the anisotropy of molecular motion within each voxel. This formulation establishes the basis of *Diffusion Tensor Imaging (DTI)*, introduced by Basser and colleagues in the mid-1990s (Basser et al., 1994b; Pierpaoli et al., 1996), which remains one of the most widely used dMRI models thanks to its simplicity, interpretability, and compatibility with clinical acquisition protocols.

DTI models diffusion in biological tissues as a positive-definite 3×3 matrix, the *diffusion tensor* $\mathbf{D}$:

$$\mathbf{D} = \begin{bmatrix} D_{xx} & D_{xy} & D_{xz} \\ D_{yx} & D_{yy} & D_{yz} \\ D_{zx} & D_{zy} & D_{zz} \end{bmatrix}, \tag{2.10}$$

which, due to its symmetry ($D_{ij} = D_{ji}$), is fully described by six independent components corresponding to the covariance of molecular displacements. In the corresponding q-space, the diffusion-weighted signal attenuation takes the form:

$$E(\mathbf{q}) = e^{(-\mathbf{q}^T \mathbf{D} \mathbf{q})} \,, \tag{2.11}$$

showing that it depends on the orientation of the applied gradient $\mathbf{q}$ relative to the principal diffusion directions within the voxel (Basser et al., 1994b; Jones, 2010b; Novikov et al., 2019).

In practical dMRI acquisitions, diffusion weighting is achieved using a set of gradient directions $\mathbf{G}_i$ and corresponding b-values. The measured signal along each direction i can be expressed through the Stejskal–Tanner formulation:

$$S_i = S_0 \, \exp\left(-b \, \mathbf{G}_i^T \mathbf{D} \mathbf{G}_i\right) , \tag{2.12}$$

where S_0 is the non-diffusion-weighted signal, and b reflects the strength and timing of the diffusion gradients. To estimate the six components of $\mathbf{D}$, at least six non-collinear diffusion-weighted measurements are needed, in addition to a non-diffusion-weighted ($b = 0 \ s/mm^2$) reference image. In practice, many more measurements are typically acquired to improve robustness and reduce noise sensitivity (Giannelli et al., 2010).

As illustrated in Figure 2.11, once estimated, the diffusion tensor can be diagonalized to obtain its three eigenvalues λ_1, λ_2, and λ_3, and the corresponding eigenvectors ν_1, ν_2, and ν_3, which represent the principal directions and magnitudes of diffusion along the three orthogonal axes. This decomposition provides an intuitive geometric interpretation of diffusion as an ellipsoid, whose shape and orientation reflect the degree and directionality of molecular motion (Figure 2.11). These quantities enable the derivation of scalar indices summarizing key aspects of tissue microstructure, as shown in Figure 2.12 (Basser and Pierpaoli, 1996; Pierpaoli et al., 1996).

The Mean Diffusivity (MD), defined as the average of the eigenvalues,

$$\mathrm{MD} = \frac{\lambda_1 + \lambda_2 + \lambda_3}{3} \,, \tag{2.13}$$

reflects the overall magnitude of water diffusion within the voxel. The Axial Diffusivity (AD), AD $= \lambda_1$, characterizes diffusion along the principal axis

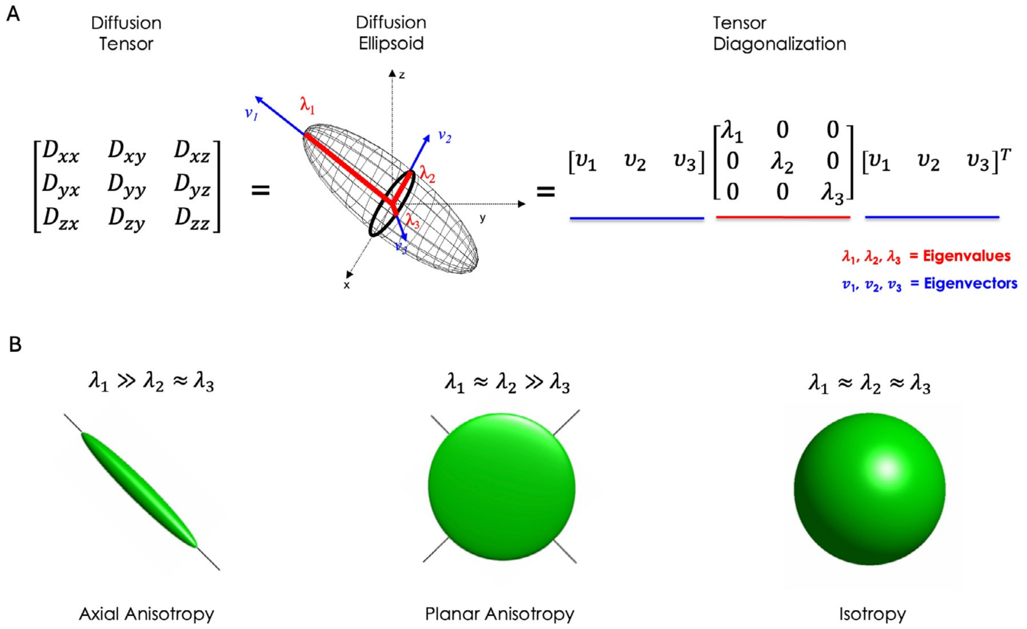

Figure 2.11: Diffusion tensor representations. (A) The diffusion tensor can be expressed as a 3×3 symmetric matrix or visualized as a diffusion ellipsoid, whose principal axes correspond to the eigenvectors ν_1, ν_2, and ν_3, and whose lengths reflect the eigenvalues λ_1, λ_2, and λ_3. (B) Examples of tensor shapes with the corresponding comparison between the three eigenvalues: elongated ellipsoids indicate axial anisotropy with predominant diffusion along one direction, flattened ellipsoids indicate planar anisotropy, and spherical tensors correspond to isotropic diffusion. From (Dell'Acqua et al., 2025).

and is often associated with axonal integrity, whereas the Radial Diffusivity (RD),

$$\mathrm{RD} = \frac{\lambda_2 + \lambda_3}{2}\,, \tag{2.14}$$

describes diffusion perpendicular to the main fiber axis and has been linked to myelin microstructure. Finally, the Fractional Anisotropy (FA) quantifies the degree of diffusion anisotropy and is defined as:

$$\mathrm{FA} = \sqrt{\frac{3}{2}}\,\frac{\sqrt{(\lambda_1 - \mathrm{MD})^2 + (\lambda_2 - \mathrm{MD})^2 + (\lambda_3 - \mathrm{MD})^2}}{\sqrt{\lambda_1^2 + \lambda_2^2 + \lambda_3^2}}\,. \tag{2.15}$$

FA values close to 1 indicate highly directional diffusion, as found in coherent

WM fiber bundles, whereas values near 0 correspond to isotropic diffusion, typical of GM or CSF.

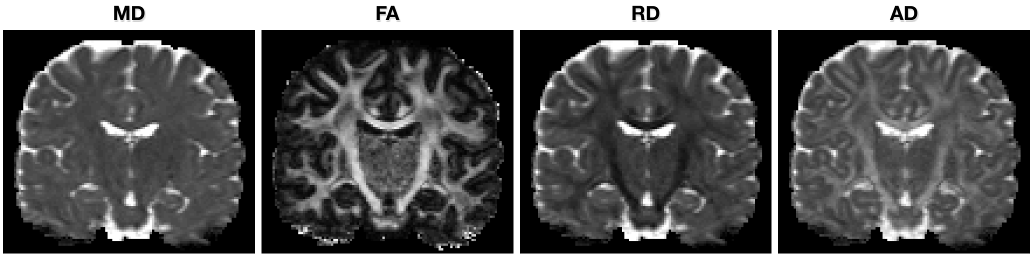

Figure 2.12: Coronal slices illustrating standard scalar metrics derived from diffusion tensor imaging: Mean Diffusivity (MD), Fractional Anisotropy (FA), Radial Diffusivity (RD), and Axial Diffusivity (AD). Data from subject ID 103818 of the Human Connectome Project test-retest dataset (Van Essen et al., 2013a).

Maps of FA, MD, AD, and RD have become standard tools for characterizing tissue microstructure and WM integrity in both clinical and research contexts. Variations in these parameters have been associated with developmental processes, aging, and a wide range of neurological and psychiatric disorders (Alexander et al., 2007; Jones et al., 2013). The principal eigenvector $\mathbf{e}_1$ is commonly interpreted as the predominant fiber orientation within the voxel and serves as the basis for tractography algorithms aimed at reconstructing WM pathways (see Section 2.3.2 for more details) (Basser et al., 2000; Mori et al., 1999).

Despite its widespread use, the single-tensor representation in DTI provides only a simplified view of the underlying microstructure. It inherently assumes Gaussian diffusion and a single dominant orientation per voxel, which limits its ability to represent the complex organization of WM, as illustrated in Figure 2.13. In many brain regions, diffusion arises from multiple fiber populations exhibiting crossings, branchings, or fanning patterns — configurations that cannot be resolved by the DTI model (Jeurissen et al., 2013; Jones, 2010b). These shortcomings have motivated the development of more advanced frameworks capable of capturing non-Gaussian diffusion and resolving multiple orientations within a voxel, such as High-Angular-Resolution Diffusion Imaging (HARDI) and multi-compartment modeling approaches (Jelescu et al., 2016; Tournier et al., 2011; Tuch, 2004).

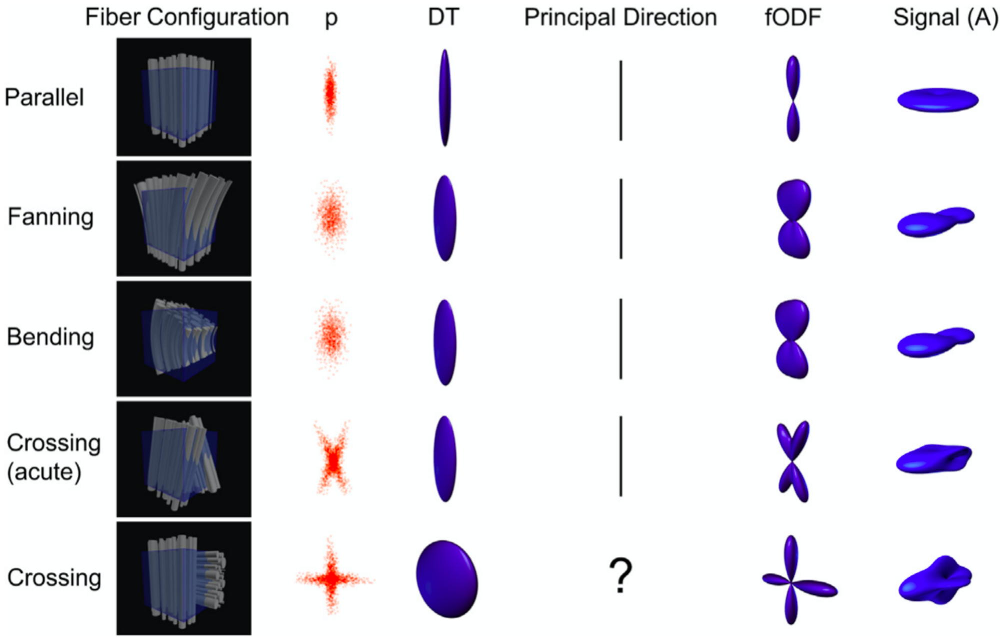

Figure 2.13: Simple configurations of axon fibers and corresponding diffusion representations. The first column depicts typical fiber geometries encountered in brain voxels; subsequent columns illustrate (from left to right) the expected diffusion scatter pattern (probability distribution on the water displacement), the best-fit diffusion tensor, its principal direction, the fiber orientation distribution function, and the directional variation of the diffusion-weighted signal. In regions with crossing or planar fiber configurations, the single-tensor model cannot accurately represent the underlying diffusion process, leading to ambiguous or undefined principal orientations. From (Seunarine and Alexander, 2014).

2.3.1.2 High Angular Resolution Diffusion Imaging

High-Angular-Resolution Diffusion Imaging (HARDI) extends dMRI beyond the tensor model by increasing the angular sampling of diffusion-encoding directions to better characterize the underlying directional structure of water diffusion (Hagmann, 2005; Tuch et al., 2002). Rather than assuming Gaussian diffusion, HARDI enables the representation of more complex, non-Gaussian displacement profiles, allowing the detection of multiple fiber orientations within a single voxel (Tournier et al., 2011; Tuch, 2004). By acquiring data along tens to hundreds of uniformly distributed gradient directions, HARDI provides sufficient angular resolution to reconstruct the angular dependence of the diffusion signal and infer more accurately the underlying fiber architecture (Descoteaux, 2008; Jones, 2010b).

In this framework, diffusion information is sampled over a dense set of gradient directions (typically more than 60) distributed across a single or multiple spherical shells in q-space, allowing for a detailed characterization of the diffusion signal as a function of orientation. HARDI techniques aim to reconstruct the *Orientation Distribution Function (ODF)*, which describes the probability of water diffusion along each spatial direction (Hagmann, 2005; Tuch et al., 2002). The ODF is closely related to the diffusion propagator but integrates out its radial component, focusing solely on directional information (Tuch, 2004). This formulation enables the visualization of multiple dominant diffusion directions within a voxel, revealing complex fiber configurations, such as crossings or branchings, that cannot be represented by the DTI model, which is limited to ellipsoidal shapes.

Several approaches have been proposed to estimate the ODF from HARDI data. Among the earliest and most influential is *Q-ball Imaging (QBI)*, introduced by Tuch (2004). It reconstructs the ODF by performing a spherical inversion of the diffusion signal based on the Funk–Radon transform, which links measurements on q-space sphere to the underlying diffusion orientation distribution (Figure 2.14). This non-parametric method allows the estimation of the angular structure of diffusion without assuming any specific microstructural model or compartment configuration. While QBI represented a major step forward in visualizing complex WM architectures, it provides only a qualitative ODF and remains sensitive to noise and limited angular sampling.

To improve robustness and interpretability, later approaches employed a mathematical framework based on *Spherical Harmonics (SH)*, which repre-

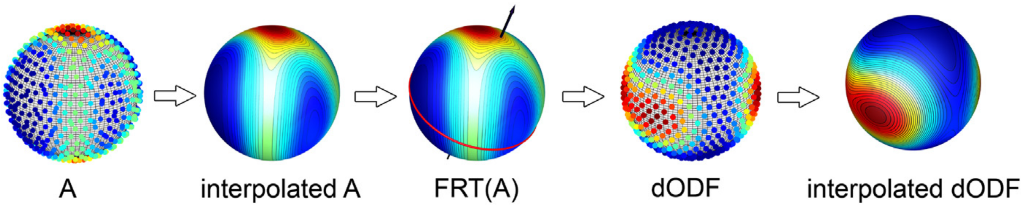

Figure 2.14: Main steps of the Q-ball Imaging algorithm. Diffusion-weighted signal (A) is sampled on a spherical shell in q-space and interpolated. Then, the orientation distribution function (dODF) is estimated using the Funk-Radon transform (FRT). Repeating this process across orientations yields a full set of ODF samples, which can then be interpolated to reconstruct the continuous diffusion ODF. From (Dell'Acqua et al., 2025).

sent functions defined on the sphere as weighted sums of orthogonal basis functions (Descoteaux, 2008; Tournier et al., 2007). SH are characterized by two parameters: the *degree* l, corresponding to the spatial frequency of the function over the sphere, and the *order* m, defining its phase component. Higher harmonic degrees capture finer angular details of the diffusion signal, while lower degrees describe its coarse features. This frequency-based representation enables efficient modeling and smoothing of the diffusion signal across orientations, thereby reducing sensitivity to noise and facilitating analytical operations such as angular differentiation and deconvolution. Each voxel's diffusion profile can thus be compactly represented by a vector of SH coefficients, whose number depends on the chosen maximum harmonic order $l_{\max}$ and the angular resolution of the acquisition. Figure 2.15 illustrates examples of real SH basis functions, showing their increasing angular complexity with higher harmonic degrees.

Building upon this representation, *Spherical Deconvolution (SD)* methods were introduced to estimate the Fiber Orientation Distribution (FOD), or fiber Orientation Distribution Function (fODF), which quantifies the relative contribution of different fiber populations within a voxel (Tournier et al., 2004). The central assumption is that the measured diffusion signal S can be modeled as the spherical convolution of a single-fiber response function

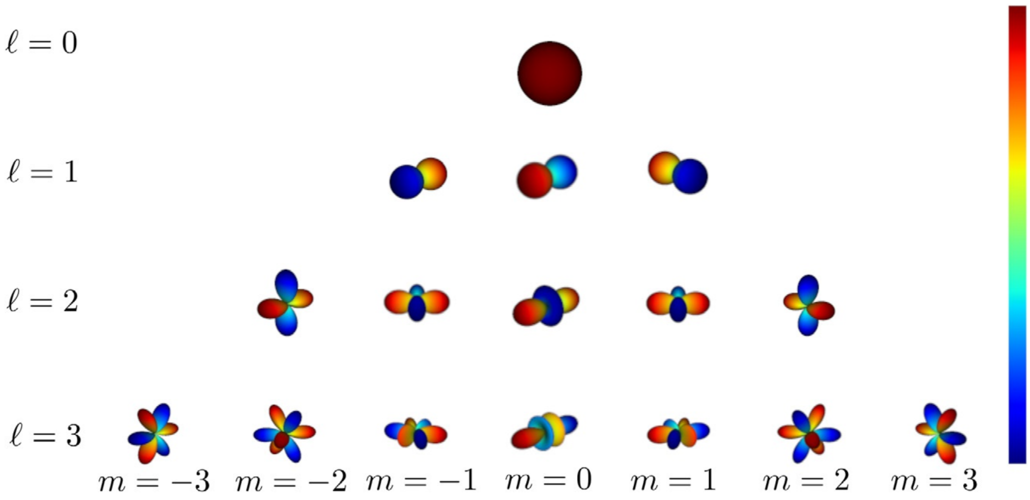

Figure 2.15: Examples of real Spherical Harmonics (SH) basis functions on the unit sphere for increasing harmonic degree l. Lower orders represent slowly varying components of the diffusion signal, while higher orders capture fine angular detail. The combination of these basis functions allows efficient reconstruction of complex diffusion profiles on the sphere. From (Grenier et al., 2025).

with the unknown FOD (Figure 2.16). Expressed in the spherical harmonic domain, the convolution simplifies to a multiplication: $S = R\,F$, where R are the SH coefficients of the response function, and F are those of the FOD. The FOD can then be recovered by solving an inverse problem, i.e., by dividing the observed coefficients by R, providing an analytical solution. This approach effectively separates multiple fiber orientations and reveals crossing or fanning patterns within voxels that appear homogeneous in DTI.

Although standard SD can resolve multiple orientations, it is sensitive to noise, and the ill-posed nature of the deconvolution may lead to oscillations or spurious peaks in the estimated FOD. To overcome these limitations, *Constrained Spherical Deconvolution (CSD)* introduces additional regularization by enforcing non-negativity on the FOD, ensuring that the estimated fiber orientations correspond to physically plausible diffusion directions and reducing artifacts in regions of low anisotropy (Tournier et al., 2007). The introduction

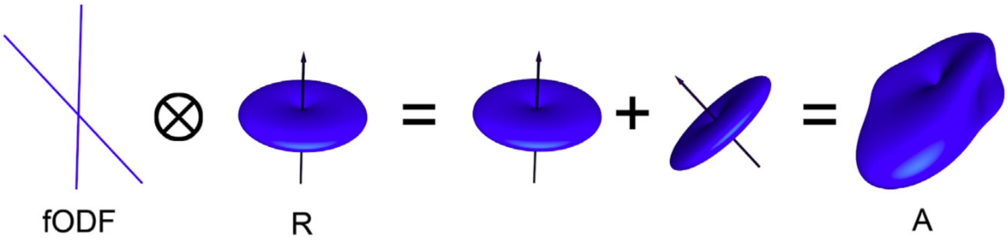

Figure 2.16: Schematic illustration of Spherical Deconvolution. The measured diffusion signal (left) is modeled as the convolution of a single-fiber response function (center) with the underlying fiber orientation distribution (FOD, right). Deconvolution in the spherical harmonic domain enables the estimation of distinct fiber orientations within a voxel. From (Seunarine and Alexander, 2014).

of sparsity priors further suppresses noise-related fluctuations and improves the discrimination of closely oriented fiber populations (Tournier et al., 2007). As illustrated in Figure 2.17, the basic form of SD is highly sensitive to noise, often producing spurious peaks in the estimated FOD. Regularized implementations, such as those proposed by Tournier et al. (2007, 2004), mitigate this issue by suppressing high-frequency components or imposing non-negativity and smoothness constraints, thereby improving the stability and interpretability of the results.

The angular resolution achievable with HARDI methods also strongly depends on the diffusion weighting, expressed by the b-value. While $b \approx 1000\ s/mm^2$ has become a standard choice for DTI acquisitions in human studies, such moderate diffusion weighting limits sensitivity to multiple fiber orientations. Higher b-values increase the angular contrast of the diffusion signal, improving the ability to distinguish fiber populations separated by small crossing angles (Tournier et al., 2013). As illustrated in Figure 2.18, higher b-values yield sharper and more distinct peaks in the estimated FODs, enhancing the discrimination of complex fiber configurations. However, increasing b-values also reduces the SNR, necessitating a balance between angular resolution, spatial resolution, and overall image quality. For typical in vivo

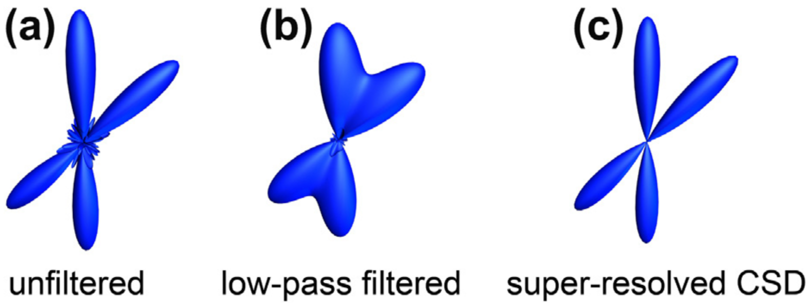

Figure 2.17: Example of fiber orientation distributions (FODs) estimated with standard spherical deconvolution (a) from noisy data, containing multiple spurious peaks. Low-pass filtering reduces noise sensitivity but at the cost of angular resolution (b). Constrained Spherical Deconvolution (CSD) using regularization removes negative lobes and spurious peaks while preserving fine angular detail (c). From (Seunarine and Alexander, 2014).

human acquisitions, b-values in the range of 2000–3000 s/mm^2 combined with 60–90 uniformly distributed gradient directions have been shown to provide an effective compromise between angular precision and SNR (Jones, 2010b; Tournier et al., 2013).

The development of HARDI and its SH- and deconvolution-based implementations has profoundly influenced modern dMRI, bridging the gap between simple Gaussian tensor models and more detailed multi-compartment frameworks. By providing richer angular information, HARDI-based methods more accurately capture the complex organization of WM, improving both tractography and microstructural analyses (Jones, 2010b; Tournier et al., 2011). As shown in Figure 2.19, compared to the single-orientation representation of DTI, CSD resolves multiple distinct fiber populations within a voxel.Although these methods require higher angular sampling, longer acquisition times, and greater computational effort than DTI, they yield a richer and more realistic characterization of WM architecture. Consequently, HARDI has become a cornerstone of advanced dMRI, enabling detailed exploration of brain structure and its alterations across development, aging, and disease.

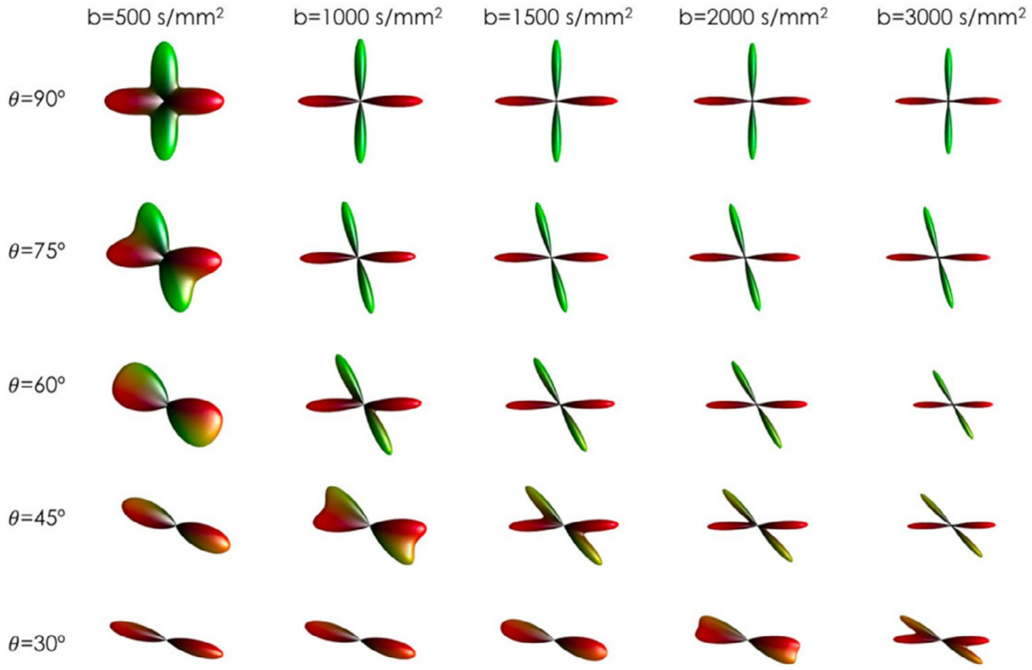

Figure 2.18: Effect of different b-values on the angular resolution of the Fiber Orientation Distribution (FOD). From left to right, increasing the b-value enhances the ability to resolve smaller angular separations between fiber populations, producing sharper and more distinct FOD peaks. From (Dell'Acqua and Tournier, 2019).

2.3.1.3 Microstructure models

Although techniques such as DTI and CSD provide essential information to estimate the fibers' direction, they do not explicitly account for the underlying microstructural properties of the tissue. To achieve a more biologically meaningful characterization of WM, a range of *multi-compartment models* has been developed to describe the diffusion signal in terms of distinct micro-environmental contributions. These microstructure models aim to infer quantitative indices that reflect specific tissue features such as neurite density, orientation dispersion, and intra-/extra-axonal diffusivities (Alexander et al., 2019; Jelescu et al., 2016; Novikov et al., 2019; Panagiotaki et al., 2012).

As explained in Section 2.2.1, the dMRI signal measured in vivo arises

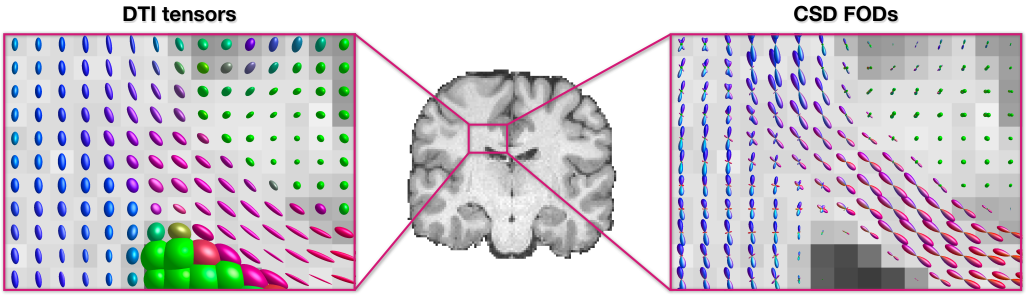

Figure 2.19: Comparison between Diffusion Tensor Imaging (DTI) and Constrained Spherical Deconvolution (CSD). Looking at the corona radiata region (from a coronal section, middle), DTI evidently represents diffusion as a single ellipsoid per voxel (left), whereas CSD reveals multiple distinct fiber orientations (right), providing a more accurate description of complex crossing and fanning configurations of white matter. Data from subject ID 103818 of the Human Connectome Project test-retest dataset (Van Essen et al., 2013a).

from water molecules moving within different tissue compartments: inside and outside axons, within soma, dendrites, and glial cells. Because these environments impose distinct degrees of hindrance or restriction to diffusion, the observed signal can be modeled as the weighted sum of multiple compartmental contributions, each describing a specific diffusion regime (Assaf and Basser, 2005; Jelescu et al., 2016).

Early microstructural approaches extended the diffusion tensor framework to represent multiple fiber populations within a voxel by combining several Gaussian compartments, leading to the so-called *multi-Gaussian models* (Parker and Alexander, 2003; Tuch et al., 2002). Similarly, the *ball-and-stick* model (Behrens et al., 2007, 2003) represents isotropic and anisotropic diffusion components, assuming independent compartments for free water and fibers with coherent orientation. Later developments, such as the *Composite Hindered and Restricted Model of Diffusion (CHARMED)* (Assaf and Basser, 2005) and *AxCaliber* (Assaf et al., 2008), generalized this framework by explicitly modeling axons as impermeable cylinders, enabling the estimation of axonal diameter distributions. These formulations paved the way for more biologically grounded models applicable to clinical acquisitions, including

NODDI and SMT.

The *Neurite Orientation Dispersion and Density Imaging (NODDI)* model (Zhang et al., 2012) provides a simplified yet biophysically interpretable representation of the microstructural complexity of neurites (dendrites and axons). It describes the diffusion signal as the mixture of three compartments: intracellular, extracellular, and isotropic (CSF), according to:

$$A = (1 - \nu_{iso})(\nu_{ic} A_{ic} + (1 - \nu_{ic}) A_{ec}) + \nu_{iso} A_{iso}. \tag{2.16}$$

Here, ν_{ic} and A_{ic} denote the intracellular volume fraction (ICVF) and normalized signal; A_{ec} and A_{iso} correspond to the extracellular and isotropic signal components, respectively. The intracellular space represents diffusion within dendrites and axons, characterized by strong restriction perpendicular to their orientation, whereas the extracellular compartment models hindered diffusion in the surrounding medium (Zhang et al., 2012). From this model, quantitative indices such as the ICVF (ν_{ic}), the orientation dispersion index (OD), and the isotropic volume fraction (ν_{iso}) can be derived, providing biologically interpretable measures of neurite density, angular dispersion, and extracellular free-water content.

The *Spherical Mean Technique (SMT)* (Kaden et al., 2016) represents another major advancement in microstructural modeling. It aims to estimate tissue-specific microscopic parameters independently of fiber orientation by exploiting the spherical mean of the diffusion signal. For a given diffusion weighting b, the mean signal can be expressed as:

$$\bar{e}_b = \nu_{int} \, \bar{e}_b^{\,int} + (1 - \nu_{int}) \, \bar{e}_b^{\,ext}, \tag{2.17}$$

where ν_{int} is the intra-neurite volume fraction, and $\bar{e}_b^{\,int}$ and $\bar{e}_b^{\,ext}$ are the spherical means of the intra- and extra-neurite compartments, respectively. By averaging the diffusion signal over all gradient directions, SMT effectively removes the confounding effects of fiber crossings and orientation dispersion, isolating intrinsic diffusivities that characterize the microscopic environment (Kaden et al., 2016). The resulting maps — such as intra-neurite volume fraction, intrinsic diffusivity, and extra-neurite transverse diffusivity —

provide orientation-independent biomarkers of WM microstructure that can complement tractography analyses.

Together, models such as NODDI and SMT bridge the gap between macroscopic diffusion anisotropy and microscopic tissue composition. Their integration with tractography enables *microstructure informed* analyses (Section 2.4.1) that quantify not only the geometry of WM pathways but also their underlying biophysical properties, improving the interpretability and diagnostic value of dMRI.

2.3.2 From local fiber orientations to tractography

Tractography, or fiber tracking, refers to the group of techniques designed to infer the trajectories of neuronal fibers in the WM from dMRI data (Basser et al., 2000; Dell'Acqua et al., 2025; Mori et al., 1999). By modeling the directionality of water diffusion, tractography enables the *in vivo* reconstruction of the brain' WM architecture. Before the development of diffusion imaging, this task was only achievable through invasive or post-mortem tracing studies; tractography has therefore profoundly transformed neuroscience by providing non-invasive insights into both healthy and pathological brain connectivity (Catani, 2025).

As illustrated in Figure 2.20, the output of tractography is a *tractogram*, a collection of 3D trajectories known as *streamlines*. These polylines approximate the pathways of axonal populations by following the local diffusion orientations estimated in each voxel (Jeurissen et al., 2019). In its simplest implementation, each streamline is generated by integrating direction vectors derived from a diffusion model, starting from a predefined position in the data, known as a seed point, and propagating until a termination criterion is reached (Leemans et al., 2025). Each voxel in a dMRI acquisition typically contains thousands of axons with different orientations (Jeurissen et al., 2013), and the measured signal reflects their collective properties rather than any individual fiber, operating at the *mesoscopic* scale (Novikov et al., 2025). A streamline should therefore be interpreted not as a single axon, but as the estimated trajectory of a coherent fiber population. Despite this abstraction, tractography remains the only non-invasive method capable of mapping the geometry and connectivity of WM pathways throughout the entire human brain.

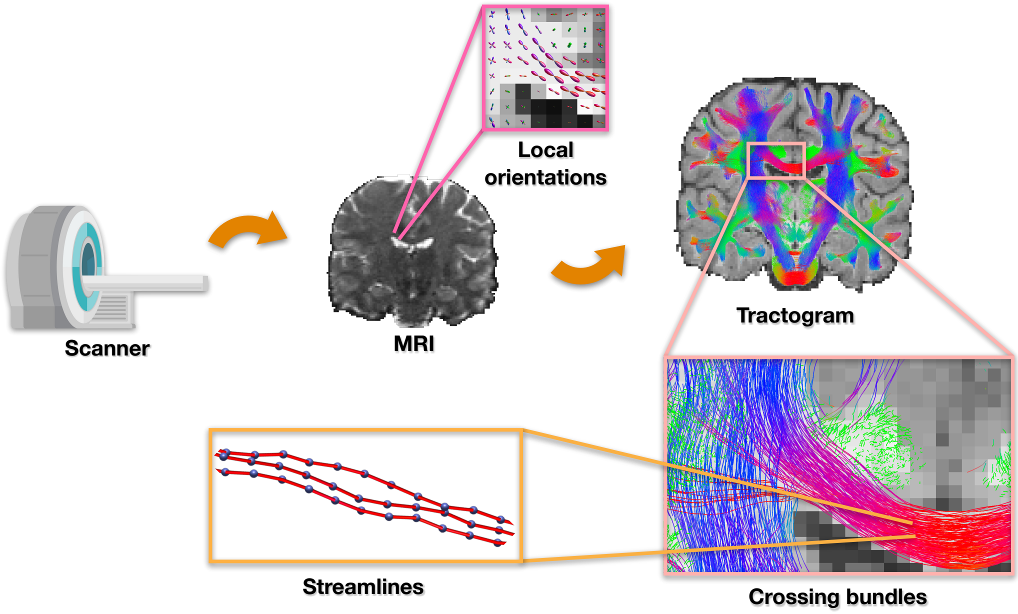

Figure 2.20: The tractography process starts from the acquired brain MRI, which captures the flow of water molecules within the tissues. Using the local orientations estimated in each voxel, it is possible to reconstruct a whole-brain tractogram characterizing the white matter architecture. It consists of a set of streamlines, where a streamline is a polyline in the 3D space representing the trajectory of a set of coherent fibers.

Tractography has become a fundamental tool in both research and clinical contexts. In neuroscience, it enables the mapping of structural connectivity and the reconstruction of large-scale networks, forming the basis for connectomic analyses (Hagmann et al., 2008; Sporns et al., 2005) (Section 2.3.3). Clinically, it plays a key role in the study of neurodevelopmental and neurodegenerative disorders and in pre-surgical planning, where it supports the identification and preservation of critical WM tracts during neurosurgical interventions (Rheault et al., 2025a).

2.3.2.1 Principles of tractography

Tractography exploits the directional information contained in dMRI data to infer the most probable trajectories of WM fibers. The fundamental assumption is that water diffusion within brain tissue is hindered by cellular structures such as axonal membranes and myelin sheaths (Section 2.2.1), resulting in anisotropic diffusion that is greatest along the predominant fiber orientation (Basser et al., 1994b; Jones, 2010b). By estimating this local diffusion direction in each voxel (Section 2.3.1) and linking them across neighboring voxels, tractography reconstructs continuous pathways that reflect the structural organization of WM (Basser et al., 2000; Mori et al., 1999; Poupon et al., 2000). Nowadays, many strategies exist to perform tractography (Jeurissen et al., 2019), but most pipelines can be conceptually divided into three main components: (*i*) the estimation of local diffusion orientations, (*ii*) the generation and propagation of trajectories, and (*iii*) the definition of stopping and acceptance criteria.

The first stage, local diffusion modeling, depends on the type of data acquired and the diffusion model adopted. Simple models such as DTI allow the estimation of a single dominant orientation per voxel, while more advanced models like CSD enable the reconstruction of multiple orientations, better capturing complex fiber configurations (Descoteaux, 2008; Tournier et al., 2004), as shown in Figure 2.21. The resulting orientation field provides the local directional information used during tracking.

Different approaches have been developed to generate trajectories, leading to various classification schemes. The most common distinction is between *local* or *line propagation* methods, which integrate orientation information step by step, and *global* techniques, which reconstruct entire pathways by optimizing a global cost function (Jeurissen et al., 2019). Local methods can be further subdivided into *deterministic* algorithms, which follow the main direction at each step, and *probabilistic* ones, which sample from an orientation distribution to account for uncertainty in local fiber estimates (Dell'Acqua et al., 2025; Jones, 2010b). Global, or energy-minimization, approaches instead aim to estimate the most plausible overall configuration of fibers in the

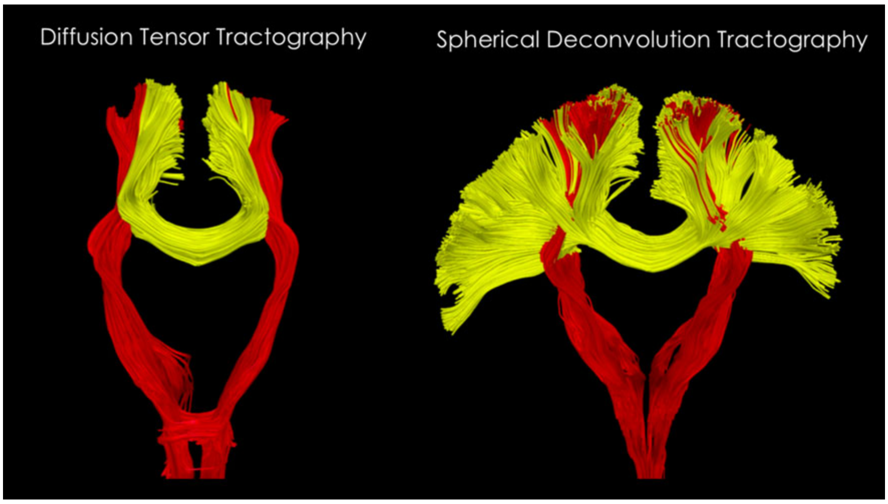

Figure 2.21: Tensor-based tractography (left) models a single dominant fibre orientation per voxel, so it fails to resolve crossing fibres, as shown for the lateral projections of the corpus callosum (yellow) that are interrupted by the denser corticospinal tract (red). Instead, multi-fibre spherical deconvolution (right) enables streamlines to traverse crossing regions, recovering a more complete representation of both pathways. From (Dell'Acqua and Tournier, 2019).

brain (Mangin et al., 2013). More recent developments also include tractography methods based on machine learning, graph theory, or explicit anatomical priors, further enhancing biological plausibility and reproducibility (Neher et al., 2025; Poulin et al., 2019).

Finally, tractography requires defining *stopping* and *acceptance* criteria, which determine whether a reconstructed streamline is considered valid. Stopping rules are typically based on physical or anatomical conditions such as low anisotropy, excessive curvature between successive steps, or entry into non-WM regions (Basser et al., 2000; Mori et al., 1999). Acceptance criteria, on the other hand, define when a streamline is retained as part of a tract of interest, often requiring that it connects specific regions or passes through target masks. These constraints are essential to ensure anatomical consistency and to reduce the inclusion of implausible trajectories, which is crucial for the interpretation of tractography results in both research and clinical applications.

2.3.2.2 Local tractography methods

Local tractography methods constitute the most widely adopted class of algorithms for reconstructing WM pathways from dMRI data. These techniques operate by incrementally propagating streamlines through the voxel-wise diffusion orientation field, integrating local directional information to reconstruct macroscopic fiber trajectories (Basser et al., 2000; Mori et al., 1999; Tournier et al., 2012). Due to their conceptual simplicity and computational efficiency, local approaches form the foundation of most tractography pipelines.

The techniques belonging to this class can be divided into deterministic and probabilistic; the distinction lies in how local fiber orientations are sampled during streamline propagation (Figure 2.22). In *deterministic* approaches, the streamline follows a single principal direction at each step, typically corresponding to the main eigenvector of the diffusion tensor or to the dominant peak of the FOD estimated by SD (Leemans et al., 2025). This strategy yields highly reproducible trajectories and sharp delineation of major bundles, and it is implemented in classical methods such as FACT (Mori et al., 1999) or the spherical deconvolution–based *SD_STREAM* (Tournier et al., 2012). However, deterministic tracking is inherently sensitive to noise and partial volume effects and often fails in regions with crossing, fanning, or kissing fibers.

Probabilistic methods, in contrast, explicitly model uncertainty in local fiber orientation by sampling directions from a probability distribution derived from the diffusion model (Girard et al., 2025). At each propagation step, a new orientation is randomly drawn from this distribution, typically weighted by the amplitude of the local FOD. If no orientation satisfies the angular or amplitude constraints (e.g., minimum FOD value, maximum curvature), propagation is stopped (Descoteaux et al., 2009; Tournier et al., 2012). Probabilistic algorithms enable exploration of multiple plausible trajectories and provide a richer representation of uncertainty in regions with complex microstructure, although they produce a broader, less specific set of stream-

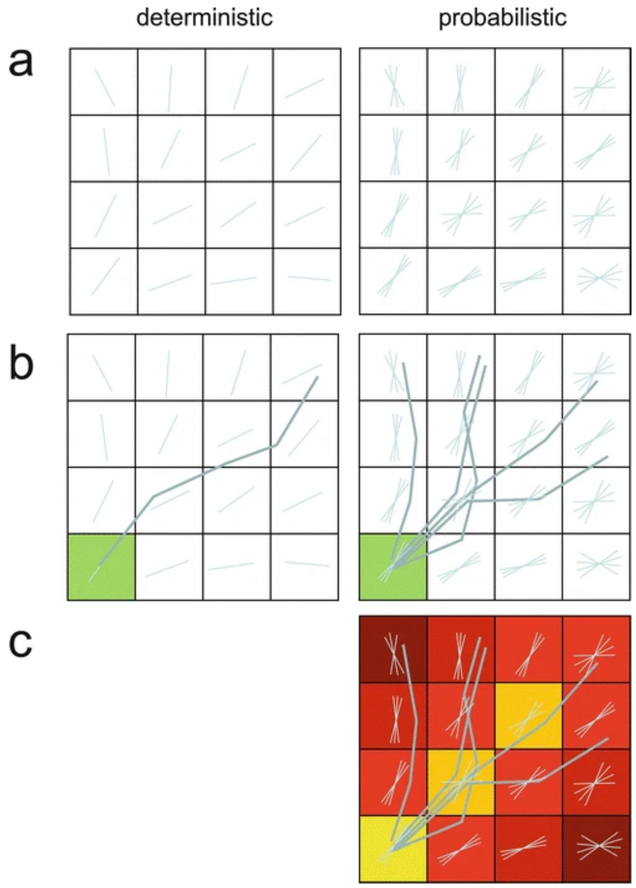

Figure 2.22: (a) Deterministic tracking follows the principal diffusion direction in each voxel, whereas probabilistic methods sample from a distribution of possible fibre orientations. (b) From a seed voxel (green), deterministic algorithms produce a single trajectory, while probabilistic ones generate multiple streamlines by sampling different orientations at each step. (c) A tract probability map is built by considering how many probabilistic streamlines pass through each voxel. From (Caan, 2016).

lines. Consequently, probabilistic tractograms are often dense; however, they can be refined or filtered using anatomical or quantitative criteria later. A widely used algorithm is the *second-order integration over FODs (iFOD2)* algorithm, which introduced a more sophisticated propagation model than the first implementations (Tournier et al., 2010). iFOD2 approach accounts for rapid angular variations, thereby improving the reconstruction of trajectories in regions of high curvature or fiber crossings, and yielding more stable and anatomically faithful results.

Building upon these principles, the *Parallel Transport Tractography (PTT)* algorithm (Aydogan and Shi, 2021), also known as *Trekker*, further refines the probabilistic framework by introducing a geometric formalism that ensures more coherent trajectories. As shown in Figure 2.23, PTT generalizes the iFOD2 concept by using probes, i.e., small cylindrical segments composed of multiple parallel lines, that sample FOD amplitudes along their extent. At each step, the most likely probe orientation is selected, and its reference frame is continuously updated along the trajectory using parallel transport. This allows the generation of geometrically smooth streamlines that better preserve the topographic organization of WM bundles and improve robustness in regions with high curvature or complex crossings.

Streamlines' generation also requires defining a seeding strategy and a set of tracking parameters that strongly influence the resulting tractogram. *Seeding* can be performed throughout the WM (whole-brain tractography), within specific regions of interest (ROI-based), or along surfaces such as the WM-GM interface, as illustrated in Figure 2.24. Dynamic seeding strategies adaptively distribute seeds to achieve uniform streamline density (Smith et al., 2015a). Key *tracking parameters* include the integration step size, curvature threshold, and minimum FOD amplitude required for propagation. Streamlines are typically terminated when these criteria are violated, when entering non-WM regions, or when reaching the user-defined maximum or minimum lengths. Together, these parameters control the anatomical coverage, density, and smoothness of the reconstructed pathways.

To enhance biological plausibility, anatomical priors are increasingly incorporated into local tractography frameworks. *Anatomically Constrained*

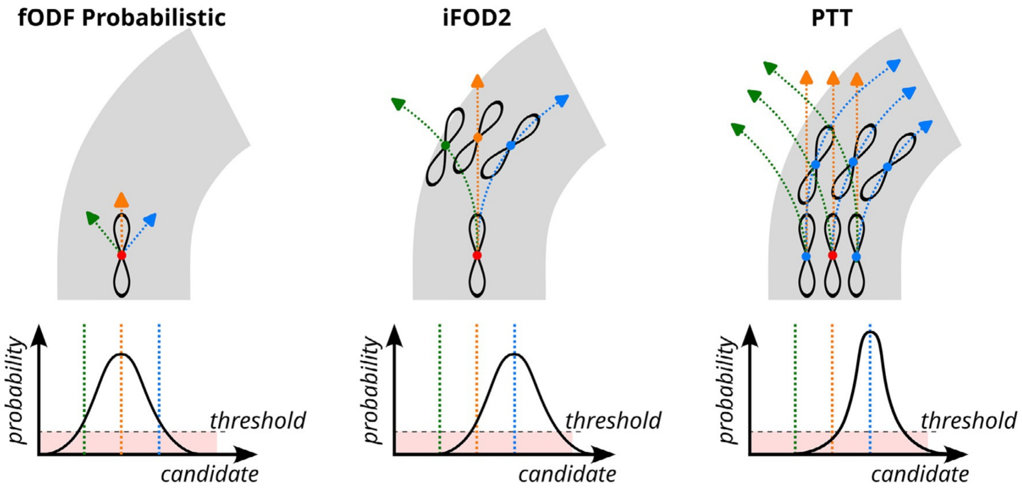

Figure 2.23: Comparison of three probabilistic tractography algorithms (local fODF, iFOD2, and PTT) starting from a red seed point. Three candidate directions (green, orange, blue) are evaluated at each propagation step, and representative probabilities for following the colored trajectories are displayed for each method. The first method uses only current FOD amplitudes; iFOD2 incorporates FODs along arcs, and PTT considers FODs within cylindrical probes (only the blue probe candidates are shown). Candidates below a threshold are rejected, while those above may be accepted depending on their probability. From (Girard et al., 2025).

Tractography (ACT) (Smith et al., 2012) uses tissue-segmented maps derived from structural MRI (usually T_1-weighted images) to ensure that streamlines originate and terminate in GM, while traversing WM, and to prevent propagation through CSF or non-brain regions. *Surface-Enhanced Tractography (SET)* (St-Onge et al., 2018) further improves cortical correspondence of tract endpoints by constraining seeding and termination directly on the reconstructed cortical surface.

Local tractography thus provides an efficient and flexible framework for reconstructing WM pathways, though it remains sensitive to noise, partial volume effects, and local modeling errors. These limitations motivated the development of semi-global and global optimization-based approaches, discussed in the following sections.

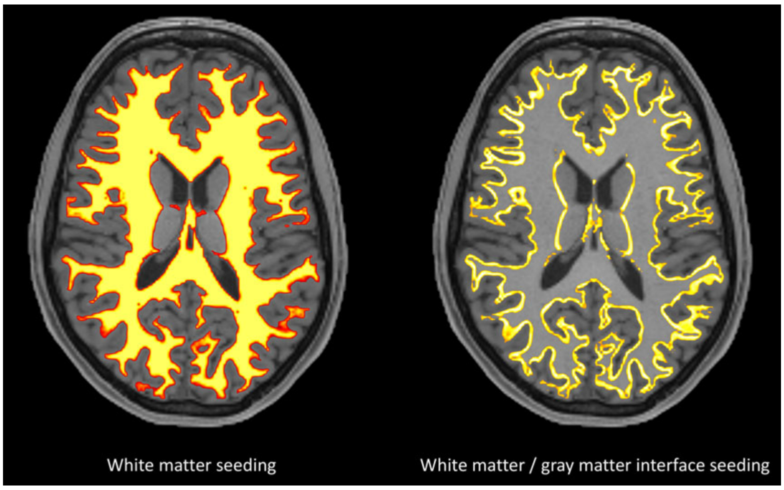

Figure 2.24: Whole-brain tractography can be performed by seeding either within the whole WM (left) or at the WM-GM boundary (right), the latter corresponding to the regions where fibers originate. From (Jeurissen et al., 2019).

2.3.2.3 Semi-global tractography methods

Semi-global tractography methods aim to overcome some intrinsic limitations of purely local tracking by incorporating contextual information over larger spatial scales. While local algorithms propagate streamlines based only on the current voxel's diffusion orientation, semi-global approaches integrate information from neighboring regions or optimize trajectories according to a global criterion defined over the diffusion field (Florack et al., 2025; Hagmann et al., 2003; Poupon et al., 2000). They thus offer a compromise between the efficiency of local methods and the robustness of fully global approaches.

A prominent class of semi-global techniques is *geodesic tractography*, which formulates fiber tracking as the problem of finding minimal paths on a Riemannian manifold derived from diffusion data (Florack et al., 2025; Sengers et al., 2021). WM tracts are interpreted as the *shortest paths* between two points with respect to a cost function reflecting local anisotropy and orientation coherence. The metric is typically defined from the diffusion tensor or FOD, so that propagation along well-aligned, anisotropic directions accumulates lower cost. By penalizing abrupt angular deviations, geodesic tractography yields smoother and more anatomically consistent reconstructions than purely local methods.

Several numerical strategies exist to estimate these optimal trajectories. *Front-propagation algorithms* (Jbabdi et al., 2008; Parker et al., 2002) simulate the evolution of a propagating interface from a seed region, where local diffusion properties determine propagation speed (Figure 2.25). The resulting arrival-time map encodes the minimal-cost field, from which optimal paths are recovered by gradient descent. Alternatively, *graph-based methods* (Zalesky, 2008) represent the diffusion field as a weighted graph, with voxels as vertices and edges encoding inter-voxel transition costs based on local coherence or anisotropy. Shortest paths are then computed using algorithms such as Dijkstra's, providing an intuitive and efficient formulation.

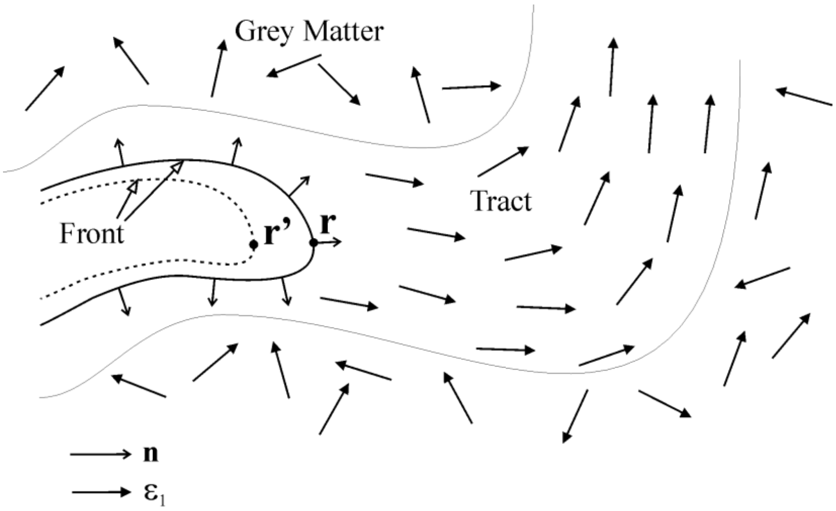

Figure 2.25: Illustration of vectors used in computing the speed function of front-propagation tractography algorithms. In WM tracts, the principal diffusion eigenvector (arrow) shows strong directional coherence, whereas in GM this directional organization is largely absent. From (Parker et al., 2002).

In summary, semi-global techniques extend the streamline framework by enforcing path optimality over spatially extended neighborhoods. They offer greater continuity and robustness in complex regions while remaining computationally manageable. Nonetheless, their accuracy is still limited by the ill-posed nature of the diffusion inverse problem, as modeling errors, noise, and limited resolution can distort the cost space, leading to anatomically implausible trajectories.

2.3.2.4 Global tractography methods

As discussed in the previous sections, local and semi-global tractography methods reconstruct streamlines by stepwise propagation following voxel-wise fiber orientations. While computationally efficient and widely adopted, these techniques are inherently limited by their local nature: each propagation step depends only on the immediately surrounding diffusion information, making them susceptible to noise, modeling inaccuracies, and local ambiguities in regions where fibers cross or fan out. *Global tractography methods* address these limitations by formulating tractography as a global optimization problem in which the entire set of streamlines is estimated at the same time to best explain the observed diffusion signal (Daducci et al., 2025; Mangin et al., 2013; Reisert et al., 2011). In this context, the term *global* refers to three key aspects that distinguish these methods from local ones: the use of all diffusion data simultaneously during estimation, the joint optimization of all trajectories rather than their independent propagation, and the requirement that the resulting tractogram collectively explains the measured signal.

Global tractography optimizes a configuration of trajectories whose cumulative contribution best explains the measured data. This estimation relies on two key components: a *forward model*, which predicts the diffusion-weighted signal generated by a given tractogram, and a *cost function*, which quantifies the mismatch between the predicted and observed data. Formally, the optimal tractogram $\mathbf{T}^*$ is given by:

$$\mathbf{T}^* = \underset{\mathbf{T}}{\operatorname{argmin}}\ \mathcal{E}(\mathbf{D}, \mathcal{M}(\mathbf{T})), \tag{2.18}$$

where $\mathbf{D}$ denotes the acquired dMRI data, $\mathcal{M}(\cdot)$ the forward model, and $\mathcal{E}(\cdot,\cdot)$ the energy function evaluating their similarity (Daducci et al., 2025). The forward model often employs spherical convolution to predict each streamline's

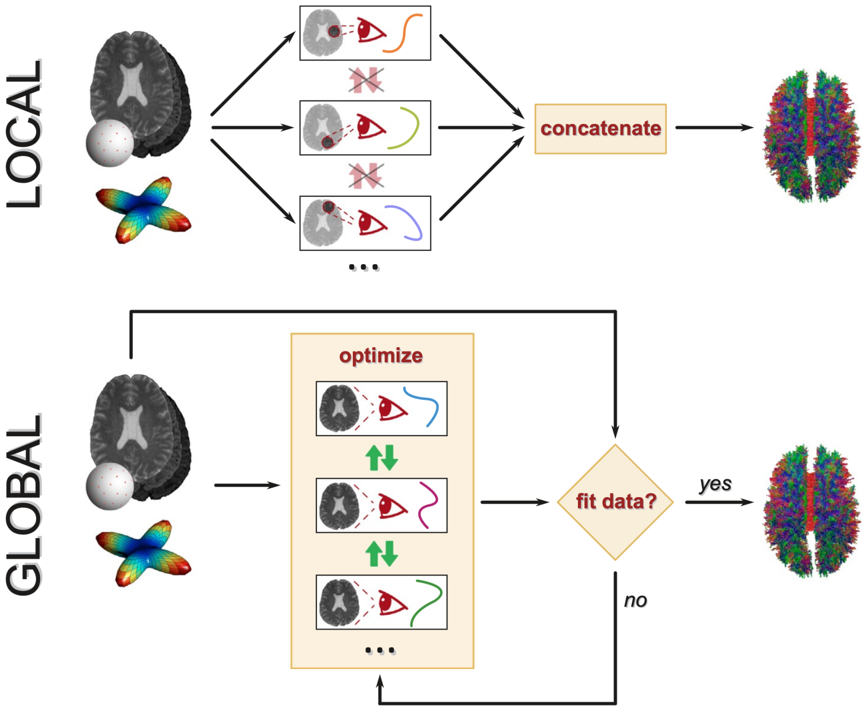

Figure 2.26: Illustration of the distinction between local and global tractography strategies. Local tractography reconstructs each streamline independently using only nearby diffusion information, and the complete tractogram is formed by combining all streamlines. Global tractography, on the other hand, simultaneously estimates all streamlines by fitting the entire tractogram to the full dMRI dataset, optimizing trajectories to best match the observed signal. From (Daducci et al., 2025).

contribution based on its position and orientation, potentially including additional compartments such as extra-axonal or isotropic components. Some variants adopt an inverse formulation, where voxel-wise diffusion models are first estimated and then compared with streamline-derived orientations. Given the noise and degeneracy of dMRI, multiple tractogram configurations may fit the data equally well, making the problem ill-posed. To constrain the solution space, global methods include *regularization* terms that enforce desirable properties such as smoothness, sparsity, or anatomical plausibility, balancing data fidelity with biological realism.

As illustrated in Figure 2.27, global tractography algorithms can be broadly divided into two complementary categories according to how they optimize the global objective function: generative and discriminative approaches (Daducci et al., 2025). Both rely on the same underlying principle — estimating the configuration of trajectories that best explains the measured diffusion signal — but differ in whether they construct the tractogram directly from the diffusion data or refine an existing set of candidate streamlines. *Generative* methods adopt a bottom-up strategy, reconstructing WM pathways from their elementary building blocks. They begin with a large collection of short fiber segments, each representing a local portion of a tract and associated with a predicted signal contribution derived from the forward model. Through iterative optimization, these fragments are progressively displaced, reoriented, and linked to form continuous, smooth trajectories whose cumulative signal best reproduces the measured data. In this framework, both the geometry and the number of streamlines are inferred directly from the diffusion signal itself, allowing the model to synthesize a tractogram that naturally emerges from the data without requiring a predefined set of trajectories. In contrast, *discriminative* (or top-down) methods start from a precomputed whole-brain tractogram, typically obtained through local tracking, and aim to globally adjust its fit to the diffusion data (see also Section 2.4.1). Rather than generating streamlines, they treat each candidate trajectory as a potential contributor to the measured signal. The forward model is used to estimate the signal each streamline would produce, assuming a constant contribution along its length. The optimization then assigns a weight to each streamline, modulating its contribution so that the aggregate prediction across all streamlines best matches the empirical data. This approach reframes global tractography as a data-driven filtering or reweighting problem, where the optimal solution emphasizes anatomically and physically plausible trajectories while discarding implausible ones.

As said before, *generative* global tractography reconstructs WM pathways by directly inferring the configuration of streamlines that best explains the measured dMRI signal through a forward model. Rather than propagating trajectories from predefined seeds, these methods start from an initial random

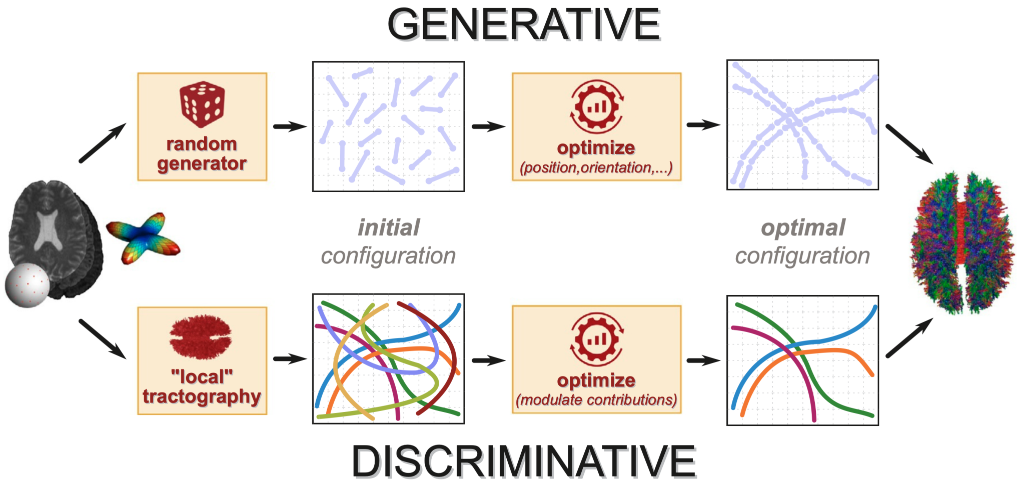

Figure 2.27: Illustration of generative versus discriminative approaches in global tractography. Generative (or ”bottom-up“) methods construct optimal streamline configurations by starting from random short segments, which are guided to form smooth, continuous trajectories that best account for the measured dMRI signal. Discriminative (or ”top-down“) methods begin with an initial tractogram obtained from local tractography and adjust the contribution of each streamline to maximize agreement with the observed diffusion data. From (Daducci et al., 2025).

distribution of short fiber segments and iteratively adjust their position and orientation to form smooth, data-consistent trajectories. Due to the problem's large dimensionality and nonlinearity, stochastic optimization techniques are typically employed. A first example is the *spin glass model* (Mangin et al., 2002), where the tractogram is represented as a dense set of short, oriented segments, analogous to magnetic spins, that interact both with the local diffusion field and with neighboring segments. The global energy minimized during optimization combines an external term, encouraging alignment with principal diffusion directions, and an internal term, enforcing smoothness between adjacent segments. Later developments enabled multiple, freely positioned spins per voxel, allowing for the representation of crossings and complex geometries (Fillard et al., 2009; Kreher et al., 2008; Reisert et al., 2011). While highly expressive, this model involves a huge parameter space and poses a challenging optimization problem. The *Gibbs tracking* framework (Kreher et al., 2008; Reisert et al., 2011) refined this idea by introducing simulated annealing to drive the system toward an optimal low-energy configuration (Figure 2.28). Random modifications, such as adding, removing, or perturbing individual segments, are proposed and accepted with a probability dependent on their energy change and a gradually decreasing temperature. At high temperature, the model explores diverse configurations, whereas cooling progressively stabilizes the system around a globally consistent tractogram. This probabilistic formulation improves convergence and robustness, making generative global tractography computationally feasible and anatomically more coherent.

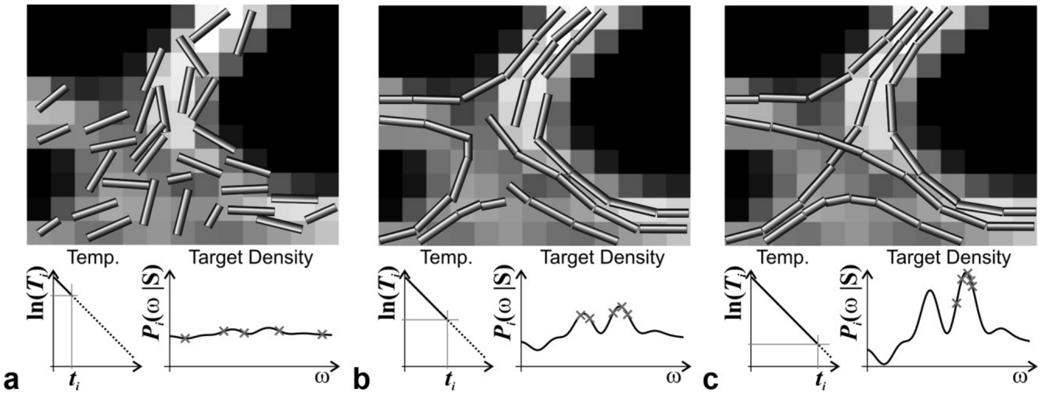

Figure 2.28: Illustration of the Gibbs tracking method. (a) At very high temperatures, cylinder configurations are largely random and unstructured. (b) At intermediate temperatures, configurations in regions of higher probability are favoured, while maintaining some variability. (c) At temperatures near zero, only configurations near local optima are sampled, producing highly structured cylinders with minimal variation. From (Kreher et al., 2008).

2.3.2.5 Limitations of tractography

Tractography allows non-invasive reconstruction of WM pathways, yet its accuracy is limited at every stage of the processing pipeline due to the indirect and ill-posed nature of inferring axonal trajectories from diffusion signals.

These signals reflect only the average displacement of water molecules within each voxel rather than imaging axons directly, so all subsequent modeling and tracking steps rely on assumptions that can lead to multiple, non-unique solutions (Hubbard and Parker, 2014; Jones et al., 2013; Mangin et al., 2013; Rheault et al., 2025b). The finite spatial resolution of dMRI voxels, which is several orders of magnitude larger than individual axons, introduces partial volume effects that are particularly problematic in regions of crossing, fanning, or converging fibers (Hubbard and Parker, 2014; Jeurissen et al., 2013). Even high-quality acquisitions cannot fully resolve small or short-range connections, and measured signals are further degraded by noise, motion, and other imaging artifacts. Consequently, tractography remains a model-based inference rather than a direct measurement of axonal connectivity.

A fundamental unresolved limitation of tractography is the *absence of ground truth* in vivo (Hubbard and Parker, 2014; Jones, 2010a; Rheault et al., 2025b). Streamline reconstructions cannot be directly verified against true anatomical connections in living brains. Ex vivo techniques, such as axonal tracing and postmortem dissection, allow micro- or macro-scale validation (Jeurissen et al., 2019), but these methods are invasive, limited to specific pathways, and cannot be applied to live subjects. Physical and software phantoms provide controlled environments with known ground truth (Hubbard and Parker, 2014; Schilling et al., 2019b), yet they only approximate biological tissue and cannot fully reproduce the structural complexity of the human brain.

Tractography is fundamentally an *ill-posed inverse problem*, meaning that multiple distinct solutions can equally explain the measured diffusion signal, and even minor perturbations in the input data, such as noise, may lead to substantially different results. Indeed, multiple fiber configurations can produce virtually identical diffusion signals at the voxel level, allowing errors to propagate during the streamline reconstruction process. Regions with complex fiber organization are particularly prone to misestimation, resulting in both false positives and false negatives (Hubbard and Parker, 2014; Rheault et al., 2020).

Algorithmic choices also shape reconstruction outcomes. As seen in Section 2.3.1.2, advanced local modeling techniques, such as CSD, improve the estimation of fiber orientations but remain limited by voxel-level ambiguities and angular resolution constraints (Rheault et al., 2025b). Moreover, the chosen tractography approach highly influences the results: deterministic methods tend to produce sparse, incomplete tractograms that miss valid connections, whereas probabilistic algorithms generate denser reconstructions, but at the cost of increased false positives (Zalesky et al., 2016). Consequently, streamline counts are strongly influenced by tracking parameters, local modeling assumptions, and algorithm design, and are therefore unreliable as quantitative indicators of structural connectivity (Girard et al., 2014; Jeurissen et al., 2013) (see also Section 2.4).

Comparative studies and community challenges have shown that most algorithms recover a majority of true fiber bundles but also generate substantial numbers of spurious connections, sometimes exceeding true positives by several fold (Maier-Hein et al., 2017; Schilling et al., 2019b). Achieving high sensitivity without inflating false positives remains a major challenge. To address this, post-processing methods, along with the integration of anatomical priors or multimodal data, can improve specificity and reduce spurious streamlines (Daducci et al., 2016). Nevertheless, their effectiveness is ultimately constrained by the inherent ambiguities of the inverse problem and by limitations of the initial tractogram (see Sections 2.4.1 and 2.4.2).

In addition to these challenges, tractography outcomes are influenced by several systematic algorithmic biases, some of which are illustrated in Figure 2.29 (Zhang et al., 2022). A *curvature overshoot bias* occurs when numerical integration fails to follow sharp bends, causing streamlines to overshoot or smooth out curved trajectories and deviate from the true anatomical course. The *termination bias* reflects the tendency of streamlines to stop prematurely or to extend into non-neuronal tissue when local diffusion information is weak or ambiguous; ACT (Smith et al., 2012) can alleviate but not fully remove this problem. The *connection-density bias* arises because the number of reconstructed streamlines is not proportional to the true number of axons: factors such as seeding density, FOD amplitude, and tracking thresholds can artificially inflate or suppress specific pathways (Zhang et al.,

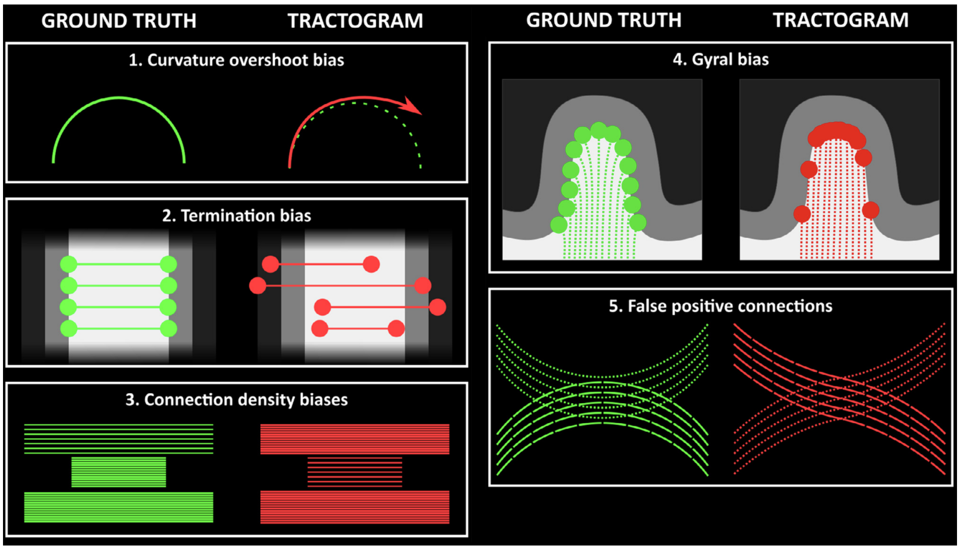

Figure 2.29: Representative examples illustrate errors and biases typical of fiber reconstruction compared to the ground truth. (1) Streamlines can overshoot the true pathway because low-order integration can underestimate curvature. (2) Reconstructed streamlines may terminate in implausible locations due to inappropriate anatomical constraints. (3) Streamline counts within a bundle do not necessarily reflect the underlying axonal density. (4) Due to the limited spatial resolution of dMRI, many streamlines may terminate at gyral crowns rather than being uniformly distributed across the cortex. (5) In regions of bundle intersection, streamlines may erroneously combine segments from different pathways, generating false-positive connections. Adapted from (Zhang et al., 2022).

2022). Finally, preferential termination at gyral crowns, referred to as *gyral bias*, underrepresents sulcal connections (Jeurissen et al., 2019; Schilling et al., 2018), while distance-dependent decay systematically reduces the detection of long-range pathways and exaggerates local shortcuts. These biases, together with voxel-level ambiguities, further limit the quantitative interpretability of tractography-derived connectivity measures (see also Section 2.4).

Voxel-level ambiguities interact with anatomical and geometric constraints, further complicating the reconstruction process. Many voxels contain multiple anatomically distinct bundles, particularly where fibers converge or branch, such as in the internal capsule or corona radiata. In these regions, the diffusion signal represents a mixture of orientations, making it difficult for algorithms to assign streamlines correctly, which can lead to premature terminations, misrouted trajectories, or artificial merging of distinct bundles (Jbabdi and Johansen-Berg, 2011; Jeurissen et al., 2019; Rheault et al., 2020). *Bottleneck regions*, where multiple distinct bundles converge within a few voxels (Figure 2.30), magnify these ambiguities by making it nearly impossible to disentangle individual pathways and consequently lead to the introduction of more invalid connections (Schilling et al., 2022b). Instead, *wall effects*, where streamlines are forced to travel along the boundaries of a voxel or tract (Figure 2.31), can artificially constrain or redirect trajectories away from their true anatomical course (Jeurissen et al., 2019; Rheault et al., 2020).

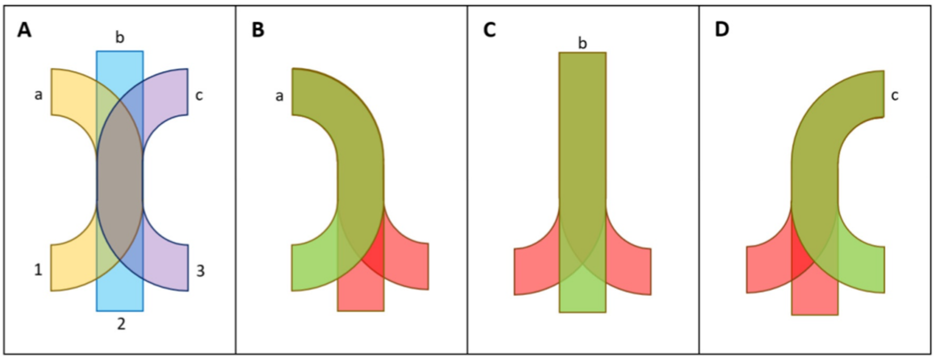

Figure 2.30: Illustration of the bottleneck effect. Three distinct bundles with separate endpoints converge in an overlapping WM region (A), where all fibres run locally parallel, creating directional ambiguity upon exit. With three possible origins and three destinations, nine configurations are feasible in principle (B–D), even though only three reflect the true underlying anatomy. From (Rheault et al., 2020).

Recognizing these challenges is essential not only for avoiding misinterpretation but also for understanding tractography's strengths, as doing so provides a constructive foundation for its continued improvement (Rheault et al., 2020, 2025b). Despite these limitations, tractography remains a crucial tool for mapping WM architecture, and ongoing methodological and acquisition advances promise to enhance its accuracy and reliability in both basic

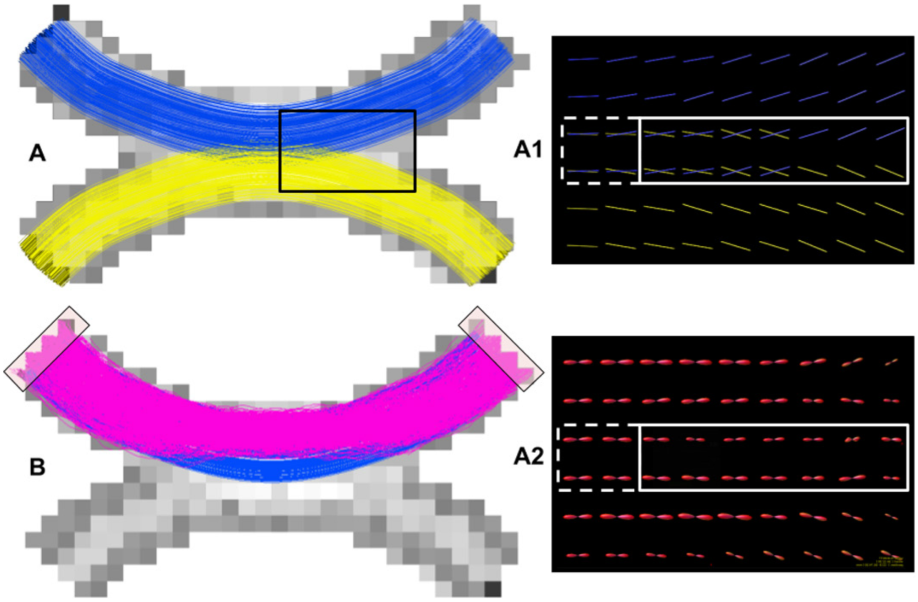

Figure 2.31: Illustration of the wall effect using simulations. (A) Ground truth showing two bundles that briefly converge ("kissing"), with the true vector fields displayed in (A1). In (A2), the FODs reconstructed from the same area using CSD are shown. The white boxes indicate the wall effect, i.e., regions where multiple orientations should appear but only one is detected, while the dotted boxes highlight locations where a single orientation is correctly expected. (B) Pink streamlines generated by probabilistic tractography show reduced volume compared to the blue ground truth, with the lower arc segment missing due to the wall effect. From (Rheault et al., 2020).

and clinical neuroscience.

2.3.3 From tractograms to structural brain networks

Once the fiber pathways have been reconstructed through tractography, they can be used to build the *structural connectome*, a network representation of WM connectivity linking distinct GM regions (Sotiropoulos and Zalesky, 2019; Sporns, 2014; Yeh et al., 2021; Zalesky et al., 2025). As illustrated in Figure 2.32, in this framework, the brain is modeled mathematically as a graph, where *nodes* correspond to cortical and subcortical Region of interest (ROI), and *edges* represent WM pathways inferred from the streamlines connecting pairs of regions (Bullmore and Bassett, 2011; Hagmann, 2005; Sporns et al., 2005). Unlike single-tract analyses, the connectome provides a system-level description of brain wiring, enabling studies of network organization, inter-individual variability, and the impact of development, aging, or pathology (Sotiropoulos and Zalesky, 2019).

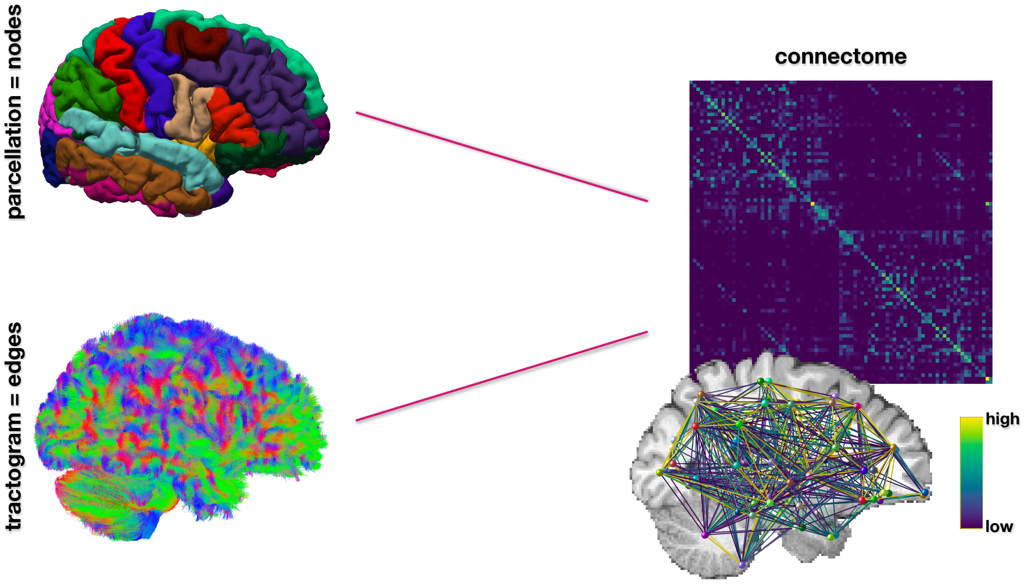

Figure 2.32: Cortical and subcortical GM regions are first parcellated into distinct nodes using an anatomical atlas (top left). Whole-brain tractography is then used to infer WM pathways between node pairs (bottom left), where each reconstructed streamline contributes to a specific connection (edge). The resulting symmetric adjacency matrix (as tractography cannot resolve fiber directionality) is a macroscale representation of the structural connectome (right).

To define the graph *nodes*, the GM is parcellated into anatomical or data-driven ROIs, according to an atlas, like those shown in Figure 2.33 (Cammoun et al., 2012; Desikan et al., 2006; Destrieux et al., 2010; Hagmann et al., 2007). In the most common approach, an anatomical atlas is registered to the subject's T_1-weighted MRI, and voxels are assigned to region labels appropriately (Sotiropoulos and Zalesky, 2019). Atlas choice is nontrivial: coarse parcellations lead to sparser macroscale networks, whereas high-resolution or data-driven schemes can increase network richness at the expense of reproducibility. Furthermore, parcellations derived from functional or structural criteria may segment the brain along different organizational principles, resulting in connectomes that are qualitatively distinct even when built from the same diffusion data (Messaritaki et al., 2019).

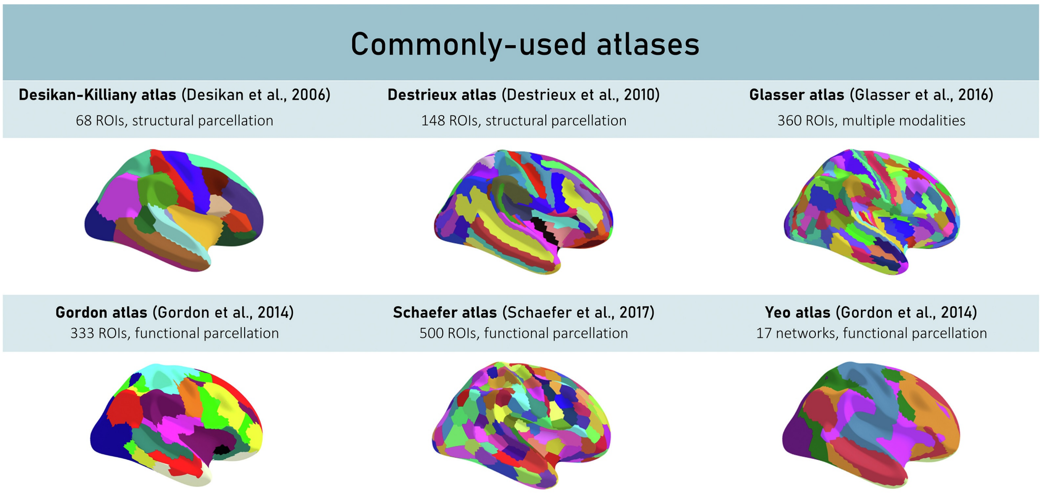

Figure 2.33: Surface-based representations of cortical parcellations are used to define network nodes according to different atlases. Shown are examples of coarse (e.g. Desikan–Killiany) and higher-resolution (e.g. Destrieux) anatomically defined parcellations, and functionally derived atlases (e.g. Yeo). Adapted from (Fürtjes et al., 2023).

Once the ROIs are defined, streamlines from the tractogram are assigned to pairs of nodes to determine the graph *edges*. The simplest approach considers only the endpoints of each streamline to specify its corresponding ROI pair, although streamlines may terminate just short of a region boundary due to partial-volume effects (Yeh et al., 2021). Heuristic strategies, therefore, assign each streamline to the nearest ROI within a search radius, ensuring each streamline contributes to exactly one connection (Smith et al., 2015b). Alternative strategies also consider whether streamlines traverse an ROI's volume, which can capture long-range connections more inclusively, but, in this way, a single tract will contribute to multiple edges, increasing the number of connections unrealistically (Yeh et al., 2019). These methodological choices shown in Figure 2.34 influence the resulting connectome even before edge weights are assigned; strategies for weighting edges are discussed in detail in Section 2.4.

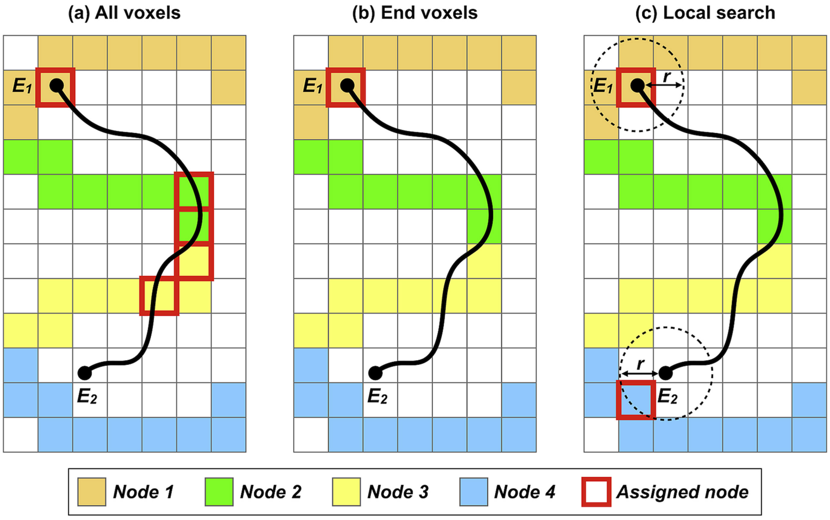

Figure 2.34: Different node (colored voxels) assignment strategies used to determine how tractography streamlines (black curves) are mapped to network edges (endpoints denoted E1 and E2). (a) All-voxels: any ROI intersected along the streamline trajectory is counted. (b) Endpoint-only: a streamlines contributes to connectivity only if both endpoints lie within labeled ROIs. (c) Local-search: endpoints are assigned to the nearest ROI within a defined neighborhood radius. From (Yeh et al., 2019).

The resulting adjacency matrix constitutes the structural connectome, which can be analyzed with *graph theory* to characterize the network's organization (Bullmore and Sporns, 2009; Fornito et al., 2016). It can be considered as an undirected binary graph, reflecting only the presence or absence of connections, or as a weighted graph, where edges encode a measure of connection strength (Yeh et al., 2021). Weighted graphs allow richer analyses but are more sensitive to modeling assumptions. Metrics such as global efficiency, clustering coefficient, modularity, and connection strength quantify aspects of large-scale communication capability, local specialization, and network organization (Zalesky et al., 2025). These measures are employed for comparisons between subjects or groups, allowing investigations into how structural wiring supports cognition or is altered in disease. In this way, tractography-based connectomics provides a bridge between microscopic WM architecture and macroscopic systems-level brain function, while remaining model- and parameter-dependent and subject to the methodological limitations discussed in Section 2.3.2.5 (Jones et al., 2013; Mangin et al., 2013; Rheault et al., 2020).

In all cases, the resulting network is a model rather than a direct observation of biology. Its structure reflects algorithmic choices, parcellation scheme, and tractography parameters. *Validation* therefore remains a major challenge: while group-level patterns of connectivity have shown reasonable consistency across studies, direct subject-level ground truth is unavailable in vivo (Fornito et al., 2016; Sotiropoulos and Zalesky, 2019). Reproducibility is highly dependent on the chosen pipeline, including preprocessing, parcellation, and tractography methods. Current approaches to improve robustness include the use of standardized pipelines, cross-validation across datasets, and multimodal integration (e.g., combining dMRI with functional or anatomical data), but even these strategies cannot fully overcome the inherent ambiguities in streamline reconstruction or node definition. Consequently, structural connectomes should be interpreted as probabilistic representations of connectivity rather than definitive maps of anatomical connections (Sotiropoulos and Zalesky, 2019).

Finally, while the presence or absence of connections defines the network structure, quantifying the strength of edges remains an open methodological challenge. Choices about how to assign weights can significantly affect the interpretation of the network and downstream analyses based on graph theory.

2.4 The quantification problem in tractography

As discussed in Section 2.3.2, tractography algorithms reconstruct continuous trajectories through dMRI data by combining local fiber orientation estimates. However, it is important to emphasize that these methods do not reconstruct individual nerve fibers or bundles; instead, they generate pathways along which many axons are presumed to run in parallel (Jones et al., 2013; Zhang et al., 2022). These streamlines are used qualitatively to visualize major WM tracts and quantitatively to define regions of interest or estimate the degree of connectivity between brain regions (Conturo et al., 1999; Kaden et al., 2007). Nevertheless, orientation information alone is insufficient for accurate *quantification* of WM connections. It requires microstructural information beyond orientation, including axon density, diameter, and myelin content, which can be partially estimated with advanced dMRI techniques or complementary modalities such as quantitative magnetization transfer and multi-component relaxometry (Jones et al., 2013).

A central challenge in tractography-based connectomics is quantifying connection strength. Traditionally, the most common approach has been to define edge weights as the *number of streamlines (NOS)* reconstructed between pairs of GM regions (Jones et al., 2013). Yet, even when the underlying number of axons is constant along a pathway, the number of reconstructed streamlines can vary substantially depending on tract length, curvature, branching, or local SNR (Jones, 2010a). This means that the NOS is not a biologically faithful proxy for actual axon count. Two bundles with identical information-carrying capacity (e.g., straight vs. curved) are therefore not expected to differ, yet tractography would typically report different streamline counts. For this reason, interpreting streamline count as "fiber count" (i.e., true axon number) is misleading and should be avoided. Likewise, the number of streamlines passing through a voxel should not be interpreted as "fiber density," as it is similarly modulated by non-biological factors (Yeh et al., 2021; Zhang et al., 2022).

Several technical factors contribute to this discrepancy. First, the intrinsic limitations of dMRI and tractography introduce biases in streamline reconstruction. As mentioned in Section 2.3.2.5, algorithmic parameters, including step size, curvature thresholds, seeding density and strategy, and the choice of local fiber orientation model, substantially influence both the number and trajectory of reconstructed streamlines (Smith et al., 2022). In particular, longer fibers are subject to underestimation due to the accumulated propagation errors, while uniform seeding strategies may lead to overestimation (Maier-Hein et al., 2017). Additional biases arise during the estimation of FODs; for example, the sharpness of the FOD, the quality and gradient amplitudes, and the presence of complex fiber configurations all affect which streamlines propagate and which terminate prematurely (Jones et al., 2013).

These technical limitations have direct implications for downstream analyses. Because connectivity matrices are typically populated by streamline counts, edge weights derived from uncorrected tractograms can misrepresent the true WM architecture (Yeh et al., 2021). This misrepresentation can propagate into graph-theory metrics, such as global efficiency, modularity, and hub identification, potentially leading to erroneous interpretations of network organization or group differences (Fornito et al., 2016). Moreover, the reproducibility of structural connectomes is highly sensitive to the tractography algorithm, seeding strategy, and post-processing choices, making cross-study comparisons challenging (Smith et al., 2022; Yeh et al., 2021).

To mitigate these limitations, tractography can be combined with quantitative microstructural information, an approach commonly referred to as *tractometry* (Bells et al., 2011; Sotiropoulos and Zalesky, 2019). In tractometry, microstructural metrics such as Fractional Anisotropy, Mean Diffusivity, or neurite density indices are sampled along the trajectory of each streamline and then aggregated across the bundle, yielding a more biologically informative estimate of connection strength than raw streamline counts. A complementary strategy is to analyze the distribution of microstructural values along the trajectory rather than collapsing it into a single scalar. This approach requires appropriate sampling or parameterization (Bells et al., 2011; Colby et al., 2012; Yeatman et al., 2012) and enables along-tract profiling, characterizing spatial variations either along the fiber axis or across its cross-section.

More advanced microstructure informed tractography methods, explicitly reweight or optimize streamline contributions to better reflect the underlying tissue properties and measured diffusion signal, partially correcting for the biases inherent in conventional streamline counts (Daducci et al., 2015; Pestilli et al., 2014; Smith et al., 2013).

2.4.1 Microstructure informed tractography

Microstructure informed tractography refers to a class of methods that exploit biophysical tissue models to infer not only the geometry of WM tracts but also the quantitative contribution of each streamline to the acquired dMRI (Daducci et al., 2016). Standard tractography techniques consider the reconstructed streamlines as simple lines, ignoring the rich microstructural information present in the dMRI data. In contrast, to provide a more biologically accurate estimation of brain connectivity, microstructure informed tractography approaches interpret the acquired diffusion signal as a function of the microstructure represented by the set of streamlines, and fit the tractogram to the data via global optimization (Figure 2.35). For this reason, microstructure informed tractography belongs to the *discriminative* class of *global methods* (see Section 2.3.2.4 for more details): these top-down techniques operate on an existing tractogram and estimate the contribution of each streamline to explaining the diffusion signal, pruning or reweighting the tractogram accordingly (Daducci et al., 2016).

2.4.1.1 SIFT

The *Spherical-deconvolution Informed Filtering of Tractograms (SIFT)* method does not directly model the complete dMRI signal, but it assumes that the amplitude of each lobe of the FOD, estimated by CSD, is proportional to the true intra-axonal volume oriented along that direction (Smith et al., 2013). To preserve this proportionality, the diffusion signal must not be normalized to the b=0 image, FOD amplitudes must retain their absolute scale. Moreover, SIFT assumes that each streamline represents a portion of axonal cross-section and contributes uniformly to tissue volume per unit length (Smith et al., 2013). Under these premises, an unbiased tractogram

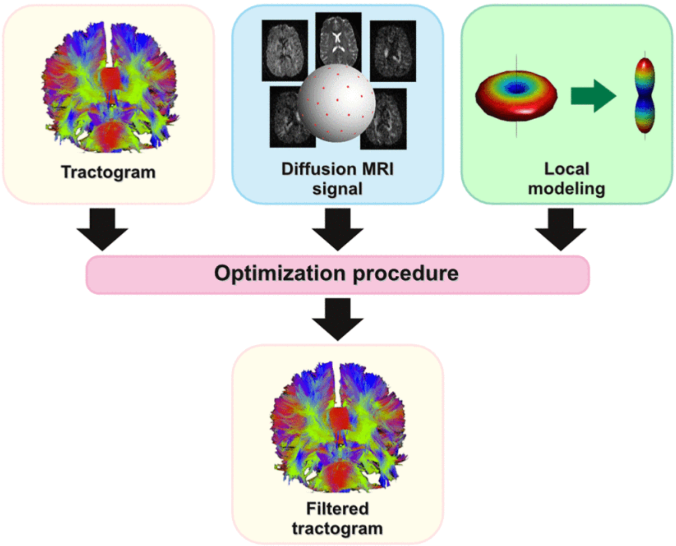

Figure 2.35: Diagram illustrating the top-down approach of microstructure informed tractography methods. The final, refined tractogram is obtained by combining, via a global optimization procedure, the streamlines generated by a standard algorithm with local tissue properties and the acquired diffusion MRI signal. From (Daducci et al., 2015).

should exhibit a streamline density in each voxel and direction that matches the corresponding FOD lobe integral, as illustreted in Figure 2.36.

SIFT introduces a *proportionality coefficient*

$$\mu = \frac{\sum_V \left(PM_V \sum_l FOD_{V,\, l} \right)}{\sum_V \left(PM_V \sum_l TD_{V,\, l} \right)}\,, \tag{2.19}$$

which reascales the raw track density $TD_{V,\, l}$ (sum of streamline segments per lobe l in voxel V, restricted to the processing mask PM) to the same units as the FOD integral $FOD_{V,\, l}$. The ideal condition enforced by the algorithm is

$$\forall\ \{V : PM_V > 0,\ l\} :\ \ \mu \cdot TD_{V,\, l} = FOD_{V,\, l} \tag{2.20}$$

and deviations from this equality indicate inaccuracy in the fit, allowing the definition of the cost function

$$f = \sum_V \left(PM_V \sum_l \left(\mu \cdot TD_{V,\, l} - FOD_{V,\, l} \right)^2 \right)\,. \tag{2.21}$$

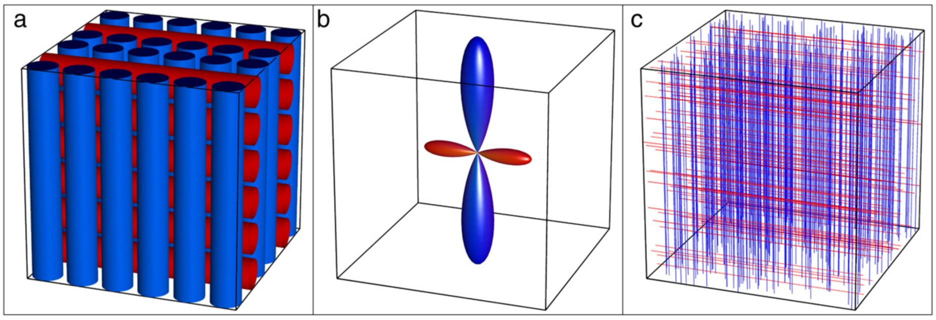

Figure 2.36: Schematic illustration of Spherical-deconvolution Informed Filtering of Tractograms (SIFT) principles. (a) A voxel contains two crossing fiber populations, with the volume of the inferior–superior bundle (blue) twice that of the left–right bundle (red). (b) The FOD amplitude is expected to reflect this ratio. (c) By assigning a volume per unit length to each streamline, an unbiased reconstruction should produce twice as many streamlines along the dominant fiber orientation as along the minor population. From (Smith et al., 2013).

This cost function can therefore be used to quantify how well the reconstruction of a streamline aligns with the underlying data (see Figure 2.37). Streamlines whose presence causes an excess of tract density with respect to the FOD (i.e. $\mu \; TD_{V,\,l} > FOD_{V,\,l}$) are therefore considered to violate the biophysical plausibility constraint and are iteratively removed. The removal process follows a greedy gradient-descent strategy: at each step, the streamline whose elimination is expected to produce the largest reduction in global cost is discarded (Smith et al., 2013). The algorithm does not recompute the full cost function after each removal, which would be computationally prohibitive. Instead, it uses efficient local updates to approximate each streamline's contribution to the mismatch, enabling millions of streamlines to be evaluated and pruned. In this way, the resulting filtered tractogram better matches the relative amplitudes of the underlying FODs. However, explicit removal reduces tractogram density, which may be undesirable in downstream applications.

To overcome this limitation, *SIFT2* (Smith et al., 2015a) keeps all stream-

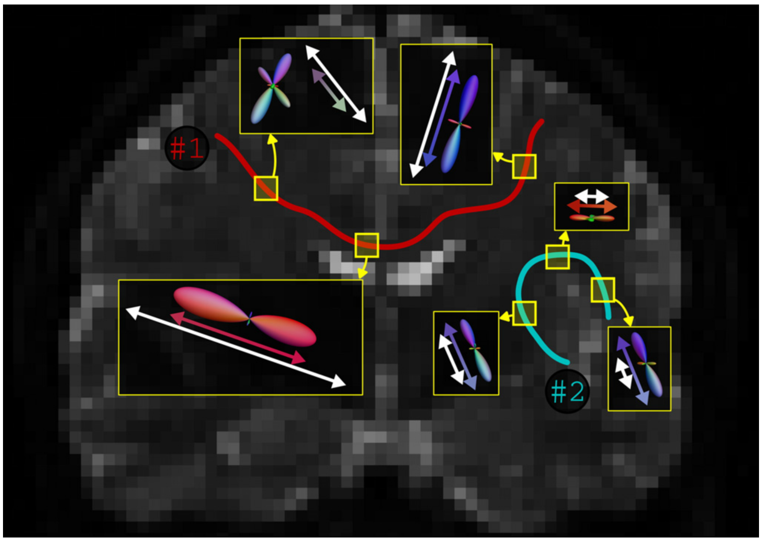

Figure 2.37: Illustration of the estimated change to the cost function from the removal of individual streamlines. For selected voxels (yellow squares), the FOD lobes are shown with colored bidirectional arrows, and the corresponding streamline contributions (densities normalised by μ) are shown as white arrows. For streamline 1 (red), densities exceed FOD lobe integrals, so its removal reduces the cost function. Instead, for streamline 2 (cyan), FOD integrals exceed densities, leading to an increase in the cost function if removed. From (Smith et al., 2013).

lines but estimates a weighting coefficient for each one, allowing tractography to remain dense while still enforcing quantitative consistency with the FOD. The track density in each lobe is redefined as

$$TD_l = \sum_{s:|s_l|>0} \left(|s_l| \cdot e^{F_s} \right) . \tag{2.22}$$

where $|s_l|$ denotes the length of streamline s assigned to lobe l, F_s is the weighting coefficient and e^{F_s} is the weighting factor. SIFT2 aims at optimize the coefficients F_s such that the weighted tractogram best matches the FOD amplitude in each direction, under the same proportionality factor μ. The estimation includes a regularization term that penalizes extreme weight deviations, enforcing smoothness and biological plausibility across neighboring streamlines. Unlike SIFT, which discards entire streamlines, SIFT2 preserves the full tractogram and instead allows the construction of a weighted connectome, where the weight of each individual streamline is interpretable as a proxy for its contribution to cross-sectional fiber area (Smith et al., 2015a).

2.4.1.2 LiFE

Linear Fascicle Evaluation (LiFE), rather than enforcing consistency with the FOD field, directly evaluates how well each streamline explains the measured dMRI signal (Pestilli et al., 2014). Specifically, it models the diffusion signal as a linear combination of the signal predicted by all streamlines and directly fits that model to the data.

For a diffusion gradient with direction θ and strength b, the signal attenuation from a single streamline segment f is modeled as

$$S(\theta, b) = S_0 \, e^{-bA_f(\theta)}, \tag{2.23}$$

where S_0 is the non–diffusion-weighted signal, and the ADC is

$$A_f(\theta) = \theta^T Q \, \theta, \tag{2.24}$$

with Q a positive-definite diffusion tensor locally aligned to the orientation of the fascicle segment. Because a typical voxel v contains multiple fascicles and possibly isotropic tissue, LiFE expresses the measured signal as a weighted sum of contributions:

$$S_v(\theta, b) = w_0 S_0 e^{-bA_0} + \sum_{f \in v} w_f \, S_0 \, e^{-bA_f(\theta)} \, , \tag{2.25}$$

where A_0 and w_0 model the isotropic compartment (e.g. CSF), and each w_f is the unknown, non-negative contribution of fascicle f. This can be rearranged into an isotropic baseline I_v plus orientation-dependent components $O_f(\theta)$:

$$S_v(\theta, b) = I_v \; + \sum_{f \in v} w_f \, O_f(\theta) \, , \tag{2.26}$$

LiFE then solves a global Non-Negative Least Squares (NNLS) problem:

$$\operatorname*{argmin}_{w_f \geq 0} \sum_v \sum_\theta \left(S_v(\theta, b) - I_v - \sum_{f \in v} w_f \, O_f(\theta) \right)^2 . \tag{2.27}$$

The solution provides biophysically interpretable weights for each streamline, reflecting its quantitative contribution to explaining the measured diffusion signal. Streamlines that do not improve the prediction receive weights approaching zero, effectively reducing the impact of implausible trajectories without deleting them from the tractogram (Pestilli et al., 2014).

2.4.1.3 COMMIT

Convex Optimization Modeling for Microstructure Informed Tractography (COMMIT) (Daducci et al., 2013, 2015) is a flexible framework that enables the combination of tractography with virtually any additive microstructural signal model to enhance the quality of the reconstructions. Like the other microstructure informed tractography methods, it starts from a superset of candidate streamlines generated using classical tractography algorithms. This is assumed to be a valid superset of anatomically plausible connections, since this class of techniques cannot create new streamlines but only remove those that are invalid. Each streamline is then assigned a weight reflecting its contribution to the measured signal, estimated by solving a convex optimization problem (Daducci et al., 2013, 2015).

The signal within each voxel is modeled as a linear combination of contributions from *multiple compartments*, depending on the forward model applied. In the original COMMIT formulation, it included a restricted intra-axonal compartment, a hindered extra-axonal compartment, and an isotropic compartment representing CSF (Panagiotaki et al., 2012). Therefore, the predicted diffusion signal $S(\boldsymbol{q})$ in a voxel is expressed as:

$$S(\boldsymbol{q}) = \sum_{s_i \in \mathcal{T}} f_i^{IC} R_i^{IC}(\boldsymbol{q}) + \sum_{s_i \in \mathcal{T}} f_i^{EC} R_i^{EC}(\boldsymbol{q}) + f^{ISO} R^{ISO}(\boldsymbol{q}) \,, \tag{2.28}$$

where R_i^{IC}, R_i^{EC}, and R_i^{ISO} are the signal profiles for the restricted, hindered, and isotropic compartments, and f_i^{IC}, f_i^{EC}, and f^{ISO} are their respective volume fractions. Each R_i^{IC} and R_i^{EC} is rotated to align with the local orientation of streamline s_i belonging to the input tractogram $\mathcal{T}$ and scaled by the actual length of the s_i segment crossing the voxel. The contributions of all streamlines within a voxel are summed to account for both restricted and hindered compartments.

COMMIT assumes that the measured dMRI image $\mathbf{I} \in \mathbb{R}^{n_x \times n_y \times n_z \times n_d}$, composed of n_d q-space measurements acquired across $n_v = n_x n_y n_z$ voxels, can be modeled as $\mathbf{I} = A(\mathcal{T}) + \eta$, where $A : \mathcal{T} \to \mathbf{I}$ is the *linear operator* describing the contribution of each streamline in $\mathcal{T}$ to the signal, and η accounts for noise and modeling errors. Given an input image $\mathbf{I}$, the aim is to find the set of fibers $\widetilde{\mathcal{T}}$ that best describes the data. As shown in Figure 2.38, this formulation can be represented in matrix form as a system of linear equations:

$$\mathbf{y} = \mathbf{A}\mathbf{x} + \eta \,, \tag{2.29}$$

where $\mathbf{y} \in \mathbb{R}_+^{n_v n_d}$ contains the concatenated diffusion measurements across all voxels, $\mathbf{A} \in \mathbb{R}^{n_v n_d \times n_c}$ encodes the multi-compartment forward model for all streamlines and other tissue contributions, $\mathbf{x} \in \mathbb{R}_+^{n_c}$ represents the *unknown non-negative weights* of each streamline (Daducci et al., 2015). The weights are estimated by solving a NNLS problem:

$$\underset{\mathbf{x} \geq 0}{\operatorname{argmin}} \, \|\mathbf{A}\mathbf{x} - \mathbf{y}\|_2^2 \,. \tag{2.30}$$

The matrix $\mathbf{A}$ is typically large and sparse, as each streamline intersects only a subset of voxels, and can be structured as a block matrix for multi-compartment models:

$$\mathbf{A} = [\mathbf{A}^{IC} \,|\, \mathbf{A}^{EC} \,|\, \mathbf{A}^{ISO}] \,, \tag{2.31}$$

where each block encodes the restricted, hindered, and isotropic contributions, respectively. The streamlines are assigned global weights, providing a quantitative measure of their contribution to the diffusion signal (Daducci et al., 2015). Streamlines with weights equal to zero are considered non-contributing and are removed, producing a refined, biologically plausible tractogram.

Figure 2.39 shows an illustrative synthetic *toy example* of the COMMIT forward model. In panel (A), the simulated diffusion data are modeled in each voxel with the represented FODs, from which three candidate streamlines

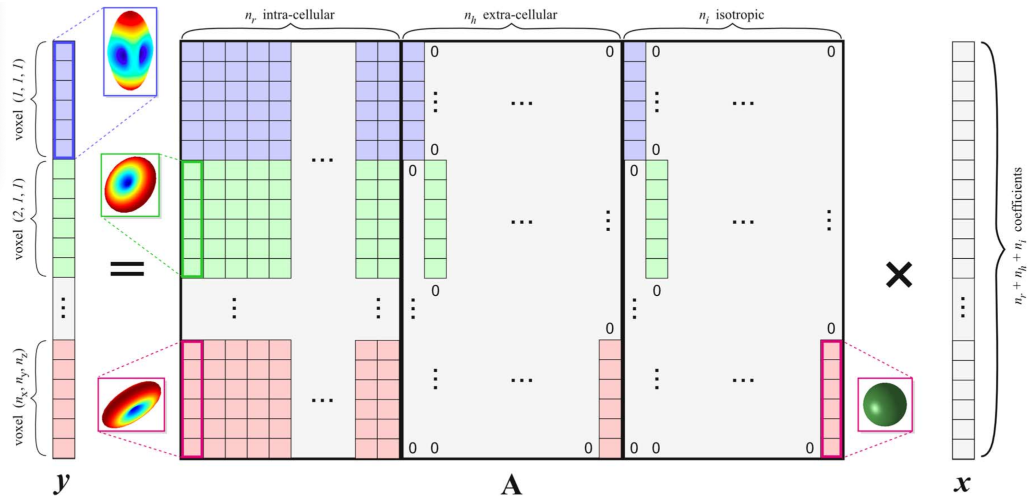

Figure 2.38: Conceptual overview of the COMMIT framework. The input streamlines (weighted by coefficients $\mathbf{x}$) are mapped to the measured dMRI signal $\mathbf{y}$ via the linear operator $\mathbf{A}$. In each voxel, the signal is expressed as the sum of restricted intra-axonal contributions from all intersecting streamlines, optionally complemented by local extra-axonal and/or isotropic compartments. From (Daducci et al., 2015).

are reconstructed. These streamlines form the input tractogram on which COMMIT operates. The chosen forward model consists of a "stick" compartment to capture the anisotropic intra-axonal signal associated with each streamline segment and a complementary "ball" compartment to account for potential isotropic signal. Panel (B) then details the construction of the linear system of Eq. 2.29. The vector $\mathbf{y}$ is formed by concatenating the simulated diffusion measurements from all voxels, while the matrix $\mathbf{A}$ is assembled by considering how each streamline intersects the voxel grid. In this case, fiber 1 passes through voxels 1 and 2, fiber 2 through voxels 1 and 3, and fiber 3 through voxels 2, 3, and 4. One column is created for each streamline, and in the rows corresponding to traversed voxels COMMIT inserts the anisotropic stick response oriented according to the local direction of the fiber; all other rows remain zero. To model isotropic contributions, four additional columns are appended, one per voxel, each containing a ball response exclusively in the row of its corresponding voxel. In this formulation, each column of $\mathbf{A}$ is controlled by a separate entry of $\mathbf{x}$, and the predicted signal is simply $\mathbf{Ax}$. According to matrix-vector multiplication, we can notice that in voxel 1, only the first two streamline contributions may be nonzero, while the CSF term must be zero; in voxel 2, the only compatible contribution is that of fiber 3; and similarly, fiber-specific weights are inferred in voxels 3 and 4. In this example, $\mathbf{x}$ is uniquely determined, and because the coefficient associated with fiber 3 is estimated as zero, that streamline is identified as a false positive and discarded from the tractogram.

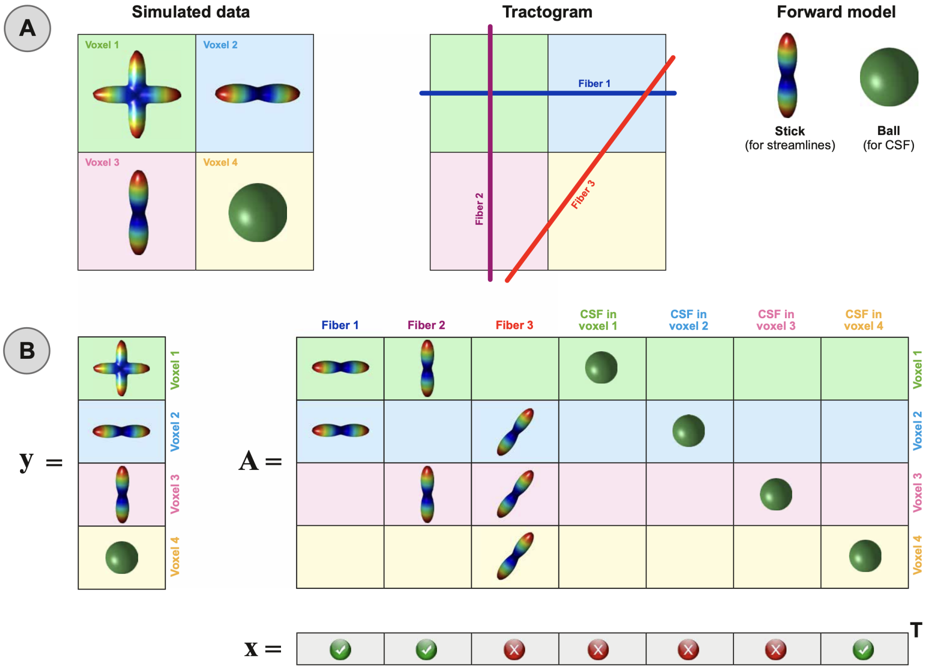

Figure 2.39: Synthetic toy example of COMMIT model. The acquired image (“Simulated data”) is vectorized in $\mathbf{y}$, while the potential tractogram contribution is stored in the matrix $\mathbf{A}$ according to the selected forward model. Finally, the vector $\mathbf{x}$ contains the coefficients estimated by COMMIT (for simplicity, here the entries are only 0s, i.e., non-compatible, and 1s, i.e., compatible). From (Schiavi et al., 2020).

2.4.1.4 Extentions of COMMIT

The original COMMIT framework was designed to assign physically interpretable microstructural weights to streamlines based solely on diffusion MRI. However, its formulation is flexible by design, and several extensions have been introduced to enhance anatomical accuracy or enrich the biophysical meaning of the resulting connectivity estimates. These developments can be broadly categorized into methods that (i) integrate multimodal or microstructural information beyond diffusion, and (ii) introduce anatomical priors to counteract known tractography limitations such as false positives (Daducci et al., 2025).

Standard tractography algorithms, including global methods, are known to produce a huge number of *false positive* streamlines (Maier-Hein et al., 2017), as illustrated in Figure 2.40. A key reason is that they are typically purely data-driven, relying exclusively on the dMRI signal without enforcing anatomical knowledge (Daducci et al., 2025). Building on the original formulation, *COMMIT2* (Schiavi et al., 2020) introduces anatomical priors reflecting the natural organisation of WM axons into macroscopic tracts connecting GM regions. Instead of treating streamlines as fully independent, they are grouped in bundles g, and their corresponding columns in the matrix $\mathbf{A}$ are regularized jointly using a group-lasso penalty:

$$\underset{x\geq 0}{\operatorname{argmin}} \ \|\mathbf{A}\mathbf{x}-\mathbf{y}\|_2^2+\sum_{g\in\mathcal{G}}\lambda^{(g)}\left\|\mathbf{x}^{(g)}\right\|_2, \quad \text{with } \lambda^{(g)}=\frac{\lambda\sqrt{|g|}}{\left\|\mathbf{x}_{\mathrm{NNLS}}^{(g)}\right\|_2}, \tag{2.32}$$

where $\mathcal{G}$ is a partition of the streamlines into groups (each connecting a pair of GM regions), $|g|$ is the group size, and λ controls the trade-off between data fitting and sparsity. This promotes solutions that explain the observed diffusion signal using the smallest number of anatomically meaningful bundles rather than an arbitrary collection of individually weighted streamlines (Schiavi et al., 2020). This formulation substantially increases specificity by suppressing false-positive bundles that are not required to fit the signal, thereby enhancing the anatomical plausibility of the final tractogram and aligning with the metabolic efficiency principle that prefers solutions with low energetic cost rather than the existence of all possible connections. (Bullmore and Sporns, 2012).

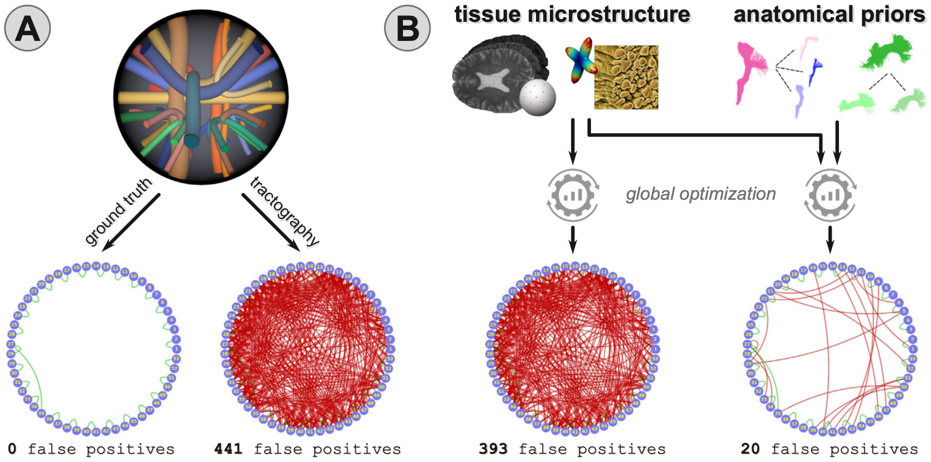

Figure 2.40: Standard tractography is prone to a high rate of false-positive connections, as shown on the synthetic simulation in panel A. Relying solely on microstructural information provides only limited improvement (B, left), whereas the integration of additional knowledge about WM organization substantially suppresses spurious pathways (B, right). From (Daducci et al., 2025).

This concept was further generalized into a *hierarchical* formulation, called *COMMIT2*$_{tree}$ (Ocampo-Pineda et al., 2021), in which streamlines are not grouped in a single partition but instead organized into a multilevel tree reflecting the branched structure of WM architecture. At the highest level, entire bundles are represented; at lower levels, sub-bundles and finer trajectory variants are progressively modelled. This variation allows discarding unplausible pathways belonging to real anatomical WM tracts; indeed, in COMMIT2 all streamlines belonging to the same group are promoted with non-zero weights. The regularization is accordingly defined over this new hierarchy, enabling the optimization to remove entire implausible bundles when sufficient evidence is lacking, while still allowing finer subdivisions to be retained when required to explain the data. This hierarchical prior further improves the balance between sensitivity and specificity, providing anatomically consistent tractograms that preserve valid projections into cortical regions while eliminating global false-positive structures that persist even after aggressive streamline-level filtering. In doing so, COMMIT2$_{\text{tree}}$ demonstrates that anatomical priors can be embedded at different levels of granularity while preserving the convexity, interpretability, and quantitative nature of the original COMMIT formulation.

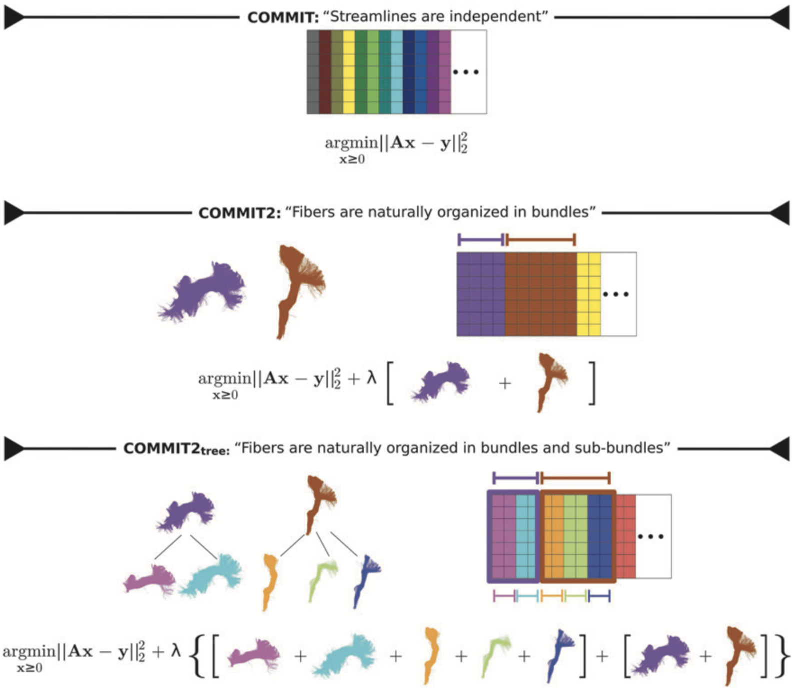

Figure 2.41: In the original COMMIT framework, streamlines are treated as independent elements. COMMIT2 introduces a regularization strategy that accounts for their natural grouping into bundles. COMMIT2$_{\text{tree}}$ further extends this idea by modeling a hierarchical organization, in which bundles can be subdivided into multiple levels of sub-bundles that are selectively promoted or penalized during optimization. From (Ocampo-Pineda et al., 2021).

Schiavi et al. (2022) proposed *Myelin Streamline Decomposition (MySD)*, an extension of COMMIT that replaces the diffusion signal with quantitative myelin-sensitive MRI maps, such as the Myelin Volume Fraction (MVF) from Magnetization Transfer Saturation (MTsat) or the Myelin Water Fraction

(MWF). In this formulation, the target vector $\mathbf{y}$ contains the voxelwise myelin content, and the forward operator $\mathbf{A}$ simply stores the length of each streamline segment inside each voxel. The estimated weights, therefore, correspond to myelin volume or water contribution per unit length of each streamline. These streamline-level myelin weights can then be aggregated at the bundle level by summing the total myelin volume attributed to the associated streamlines and normalizing by the total macroscopic bundle volume, yielding a bundle-specific myelin fraction (Schiavi et al., 2022). In vivo experiments on healthy controls confirmed that MySD can characterize both macroscopic bundles and cortical projections more precisely than traditional tractometry, which averages signal along the trajectory rather than attributing it to each streamline individually, as shown in Figure 2.42 (Daducci et al., 2025).

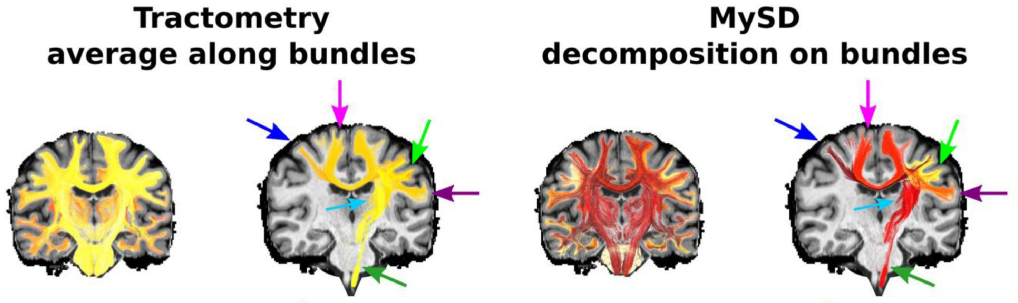

Figure 2.42: Whole-brain results and selected bundles of the left motor network are shown to compare myelin water fraction estimates using tractometry and MySD. MySD provides higher contrast between different bundles than tractometry. It also reveals higher myelination in bundles connecting the precentral gyri and in those linking the precentral gyrus to the medulla, compared to pathways connecting to subcortical nuclei, agreeing with previous findings. Adapted from (Schiavi et al., 2022).

A further extension of the framework incorporates microstructural heterogeneity by explicitly estimating the *axonal diameter* distribution within each streamline. This model, known as COMMIT$_{\text{AxSize}}$ (Barakovic et al., 2021a), replaces the single "stick" model with a dictionary of restricted diffusion kernels corresponding to multiple candidate axon calibres, each associated with a distinct intra-axonal signal response. In this formulation, each streamline can express its contribution not through a single coefficient but through a mixture of size-specific components, allowing the optimization to infer both the presence and the most plausible axon-diameter profile of every trajectory. This enables COMMIT to move beyond purely geometrical filtering and into quantitative microstructural characterization of long-range connections, providing estimates of bundle-specific axon calibre distributions directly from tractography (Daducci et al., 2025). In contrast to voxelwise axon-diameter mapping approaches, $\text{COMMIT}_{\text{AxSize}}$ performs this estimation along anatomically coherent pathways, thus resolving the contributions of intersecting fibre populations while respecting the continuity of individual tracts. As a result, this extension opens the possibility of combining tractography with biologically interpretable morphometric biomarkers, while preserving the convexity and interpretability of the original optimization framework (Barakovic et al., 2021a).

Microstructural properties of distinct fiber populations, such as T_2 *relaxation time*, cannot be inferred from dMRI alone. *COMMIT-T_2* (Barakovic et al., 2021b) extends the COMMIT framework to incorporate multi-echo diffusion-relaxometry data into the optimization. In contrast to voxelwise relaxometry methods, it assumes that T_2 is constant along individual streamlines, but may vary between different streamlines within the same voxel. Analogous to how $\text{COMMIT}_{\text{AxSize}}$ models axon caliber, multiple columns per streamline are defined in the forward model, each corresponding to a different candidate T_2 value. After solving the global optimization problem, each streamline is associated with a distribution of T_2 coefficients, representing the relative contribution of each candidate relaxation component. Proof-of-concept experiments showed that this formulation successfully recovers tract-specific relaxation profiles, even in challenging areas such as the three-way crossing between the corpus callosum, arcuate fasciculus, and corticospinal tract, a configuration frequently considered problematic for classical methods (Daducci et al., 2025). This demonstrates that tractography can serve not only as a geometric estimator of connectivity, but also as a spatial regularizer for multimodal microstructural inference.

Overall, these COMMIT extensions enhance the original framework, illustrating its *versatility* in combining tractography reconstructions with diverse sources of quantitative tissue information, while retaining the advantages of convex optimization for global signal fitting and biologically interpretable streamline weighting.

2.4.2 Limitations of microstructure informed tractography

While microstructure informed tractography methods provide powerful tools for obtaining more biologically meaningful estimates of structural connectivity, several *methodological limitations* must be acknowledged (Daducci et al., 2016; Daducci and Schiavi, 2025).

A fundamental challenge lies in the quality and completeness of the *input tractogram*. Since microstructure informed methods cannot generate missing fibers, any absent or underrepresented pathway in the input may lead to the misattribution of signal, potentially assigning contributions to spurious connections or underestimating specific tracts (Daducci et al., 2016). Ensuring high sensitivity in the initial tractogram is therefore critical, even at the cost of including false positives (Zalesky et al., 2016).

Anatomical accuracy remains a significant concern. Even state-of-the-art tractography algorithms, including those informed by microstructural priors, face an intrinsic trade-off between sensitivity and specificity. As explained in Section 2.3.2.5, these methods often introduce numerous false positives, particularly in regions where distinct bundles intersect, creating "bottlenecks" that cannot be fully resolved by local information alone (Girard et al., 2020; Maffei et al., 2022; Maier-Hein et al., 2017; Schilling et al., 2019b; Thomas et al., 2014). COMMIT extensions reduce but do not eliminate such errors (Schiavi et al., 2020). Inaccuracies in trajectory or spatial extent can distort both local and global measures of connectivity, especially in geometrically complex regions such as crossing or fanning fibers. Moreover, excessive or redundant streamlines can lead to ill-posed estimation problems in global fitting frameworks, amplifying instability and inducing potential biases in the quantitative estimations (Daducci et al., 2016; Daducci and

Schiavi, 2025; Daducci et al., 2025).

In addition, microstructure informed tractography is intrinsically constrained by the assumptions made in the *forward model* that links streamlines to the diffusion signal (Daducci et al., 2016). Most formulations assume that each reconstructed streamline represents a physically continuous fiber population extending along its entire length. However, tractograms often contain *partial fibers*, truncated pathways, or streamlines that only cover a subset of the true anatomical trajectory. These incomplete representations may still contribute to the signal in a voxel-wise manner, but their limited spatial support can introduce inconsistencies in the global fitting process. As a result, the optimization may attribute signal to anatomically implausible or fragmented pathways, leading to biased weight estimates and reduced biological interpretability. This effect is particularly problematic in regions characterized by complex branching patterns or where streamlines prematurely terminate due to local modeling errors or stopping criteria (Daducci et al., 2016).

Another key limitation is the common assumption of *constant microstructural properties* along individual streamlines (Daducci et al., 2016). Parameters such as intra-axonal signal fraction, relaxation times, or myelin content are often treated as uniform along the trajectory of a given fiber, despite evidence of spatial heterogeneity in both healthy and pathological tissue (Jones, 2010a; Jones et al., 2013; Smith et al., 2022; Zalesky et al., 2020). Localized lesions or demyelinating processes can violate this assumption, introducing biases in the estimated contributions and potentially propagating errors across the connectome due to the global nature of the fitting algorithms (Dell'Acqua et al., 2025; Yeh et al., 2021; Zhang et al., 2022). Indeed, even a mismatch confined to a single region can trigger compensatory adjustments elsewhere in the tractogram, indirectly altering the estimated weights of connections that are anatomically unaffected. This phenomenon, often described as a “butterfly effect”, implies that errors are not spatially contained but can cascade globally, biasing the entire WM wiring (Daducci and Schiavi, 2025) (Figure 2.43).

Furthermore, the diffusion-weighted signal itself is affected by *spatial inhomogeneities* that are not directly related to the underlying WM microstruc-

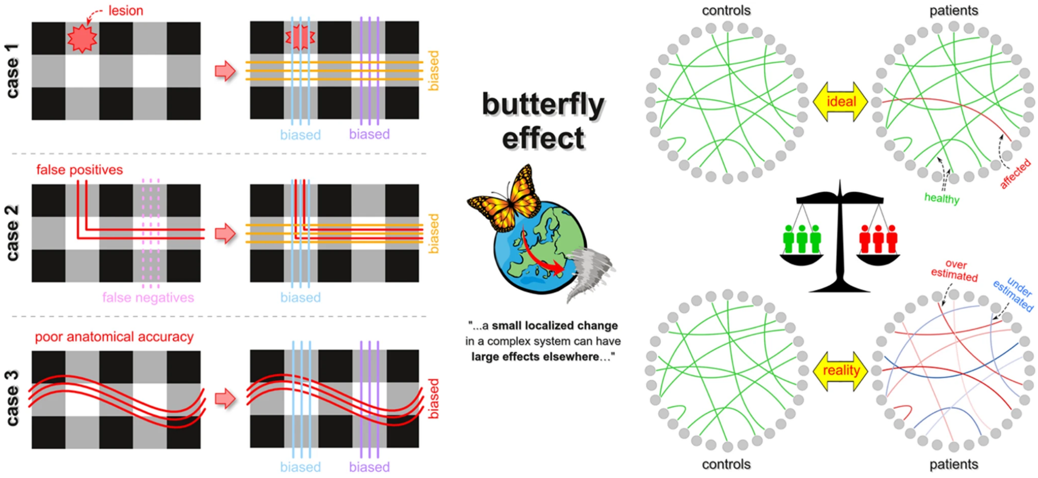

Figure 2.43: Conceptual representation of the "butterfly effect" in microstructure-informed tractography. Local perturbations, such as focal lesions, missing or spurious bundles, or inaccurate streamline geometry, can propagate through the global optimization, leading to a misestimation of microstructural properties across the entire connectome and biased connectivity measures. From (Daducci et al., 2025).

ture (Belaroussi et al., 2006). Variations in coil sensitivity, susceptibility-induced distortions, partial volume effects, and residual motion artifacts can generate spatially structured intensity fluctuations that violate the assumptions of uniform tissue properties. Since microstructure informed tractography minimizes a global fitting error, such inhomogeneities may be erroneously interpreted as microstructural variations, altering the estimated contribution of nearby streamlines (Daducci et al., 2016). In addition, the length of individual fibers can introduce systematic bias: longer streamlines traverse more voxels and may therefore be over-penalized in regularized frameworks, or conversely favored if regularization is insufficient (Daducci et al., 2016).

Finally, despite substantial progress in optimization strategies and sparse solvers, the *computational demands* of microstructure informed tractography remain considerable. Global fitting approaches, especially when applied to high-resolution multimodal datasets or very large tractograms, continue to require substantial memory and processing resources (Daducci et al., 2015;

Schiavi et al., 2020). Careful planning is therefore required to balance tractogram density, spatial resolution, and computational feasibility.

In summary, while microstructure informed tractography provides a powerful framework for deriving biologically meaningful and quantitatively interpretable reconstructions of brain connectivity, its reliability is constrained by the quality of the input tractogram, persistent anatomical ambiguities, assumptions of microstructural uniformity along fibers, the potential for globally propagating estimation errors, and computational burden. Awareness of these limitations is essential for responsible interpretation of results and for future methodological advancements.

Chapter 3

Blurred streamlines representation

3.1 Motivation

As detailed in Section 2.3.2.5, despite the unique potential, tractography suffers of some known limitation that lead to biases in the reconstructed tractograms (Girard et al., 2014; Rheault et al., 2020; Zhang et al., 2022). In particular, a fundamental decision that any user, from beginners to experts, always has to face is *how many streamlines to generate* for a given data set. Figure 3.1 illustrates the issue: if one reconstructs a small number of streamlines, there will be a high risk of missing some anatomical connections, i.e. False Negative (FN), whereas by generating a larger number there will be increasing chances to obtain spurious trajectories that do not reflect the underlying fiber structure, i.e. False Positive (FP)s, as well as to introduce unnecessary redundancy. Even though it might appear a minor detail at first glance, this is actually a very important choice that can have serious consequences on the accuracy and the interpretation of the results (Rheault et al., 2020). Yet, this issue has not received proper consideration in the past and it has been addressed either marginally or using empirical approaches; thus, to date, it *remains an open question* in the community.

Some studies investigated this problem from a saturation point of view: tractography is seen as a sampling process which retrieves a subset of streamlines in a bundle, and the consequences of increasing their number are studied

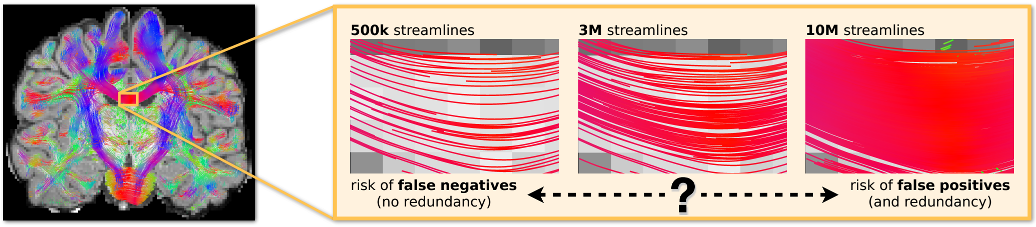

Figure 3.1: *How many streamlines should be generated?* If one reconstructs a tractogram with a low number of streamlines, no redundancy is expected in the tractogram but there will be a high risk of missing parts of brain's anatomy, i.e. false-negative connections. Conversely, as the number of streamlines increases, this possibility is more and more unlikely but there will be increasing chances of introducing redundancy in the tractogram as well as reconstructing false-positive connections. How to choose the optimal number of streamlines is still an open question in the community.

by looking at the volume (Gauvin, 2016) or the information content (Moyer et al., 2019) of the bundle. Reid et al. (2020) adopted a more practical perspective: they designed two methods for predicting the number of streamlines that should be generated to obtain a reliable tractogram, considering the reproducibility of microstructural metrics and thresholded track-density images. They discovered that many factors strongly influence the required streamline count, like the acquisition protocol, the processing steps and the anatomical tract considered. Other studies analyzed the impact of the number of streamlines on the connectome, showing that reconstructing more streamlines improves the reproducibility of network metrics extracted from the resulting connectomes (Roine et al., 2019) but also leads to more false-positive connections (Sinke et al., 2018). Therefore, the anatomical reliability of tractography is weakened by this lack of specificity, which is crucial to study brain connectivity (Drakesmith et al., 2015; Zalesky et al., 2016).

To tackle the dilemma on the optimal cardinality of the tractograms, it has become *common practice* to generate several millions of streamlines and rely on microstructure informed tractography algorithms to eliminate the many false positives that are inevitably reconstructed (Daducci et al., 2016; Maier-Hein et al., 2017). However, *redundancy among streamlines induces subtle side effects* in methods based on linear formulations, like the SIFT, LiFE, and COMMIT (Daducci et al., 2015; Pestilli et al., 2014; Smith et al., 2013), which have been largely overlooked until now (as mentioned in Section 2.4.2). In fact, besides specific differences in implementation and modeling choices, all these methods attempt to solve a linear system like that in Eq. 2.29, where the *potential* signal contributions of the streamlines to each voxel are encoded as separate columns of the linear operator $\mathbf{A}$ (Figure 3.2, top). It is important to notice that when two (or more) streamlines follow similar trajectories, besides being clearly redundant to explain the signal in the voxels they traverse, the corresponding columns tend to become linearly dependent (Figure 3.2, bottom). This phenomenon, occurring especially when a high number of streamlines is generated, is called *collinearity* (Belsley et al., 1980) and makes it difficult to interpret the coefficients estimated with a given model, i.e., actual streamline contributions in this context.

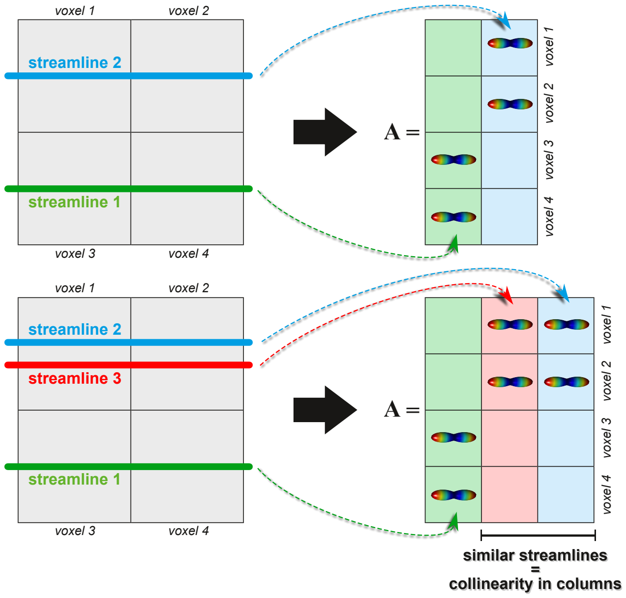

Figure 3.2: *The problem in linear formulations for microstructure informed tractography.* When streamlines follow similar trajectories, the corresponding columns of the linear operator, i.e. $\mathbf{A}$, tend to become linearly dependent, posing serious problems for the interpretation of the estimated coefficients.

We propose a novel streamline representation, called "*blurred streamlines*", specifically designed to prevent the onset of collinearity. Our solution explicitly models redundant streamlines in a tractogram using a combination of clustering of the trajectories and spatial blur of the corresponding signal contributions. We evaluated its effectiveness both on synthetic and real data, and our results demonstrate that by using this approach we can reduce the redundancy among streamlines while simultaneously improve the anatomical accuracy of the tractograms.

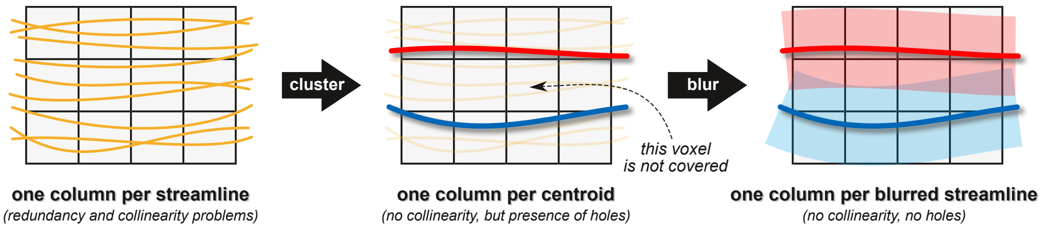

Figure 3.3: *The proposed approach.* Given a tractogram (left), we first *cluster* its streamlines (middle) to remove the redundancy between them and to mitigate possible collinearity problems. Then, we *blur* spatially the dMRI signal contributions of the resulting centroids (right) to guarantee coverage of all imaging voxels.

3.2 Materials and methods

The proposed solution is illustrated in Figure 3.3 and consists of two steps. First, we *perform clustering on the input tractogram* to eliminate redundancy between the streamlines (yellow lines in left panel) and to avoid the presence of collinearity in the corresponding linear operator $\mathbf{A}$. The resulting centroids (red and blue lines in middle panel) are streamlines representative of the estimated clusters and, by construction, are sufficiently dissimilar and likely generate linearly independent columns in $\mathbf{A}$ (one per centroid). However, they may not cover properly all voxels as the original tractogram (arrow in middle panel). Consequently, if we used directly the simplified tractogram consisting only of these centroid streamlines, we might not have an optimal support set to solve the linear system. To mitigate this problem and guarantee proper coverage of all voxels, we also introduce a method to *blur the dMRI signal contributions* of each centroid (transparent red and blue areas in right panel), as described in Section 3.2.2. The extent of this blur has no anatomical interpretation, as the proposed representation aims to remove duplicated streamlines at a purely geometrical level, thereby avoiding collinearity issues in the mathematical formulations employed in subsequent processing steps.

Without loss of generality, among all the methods based on linear formulation, we decided to implement the blurred streamlines in the case of COMMIT mainly because its formulation is very flexible and general. However, we believe that other tractography techniques may take advantage of our novel streamline representation, too. To ease the readability, in the remainder of this paper, we will refer to this implementation as $\text{COMMIT}_{\text{blur}}$.

3.2.1 Redundancy reduction

As already mentioned, collinearity in the linear system (2.29) is caused by redundant streamlines in the input tractogram, since the similarity between their trajectories introduces linearly-dependent columns in the linear operator $\mathbf{A}$. It follows that, to effectively reduce collinearity in $\mathbf{A}$, one can perform clustering on the tractogram and remove similar/redundant streamlines. To this end, in this work we adopted the QuickBundlesX algorithm (Garyfallidis et al., 2012, 2016) and used the Average of Pointwise Euclidean Metric as distance with a small threshold t_r (more details aboute the optimal value can be found later). To accelerate this step, we first split the input tractogram in groups, where each group contains only the streamlines that connect a specific pair of GM regions. Then, we performed clustering in each bundle separately, as this operation effectively reduces the search space, i.e. redundant/similar streamlines clearly belong to the same bundle, and, also, can be done in parallel. The *resulting tractogram* consists only of the K centroid streamlines C_k of the corresponding clusters, i.e. $\{C_k \,|\, k = 1, \dots, K\}$, while all other streamlines are discarded. It is important to highlight that the goal here is not to segment anatomical structures, but rather to (i) identify similar streamlines, (ii) keep only one that is representative of each cluster and (iii) discard redundant ones. We designated as representative of each cluster the streamline that is closer to the corresponding centroid.

To obtain more accurate and robust clustering results, we *pre-filtered the tractogram* to remove the streamlines deemed as outliers, because they could negatively affect the clustering itself. We considered two types of outliers: streamlines that are not compatible with the acquired signal and those with geometrically implausible trajectories. For the former kind, we run plain COMMIT (i.e. no blurred streamlines) with the aim of removing streamlines with an estimated contribution equal to zero, meaning that they do not contribute to the measured dMRI signal. Even though we know that the results of this step might be sub-optimal due to collinearity, we experimentally observed that it is usually able of removing some spurious trajectories; in the worst case, this step has no effect. Then, to discard geometrical outliers, we run QuickBundlesX as described above but with an higher threshold t_o, i.e. $t_o > t_r$, and removed from the tractogram the streamlines belonging to clusters populated by very few streamlines (three or less), which are considered the results of noise during the reconstruction process.

3.2.2 Spatial blur

In COMMIT, as well as all other methods for microstructure informed tractography, the linear operator $\mathbf{A}$ is constructed assuming that every streamline contributes to the signal only in those voxels it passes through (Figure 3.4A, top). With the term *blurred streamlines* we mean that a streamline can instead contribute also to adjacent voxels (Figure 3.4A, bottom) such that it captures the redundancy between similar fiber trajectories using a compact representation. The procedure to achieve this is illustrated in Figure 3.4 and explained more in details in what follows.

3.2.2.1 Sampling the space around a streamline

For each centroid streamline C_k we create a set of M replicas $\{C_k^1, \dots, C_k^M\}$ such that they form a tubular structure of radius r following the trajectory

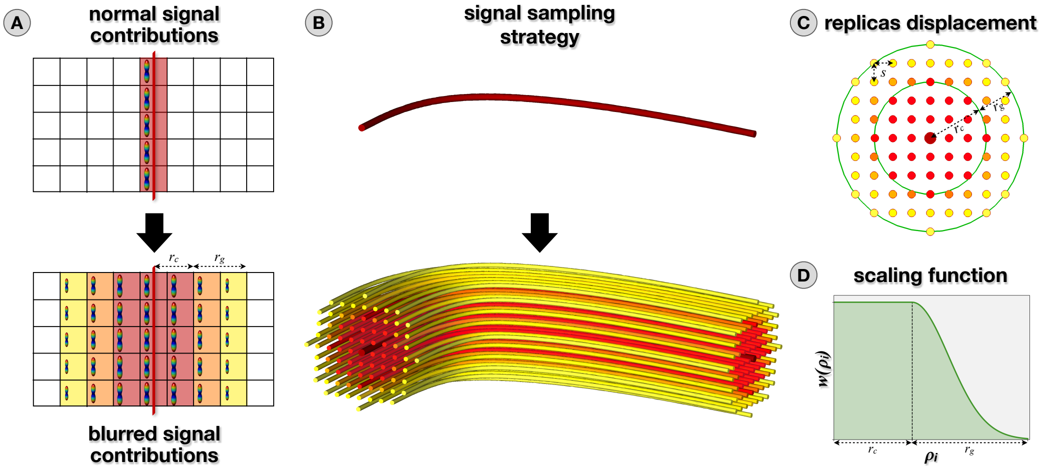

Figure 3.4: *Blurred streamlines.* A streamline contributes to the signal only in those voxels it passes through, whereas a blurred streamline can contribute also to adjacent voxels (panel A). The spatial blur implementation is done empirically: we create many replicas of the centroid streamline (panel B) by displacing them in a Cartesian grid (panel C) and scaling their contributions as function of the distance from the actual centroid (panel D). The symbols meaning is detailed in section 3.2.2.

of C_k, as illustrated in Figure 3.4B. Each copy C_k^i is obtained by shifting all points of C_k by a given offset (ρ_i, θ_i), expressed in polar coordinates, in a plane that is always orthogonal to the direction of C_k. After moving the first point of C_k to position (ρ_i, θ_i) in the orthogonal plane, we construct all remaining points of C_k^i by following the local tangent of C_k along its trajectory. To guarantee uniform sampling of the space around a centroid, the displacements (ρ_i, θ_i) of the M replicas are organized in a Cartesian grid of spacing s centered in C_k (Figure 3.4C). The number M of replicas depends both on the radius r and the grid spacing s, but it is the same for all centroids.

3.2.2.2 Aggregating signal contributions

The total signal contributions associated to a centroid C_k, which form the k^{th} column of $\mathbf{A}$, i.e. $\mathbf{A_k}$, are obtained as a weighted combination of all the individual contributions of its replicas, as follows:

$$S(C_k) \equiv \mathbf{A_k} = \sum_{i=1}^{M} w(\rho_i)\, S(C_k^i) \;, \tag{3.1}$$

where $S(C_k^i)$ are the signal contributions of the replica C_k^i, i.e. the one that was shifted to position (ρ_i, θ_i), and are computed as usual considering only the traversed voxels. However, to ensure that replicas that are closer to the centroid are being considered more than those far away, we additionally modulate these contributions as function of their distance from C_k; in this work, the *scaling factor* $w(\rho_i)$ is defined as:

$$w(\rho_i) = \begin{cases} 1 & \text{if } \rho_i \leq r_c, \\ \exp\left(\frac{-0.5\,(\rho_i - r_c)^2}{\sigma^2}\right) & \text{otherwise .} \end{cases} \tag{3.2}$$

As illustrated in Figure 3.4D, there is a core area of extent r_c inside which the replicas have the same contribution as the original streamline C, followed by a blur area of extent r_g, such that $r_c + r_g = r$, where the contributions are scaled by a Gaussian with standard deviation σ.

3.2.3 Data description and processing

We *quantitatively* evaluated the proposed approach using the synthetic phantom developed for the “2013 HARDI reconstruction challenge” at the International Symposium on Biomedical Imaging (ISBI) (Caruyer et al., 2014). This is shown in Figure 3.5A and it consists of 27 Ground Truth (GT) fiber bundles between 53 GM regions that resemble real brain configurations with complex arrangements, like crossing, branching and kissing with different sizes and curvatures. The corresponding dMRI signal was generated along 64 directions with $b = 3000\,\mathrm{s/mm^2}$ and Rician noise was added with a SNR of 30. We also *qualitatively* evaluated it on in vivo data using 10 healthy subjects (details reported in Table 3.1) from the Human Connectome Project (HCP) test-retest data set (Van Essen et al., 2013b). We downloaded the preprocessed diffusion data and the structural T_1-weighted images with the corresponding standard Desikan-Killiany (Desikan et al., 2006) parcellation in 85 regions performed with FreeSurfer (Fischl et al., 2002), in which we replaced the brainstem with only the medulla (Iglesias et al., 2015).

Subject ID	Gender	Age
103818	F	31-35
105923	F	31-35
111312	F	31-35
114823	F	31-35
115320	F	31-35
122317	M	31-35
139839	M	26-30
146129	M	22-25
149337	M	31-35
149741	M	26-30

Table 3.1: *Demographic data* of each subject that was considered in the qualitative in vivo evaluation.

For both types of data we computed the FODs in each voxel using CSD (Tournier et al., 2007), with the multi-shell multi-tissue algorithm (Jeurissen et al., 2014) only in the case of HCP images. Tractography was performed with three different algorithms and using default parameters if not otherwise specified: a deterministic, i.e., SD_STREAM (Tournier et al., 2012), and two probabilistic, i.e., iFOD2 (Tournier et al., 2010) and Trekker (Aydogan and Shi, 2021). Each of the three tractograms for the phantom was generated with 1 million of streamlines by seeding in the whole WM mask. For the in vivo data we used iFOD2 and SD_STREAM in combination with ACT (Smith et al., 2012) to reconstruct 3 millions of streamlines of length between 5 mm and 250 mm (setting the cutoff = 0.06 for iFOD2 and the angle = 70° and step size = 0.25 mm for SD_STREAM). Instead, for Trekker we seeded in the WM and generated 1 million of streamlines using default parameters.

For the evaluation with COMMIT (with and without blurred streamlines) we used as forward model the GT intra-axonal signal fraction map of the phantom in the case of synthetic data. Instead, for the in vivo data, since the

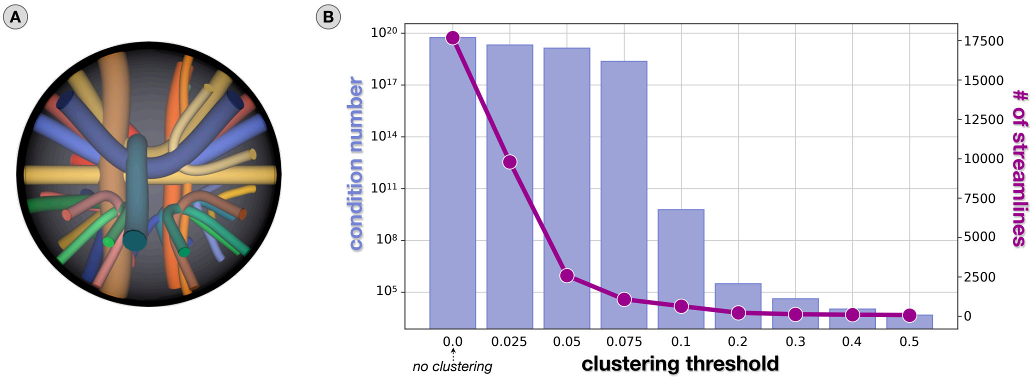

Figure 3.5: *Efficacy in reducing the redundancy.* (A) Synthetic phantom used to quantitatively evaluate the proposed streamline representation. (B) The "lineplot" reports the number of streamlines of a representative bundle reconstructed using deterministic tractography and clustered at various thresholds (t_r), whereas the "barplot" shows the condition number of the resulting linear operator.

GT is not available, we used the intra-neurite volume fraction map obtained with multi-compartment SMT (Kaden et al., 2016) (see Section 2.3.1.3); more details can be found in (Schiavi et al., 2020). Before the fit, we assigned each endpoint of a streamline to a node if that point fell within 2 mm from one of the GM regions; then, a streamline was considered as connecting two nodes if both endpoints were assigned, otherwise it was discarded and excluded from the analysis. The quantitative connectomes were computed by using as edge weights the sum of the estimated streamline contributions connecting the pairs of regions.

3.2.4 Experiments

3.2.4.1 Efficacy in reducing the redundancy

To quantify the redundancy present in the original tractogram and how much this can be reduced by the proposed streamline representation, we computed the condition number of the corresponding linear operators, i.e. **A** in Eq. (2.29). The *condition number* of a matrix measures the sensitivity of

the parameter estimates to small changes in the matrix itself and can be used to identify collinearity between its columns (Belsley et al., 1980; Strang, 1980); hence, in this context, redundancy among streamlines. However, due to the huge size of **A** for typical tractograms, on the order of 10^{11} elements for 1 million streamlines, it is computationally unfeasible to store in memory the whole matrix and calculate its condition number; we thus approximated its value by computing it from a representative bundle, as redundancy/collinearity arises only from similar streamlines which indeed belong to the same bundle. This computation was performed both on the original set of streamlines and after clustering it using various thresholds; in the case of SD_STREAM, we used $t_r \in \{0.025, 0.05, 0.075, 0.1, 0.2, 0.3, 0.4, 0.5\}$ mm, while for iFOD2 and Trekker we applied larger thresholds
$t_r \in \{0.2, 0.4, 0.6, 0.8, 1.0, 1.25\}$ mm as, in general, the streamlines reconstructed with these algorithms are less similar among them.

3.2.4.2 Accuracy of the estimates

We investigated the accuracy of the estimates with $\text{COMMIT}_{\text{blur}}$, for all three tracking algorithms, as function of the blur parameters by varying both in the range $r_c, r_g \in \{0, 0.1, \dots, 1.0\}$ mm. We quantitatively compared the estimates with and without blurred streamlines by means of: number of True Positive (TP) and FP connections, as well as the L1 distance between the estimated and the GT connectome, defined as:

$$L1(\tilde{C}, C) = \sum_{i,j=1}^{N} |\tilde{C}_{i,j} - C_{i,j}| \tag{3.3}$$

where $\tilde{C}$ and C are the estimated and GT connectome, respectively, $\tilde{C}_{i,j}$ and $C_{i,j}$ indicate the corresponding edges, and N is the number of nodes in the connectome. Moreover, to evaluate how well a given configuration is consistent with the underlying data, we also report the Root Mean Squared Error (RMSE) of the fit between the estimated $\tilde{S}$ and the GT signal S, computed for all the WM voxels (V) as following:

$$RMSE(\tilde{S}, S) = \sqrt{\frac{\sum_{i=1}^{V} (\tilde{S}_i - S_i)^2}{V}} \tag{3.4}$$

3.2.4.3 Robustness to noise

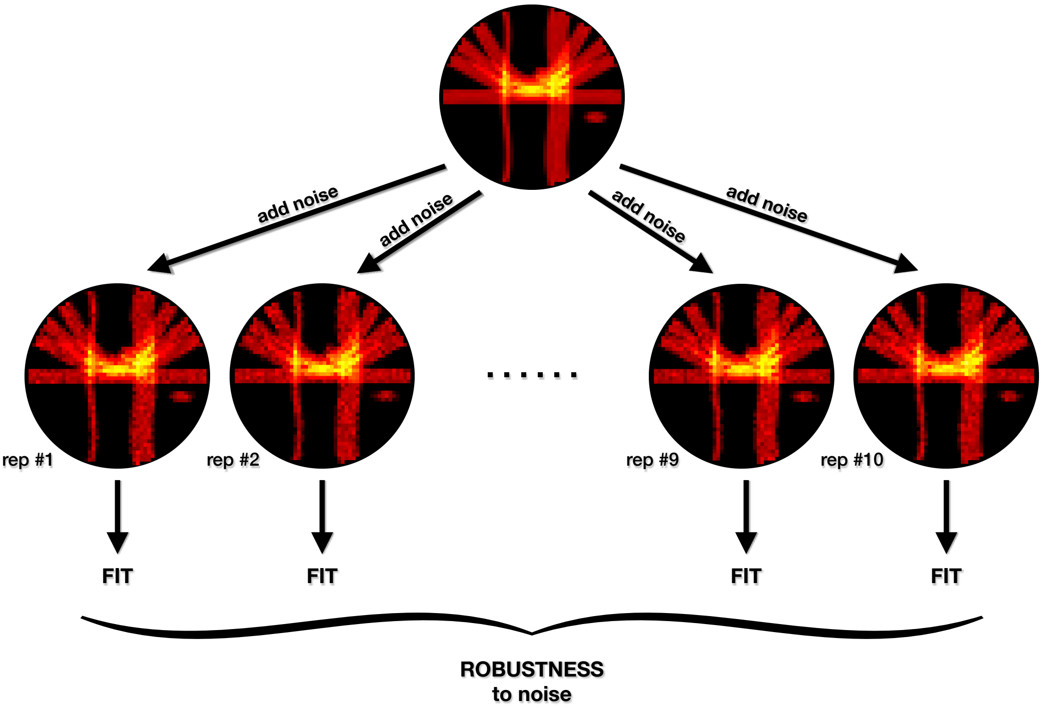

Figure 3.6: *Robustness to noise.* To investigate the benefits of the redundancy reduction, we added Gaussian noise (SNR=30) to the GT intra-axonal signal fraction map and used this noisy map to perform the fit both without and with the blurred streamlines representation. We repeated it for 10 iterations and we quantified the robustness to the introduced perturbations by computing both the distances from the reference estimates and the coefficient of variation.

To highlight the advantages of using the proposed representation, we analyzed the effects of small perturbations in the data on the parameter estimates. As illustrated in Figure 3.6, we added Gaussian noise with SNR=30 to the input image and, then, this noisy map was used to perform the fitting with and without the blurred streamlines representation. This test was repeated for 10 different applications of Gaussian noise and it was performed for a single clustering threshold ($t_r = 0.6\,\text{mm}$ for iFOD2 and Trekker and $t_r = 0.2\,\text{mm}$ for SD_STREAM, with $t_o = 2t_r$), maintaining fixed the blur parameters ($r_c = 0.5\,\text{mm}$ for iFOD2, $r_c = 0.6\,\text{mm}$ for Trekker, $r_c = 0.2\,\text{mm}$ for

SD_STREAM and $r_g = 0.9\,\text{mm}$ for all three algorithms). For each of the ten iterations, we computed the normalized L1 distance between the streamline weights estimated using the noisy map and the streamline contributions estimated using the original map, which we consider as reference. We used the same metric also for the connectomes but without normalizing, because the distances were measured from the GT connectome. Moreover, to have a precision measure of the proposed method, we computed the Coefficient of Variation (CV) of the streamlines contributions and the connections strength resulting from the fitting with the ten noisy maps.

3.2.4.4 Qualitative evaluation on in vivo data

We also evaluated the effectiveness of the blurred streamlines on real data and performed a qualitative comparison between the reconstructions obtained by fitting COMMIT using its original formulation and with the proposed representation, setting $t_r = 2.0\,\text{mm}$, $r_c = t_r$ and $r_g = 0.9\,\text{mm}$. First, we visually compared the overall intra-cellular compartment signal estimated from the tractograms reconstructed with the three algorithms to the GT map that was used for the fitting. Then, for each subject we virtually dissected two well-known bundles, i.e., Corpus Callosum and Pyramidal Tract, using the protocol defined by Rheault et al. (2022), and visually inspected the signal contributions corresponding only to the streamlines belonging to those connections to obtain better insight on the quality of the reconstructions.

3.3 Results and discussion

3.3.1 Reducing the redundancy of a tractogram

Firstly, to assess the decrease of redundancy in a tractogram achieved using the proposed representation, we computed the condition number of the corresponding linear operator $\mathbf{A}$ in Eq. (2.29). Figure 3.5 reports the number of streamlines of a representative bundle from a tractogram obtained with deterministic tractography (i.e., SD_STREAM) as function of the clustering threshold t_r, together with the condition number of the corresponding linear operator that arises when feeding such clustered tractogram to COMMIT; results at $t_r = 0.0$ correspond to the original tractogram without any clustering.

As we can see from the plots, the condition number corresponding to the original tractogram is indeed very large, $\approx 5.5 \times 10^{19}$, and clearly reveals the very high redundancy that is present in tractography reconstructions. As the clustering level increases, the tractogram size quickly diminishes (lineplot), due to the substitution of sets of similar streamlines with single centroids, but the condition number decreases at a slower rate (barplot). However, increasing further the clustering level it is possible to drastically reduce the condition number, e.g. ≈ 15 orders of magnitude at $t_r = 0.2\,\text{mm}$, clearly demonstrating that the removal of streamlines having similar trajectories can effectively reduce collinearity in the corresponding linear operator. Similar results were obtained in case of iFOD2 and Trekker (Figure 3.7; see Section 3.3.5 for more details on the clustering effects in case of iFOD2).

3.3.2 Accuracy evaluation

Knowing that by applying clustering we can dramatically diminish the redundancy, we have to prove that the introduced spatial blur provides results that are as accurate as the ones resulting using the standard representation. After determining a threshold that is able to reduce the collinearity, we tested various values for the two main parameters defining the blur: the core extent (r_c) and the Gauss extent (r_g).

Figure 3.8 summarizes the evaluation of the accuracy of the estimates with $\text{COMMIT}_{\text{blur}}$ in the case of an input tractogram generared with deterministic tractography (SD_STREAM). Results correspond to a given clustering configuration, i.e. $t_r = 0.2\,\text{mm}$ and $t_o = 2t_r$, which proved quite effective in reducing the condition number (see Figure 3.5). Using $\text{COMMIT}_{\text{blur}}$ with $r_c = 0.2\,\text{mm}$ and $r_g = 0.9\,\text{mm}$ (highlighted by the green square in the heatmaps reported in Figure 3.8) the resulting reconstruction contains all the 27 TP and only 65 FP connections (27 TP and 178 FP for standard COMMIT) and its distance

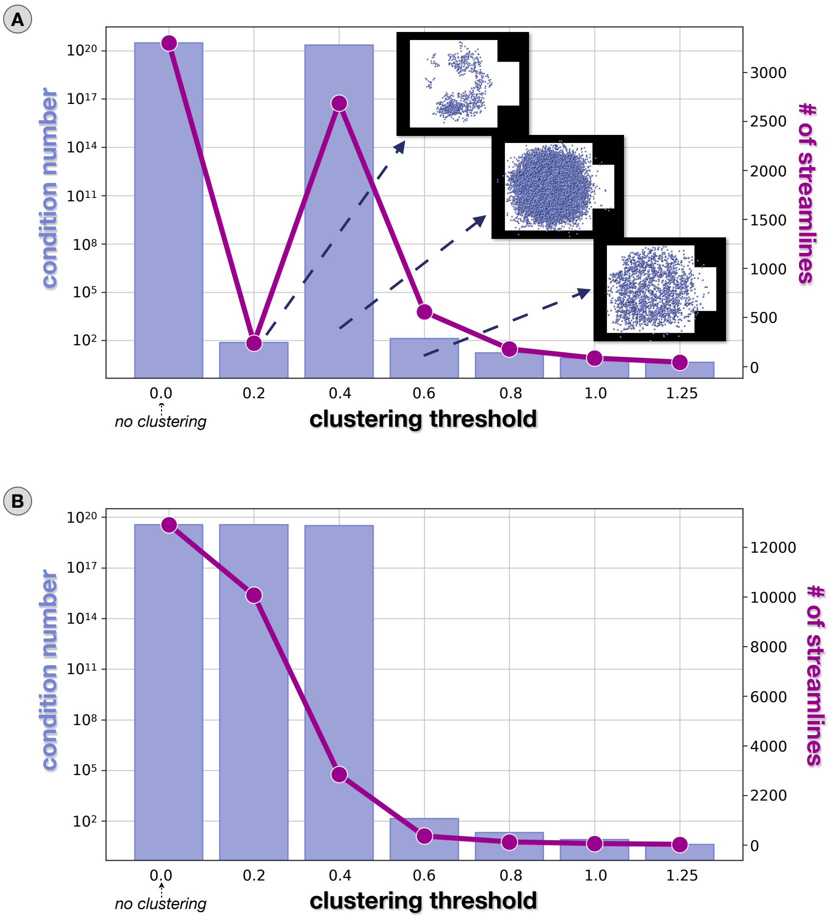

Figure 3.7: *Efficacy in reducing the redundancy in case of iFOD2 (A) and Trekker (B).* For a range of clustering thresholds we show the condition number (barplot) and the number of streamlines (lineplot) of a connection reconstructed on the phantom. In A, to explain better the effect of the clustering, we report a section of the bundle and the displacement of the streamlines kept using some of the thresholds.

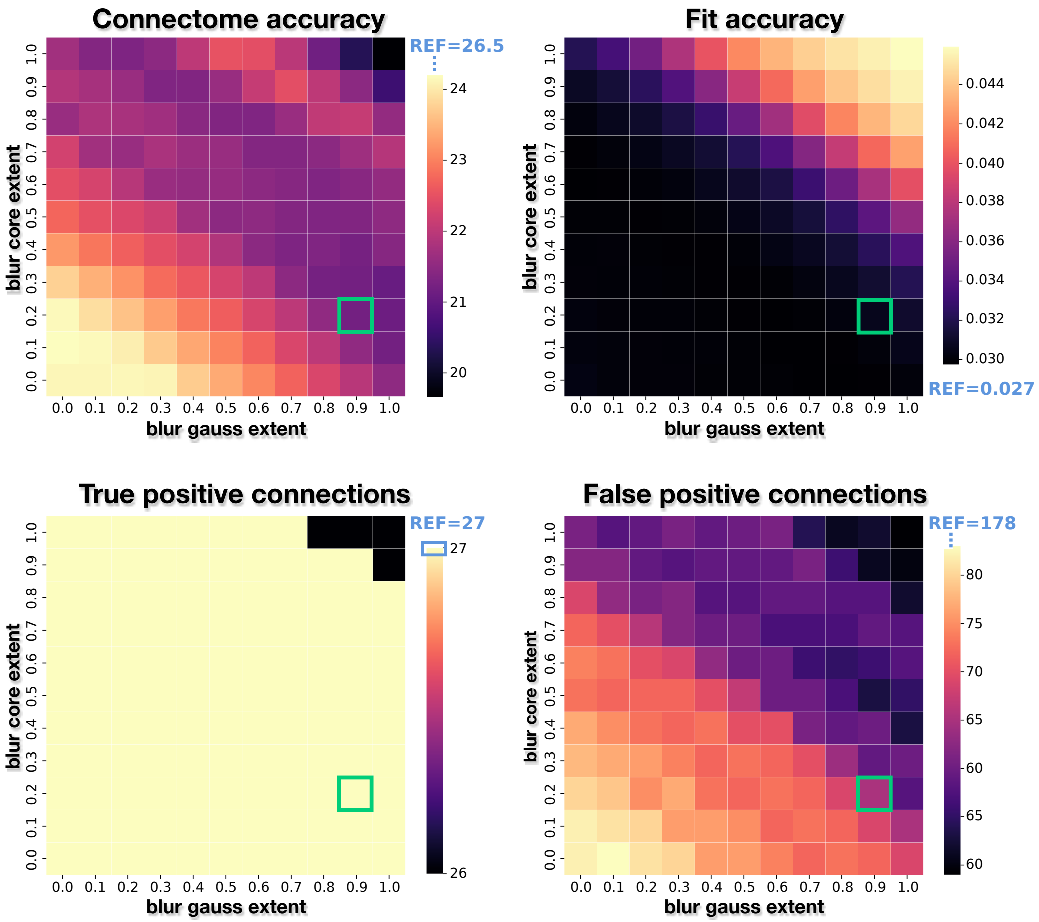

Figure 3.8: *Accuracy of the estimates as function of the blur parameters.* The estimates obtained with COMMIT$_{\text{blur}}$ on an input tractogram reconstructed with deterministic tractography (SD_STREAM) and clustered with a threshold $t_r = 0.2\,\text{mm}$ are reported for various configurations of core extent and Gauss extent. The assessment is performed in terms of: error in the estimation of the connectome (top left), fitting error (top right), number of true-positive (bottom left) and false-positive connections (bottom right). Results are compared to those obtained with the standard formulation of COMMIT, i.e. using the classical streamline representation, which are reported as "REF" values. The green square indicates the configuration discussed in the results.

from the GT is smaller than the one of COMMIT: L1 = 21.20 (for COMMIT: L1 = 26.50). Moreover, the RMSE inside the WM is equal to 3.1×10^{-2} (RMSE = 2.7×10^{-2} for COMMIT) and it is important to point out that these results are obtained using only 0.97% of the original streamlines (5,812 versus the 600,371 used by COMMIT). Similar results were obtained in case of iFOD2 and Trekker (Figures 3.9a and 3.9b).

As can be seen in the top right plot of Figures 3.8, 3.9a and 3.9b, the fitting error of the proposed approach is slightly greater than the one obtained using the standard formulation ("REF" value). This increase is probably due to the fact that the new representation prevents overfitting to take place. Indeed, we introduce additional spatial constraints to the streamlines while the original COMMIT framework has more freedom in adapting the streamline weights to reflect the underlying structure with less errors by also fitting the noise in the data.

Despite this, we proved that the proposed approach is as accurate as the state-of-the-art method. Indeed, by choosing the optimal combination of blur parameters, the resulting reconstruction contains all the real connections and less false positives with respect to COMMIT, independently of the tractography algorithm adopted. Moreover, when computing the L1 distance from the GT connectivity matrices, the connectomes estimated by $\text{COMMIT}_{\text{blur}}$ are more accurate than the ones resulting from COMMIT. Finally, it is important to remember that thanks to the proposed representation these results are obtained using always less than 5% of the input streamlines, in particular $\approx$ 1% for SD_STREAM, $\approx$ 4% for iFOD2 and $\approx$ 2% for Trekker.

3.3.3 Robustness to perturbations in the input

Once we determined the optimal parameters, both for the clustering and the blur, we performed an additional test to quantify the practical benefits of the reduced redundancy in the tractograms, besides the clear reduction in storage requirements. Since the condition number indicates the degree by which the estimates are sensitive to errors in the input, the decrease of several orders of magnitude means that with the proposed representation we should obtain

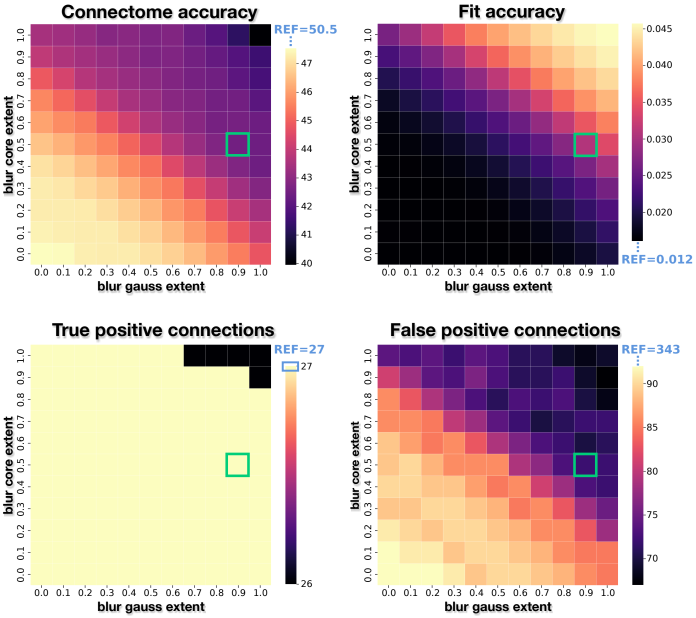

(a) Results using probabilistic tractography as input (iFOD2).

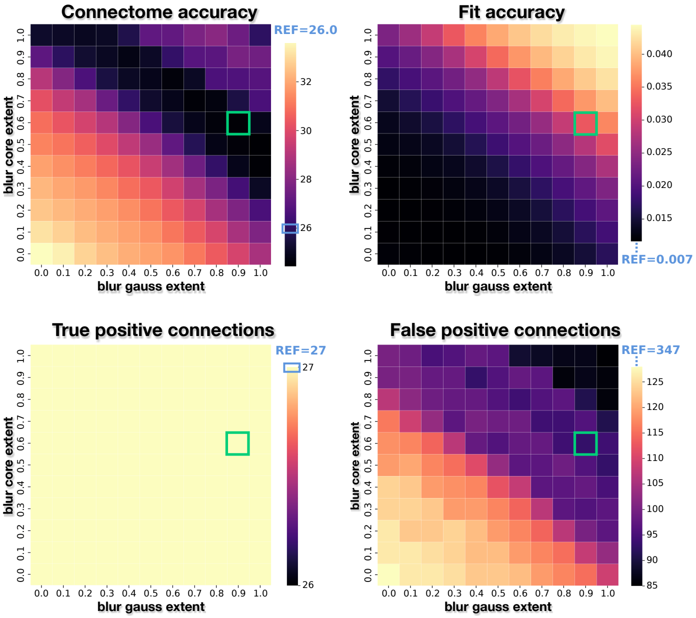

(b) Results using particle-filtering tractography as input (Trekker).

Figure 3.9: Results of the *accuracy* of COMMIT$_{\text{blur}}$ estimates as function of the blur parameters, when using iFOD2 (a) and Trekker (b) tractograms clustered with a threshold $t_r = 0.6\,\text{mm}$. Results are compared to the those of the standard formulation of COMMIT (reported as “REF” values).

more robust estimates than the ones obtained using the standard formulation. So, we introduced Gaussian noise in the input map that was used for the fit and then we evaluated the robustness to such perturbations of COMMIT using both streamline representations.

		streamline weights		connectomes	
		original	blur	original	blur
iFOD2	mean dist.	1.20	**0.72**	55.36	**43.05**
	mean CV	2.40	**1.93**	0.69	**0.46**
SD_STREAM	mean dist.	0.94	**0.51**	27.74	**21.95**
	mean CV	1.95	**1.55**	0.70	**0.54**
Trekker	mean dist.	1.59	**0.63**	33.90	**27.51**
	mean CV	2.53	**1.78**	0.98	**0.64**

Table 3.2: *Precision of blurred streamlines estimates.* For all the three tractography algorithms used we report the mean L1 distances (dist.) and coefficient of variations (CV) computed both for the streamlines weights and the connectomes estimated by COMMIT (“original”) and COMMIT$_{\text{blur}}$ (“blur”).

Table 3.2 summarizes the results: for all the three tractography algorithms, we report the mean of the L1 distances and of the CVs computed over the ten iterations. We considered both the streamlines weights and the connectomes estimated without and with the employment of the blur streamlines representation. As can be seen, using COMMIT$_{\text{blur}}$ we can obtain estimates that are on average closer to the reference ones than the ones of COMMIT, both at the level of estimated streamline weights (e.g., for SD_STREAM: L1 distance = 0.94 and = 0.51 for COMMIT and COMMIT$_{\text{blur}}$, respectively) and at higher resolution considering the connectomes (e.g., for SD_STREAM: L1 distance = 27.74 and = 21.95 for COMMIT and COMMIT$_{\text{blur}}$, respectively). Moreover, COMMIT enhanced by the proposed representation is on average more precise than the original formulation: for example, using SD_STREAM, the mean CV of streamline weights equals 1.95 for COMMIT and 1.55 for COMMIT$_{\text{blur}}$, while the mean CV of the connectomes is 0.70 and 0.54, respectively. This means that using the blurred streamlines representation we obtain results that are more robust to perturbations, like errors or noise, in the input data.

It is worth noting that the mean distances reported in Table 3.2 for the streamline weights are normalized because, by construction, the contributions estimated using COMMIT$_{\text{blur}}$ are higher than those returned by COMMIT without blurred streamlines. This happens because when we use the standard formulation we have many streamlines, i.e., the redundant ones, that can explain the signal corresponding to a real fiber trajectory, so the total signal is subdivided among them, resulting in overall small weights. Instead, if we remove the redundancy in the input tractogram, COMMIT$_{\text{blur}}$ will have very few streamlines to explain the same total contribution and therefore their weights will be higher. This behavior vanishes at the connectome level because in each cell we consider the signal fraction corresponding to the bundle connecting the two regions. Consequently, taking into account the connectomes, we computed the absolute distances and we used as reference the GT connectome. Likewise, since we are comparing different quantities, we have decided to use the CV instead of the simple standard deviation. We can also notice that the CV is higher for the streamline weights than for the connectomes. This is due to the method used to quantify the connections of the connectomes, which are obtained by summing the weights of all the streamlines connecting each pair of regions. Consequently, the amount of variations is decreased because we move to an higher level.

3.3.4 Qualitative evaluation on in vivo data

In light of the positive results obtained on the synthetic phantom, we tested the effectiveness of the blurred streamlines representation on in vivo data. Figure 3.10 shows, for one representative subject, the comparison between the GT map given in input to perform the fit (top), the maps obtained using the standard formulation (middle) and those obtained with the proposed streamline representation (bottom). The maps estimated when using the two different streamline representations are reported for each of the three

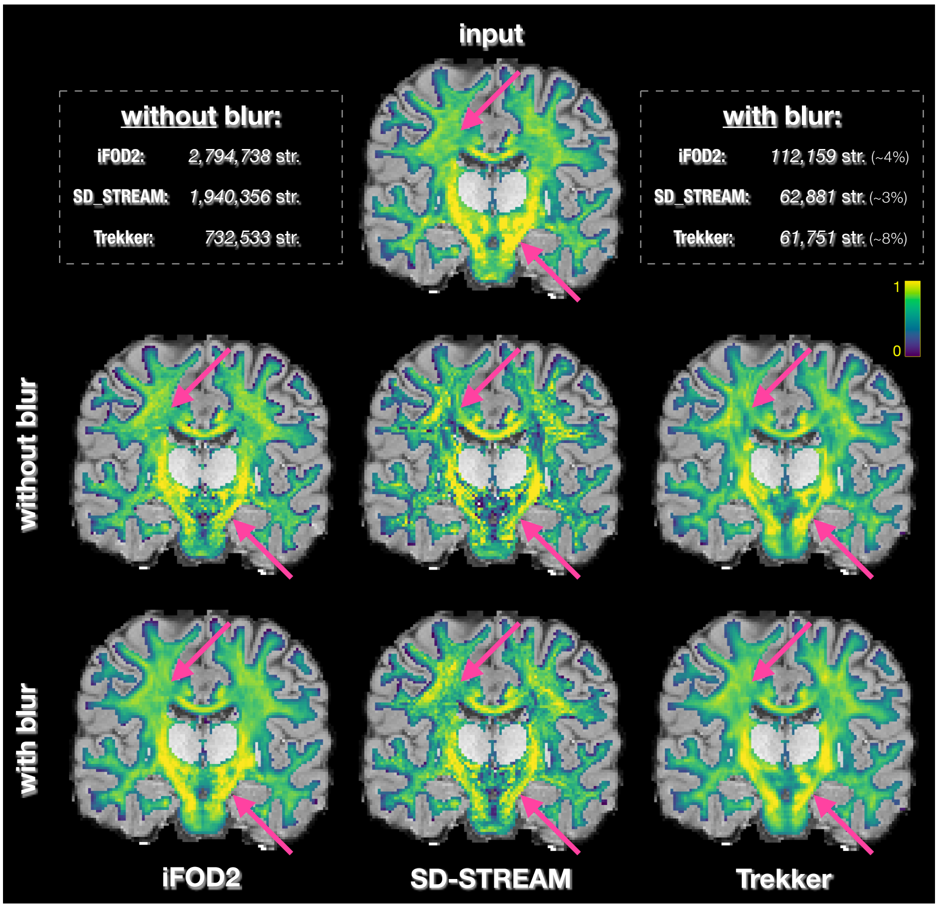

Figure 3.10: *Evaluation on in vivo data.* Coronal section of the intra-neurite volume fraction map used as input for the fit (top) as well as the maps estimated with COMMIT without (middle) and with (bottom) the blurred streamlines application. In addition to the maps estimated using three tractography algorithms, we report the number of streamlines (str.) of the input tractograms.

algorithms employed to perform tractography. As we can see, by using the blurred streamlines we are able to obtain similar estimates to the ones reconstructed with the standard method but using around 5% of the original streamlines. Moreover, the complete maps estimated by applying the blur appear more homogeneous, without drastic changes in intensity between neighboring voxels, which are not biologically realistic. Furthermore, if we focus on the regions pointed out by the arrows, using the blurred streamlines we can obtain a streamline density closer to the input one, for example, avoiding areas with very low values in the corona radiata.

Finally, Figure 3.11 shows the results on two well-known bundles, the Corpus Callosum (left half) and the Pyramidal Tract (right), reporting the contribution corresponding only to the streamlines belonging to the tract of interest. For a representative subject, we report the maps estimated both by the standard formulation of COMMIT and by the proposed approach giving in input the three different tractograms, together with the volume covered and the number of streamlines used to get the results. Thanks to the proposed representation the estimated bundles density is improved, appearing smoother while still maintaining the expected pattern along their path. In addition, looking at the outcome get from the three different tractography algorithms, the estimated maps appear closer between them when using the blurred streamlines. Finally, as reported in Figures 3.12 and 3.13, this behavior is repeated for all the ten subjects that we analyzed. We can also notice that, after the application of the proposed technique, the estimates are more similar among various subjects but preserving the anatomical differences.

3.3.5 General observations and future works

The proposed representation proved to be effective in drastically reducing the redundancy among streamlines, and consequently the collinearity in the linear operator of filtering methods, by using a combination of clustering and spatial blur of signal contributions. In the past, a Gaussian process representation for WM fiber bundles has already been employed for other purposes, e.g., (Wassermann et al., 2010; Wassermann et al., 2011). In particular,

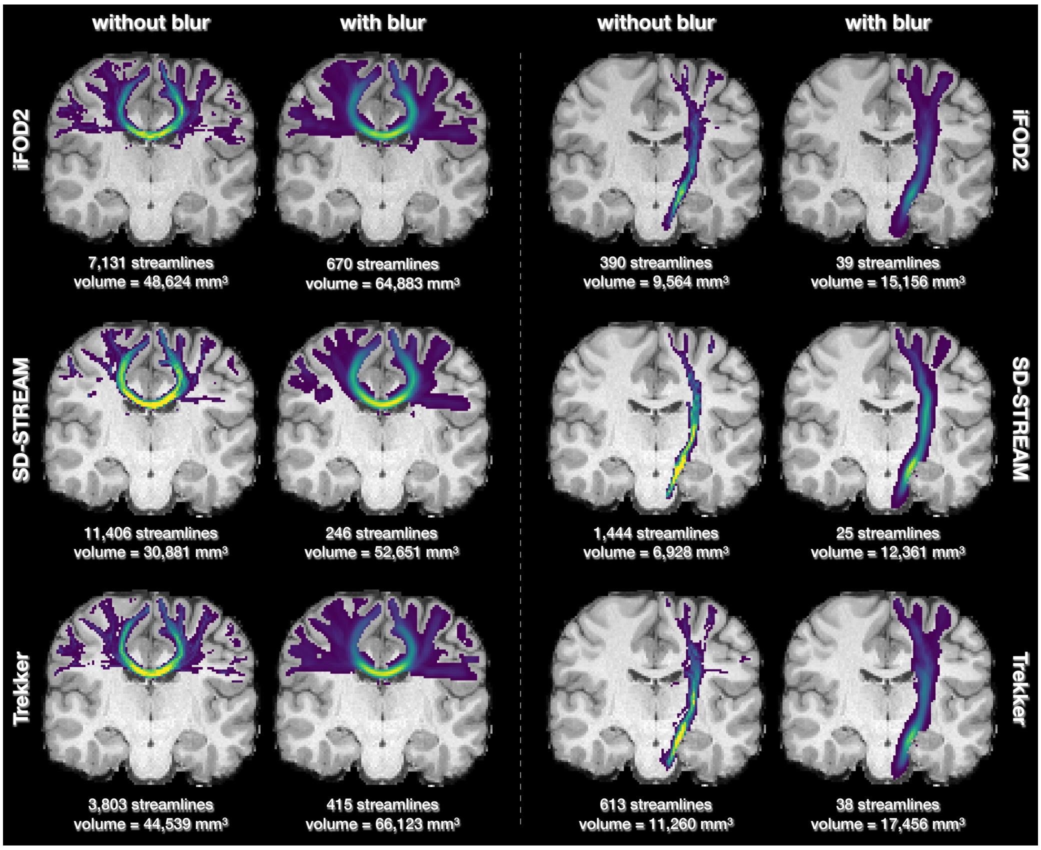

Figure 3.11: *Visual inspection of two well-known bundles.* For one representative subject, we report the coronal section of the intra-cellular compartment map corresponding only to the streamlines belonging to the Corpus Callosum (left) and to the left Pyramidal Tract (right). For each of the three tractography algorithms we compare the contribution maps estimated by the standard formulation and by the proposed blurred streamlines representation. Moreover, below each map we report the number of streamlines contributing to it and the volume covered.

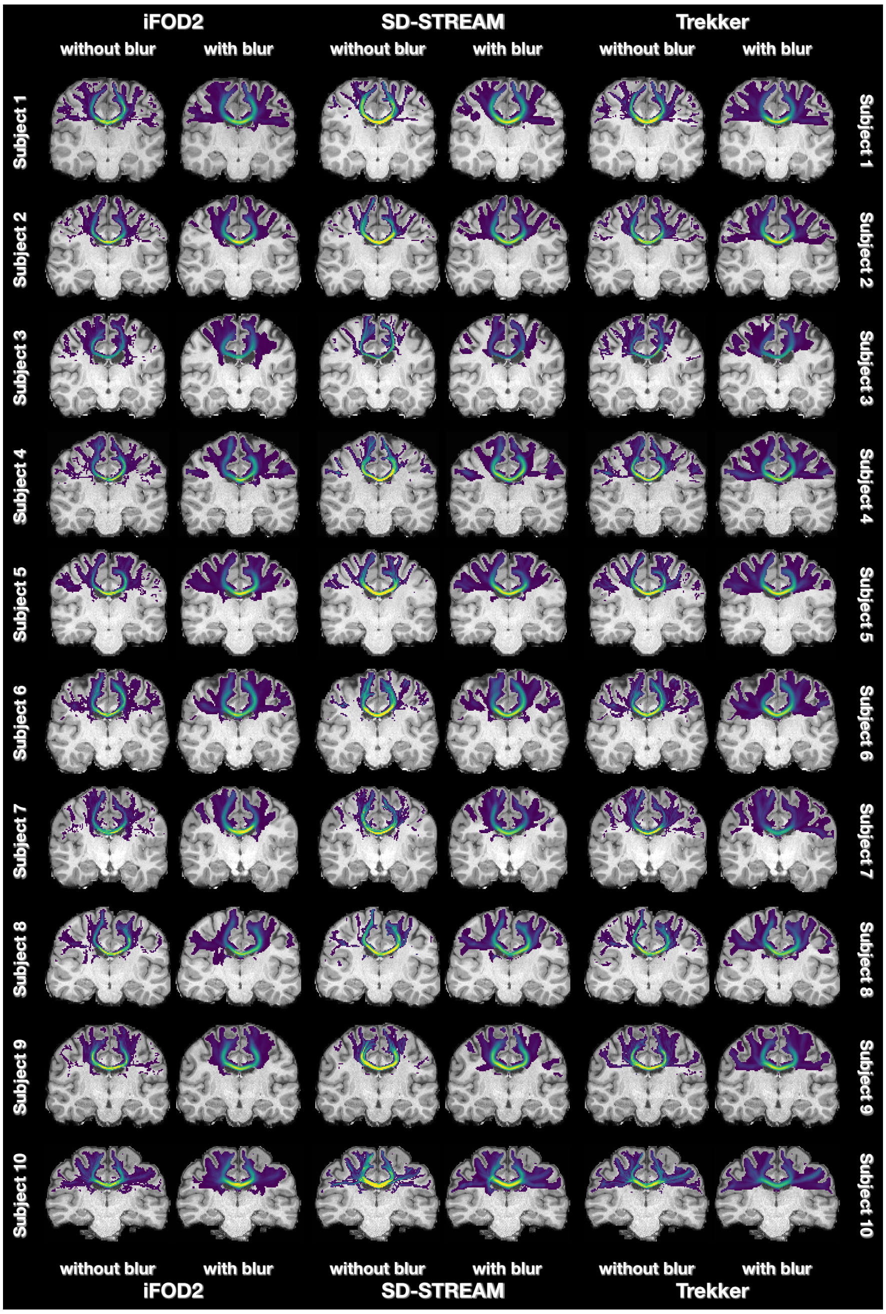

Figure 3.12: *Evaluation of real brain Corpus Callosum contribution.* For each of the three tractography algorithms we report the coronal section of the intra-cellular compartment map corresponding only to the streamlines belonging to the Corpus Callosum. We compare the contribution maps predicted by the standard formulation and by the proposed blurred streamlines representation. The results are showed for each of the 10 subjects analyzed.

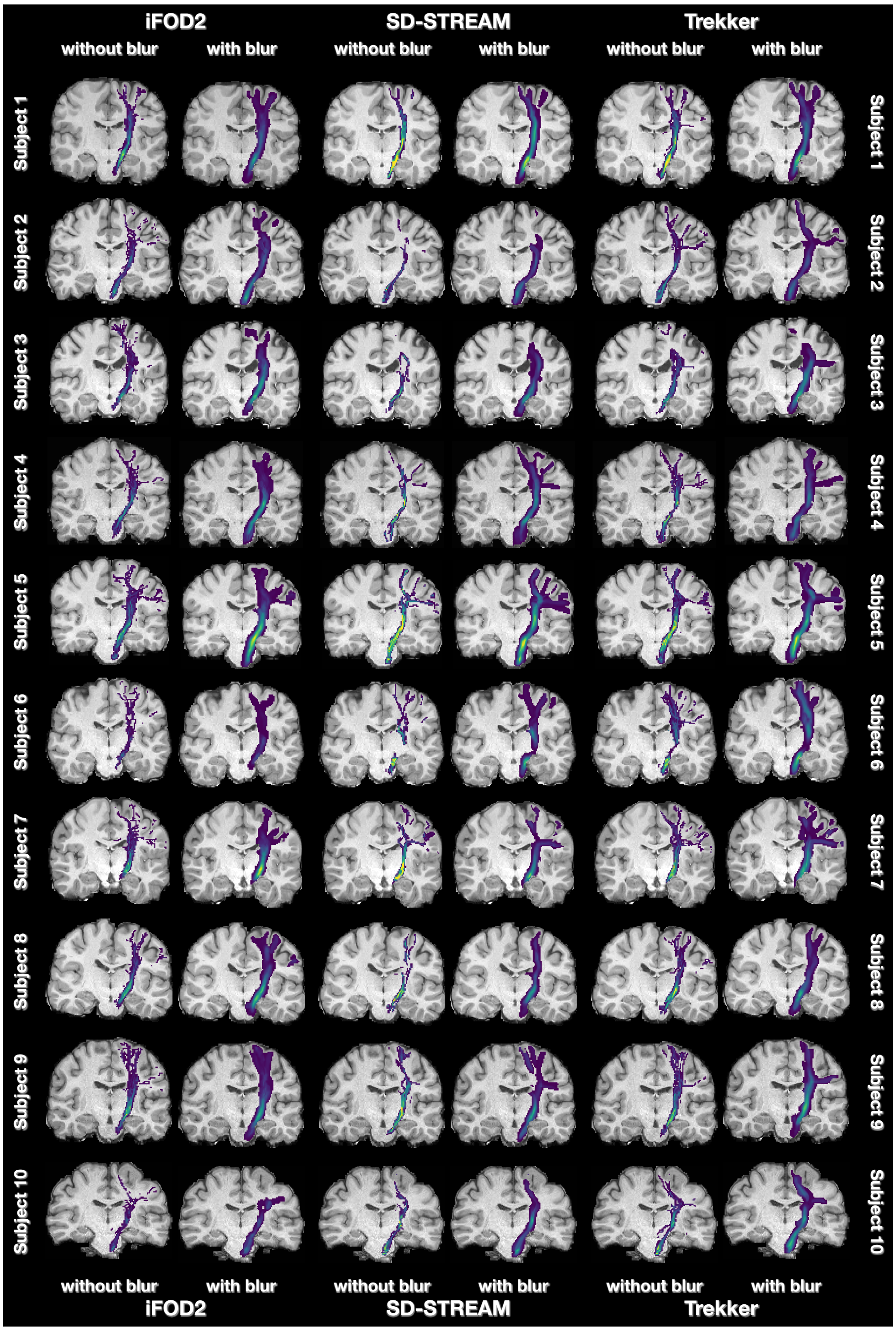

Figure 3.13: *Evaluation of real brain left Pyramidal Tract contribution.* As before, we report the coronal section of the intra-cellular compartment map corresponding only to the left Pyramidal Tract of the 10 subjects. We compare the contribution maps predicted by the standard formulation and by the proposed blurred streamlines representation.

Wassermann et al. (2010) took advantage of this mathematical framework to develop a hierarchical clustering algorithm. Despite being based on very similar concepts, i.e., clustering and Gaussian blur, their work significantly diverges from our blurred streamlines representation. Indeed, their primary objective is not to tackle the redundancy problem but to facilitate the mathematical operations between streamlines when performing statistical analysis of fibers bundles. Moreover, the clustering is a possible application of the framework and not a necessary step like in our new representation.

Other studies have explored the possibility of smoothing the connectome to get more reliable estimations of structural connectivity in test-retest data (Mansour L et al., 2022; Moyer et al., 2017). Both techniques require the use of a cortical mesh and apply a smoothing function during the construction of the connectivity matrix; instead, in this work we introduce a novel representation of streamlines in order to obtain more accurate estimations when using microstructure informed tractography. In future studies, it would be interesting to investigate how these techniques could benefit from the data-driven blur presented in this paper.

As we showed in the results, by removing redundant streamlines, the tractogram size substantially decreases, lowering the storage needs. Indeed, a typical whole-brain deterministic tractogram containing millions of streamlines has a file size of some gigabytes; for example, the SD_STREAM tractogram used in Figure 3.10 has about 2 million streamlines and occupies $\approx$ 6.15 GB. This makes it difficult to visualize and process tractograms, especially in case of clinical studies where hundreds or even thousands of subjects are usually involved (Mansour L. et al., 2023; Miller et al., 2016; Schilling et al., 2022a). Since with the blurred streamlines we are able to explain the acquired signal with the same accuracy as before, if we save both the clustered tractogram and the blur parameters we do not lose information and we can employ this representation as a *compression* technique. As an example, if we apply $\text{COMMIT}_{\text{blur}}$ to the representative tractogram mentioned before, 62,881 blurred streamlines are sufficient ($\approx 3\%$) requiring only 130 MB ($\approx 2\%$). Compression was not the main objective for the blurred streamlines representation but it would be interesting in future to study how it compares to existing techniques developed ad hoc for this purpose, e.g., (Haehn et al., 2020; Presseau et al., 2015).

Thanks to the blurred streamlines representation, we now have a tool which can allow us to determine precisely how many streamlines are required for a given data set. At the moment, this number is determined only empirically, by applying clustering to discard redundant trajectories and then adding the blur. Indeed, from the experiments shown above, we saw that less than 5% of all the streamlines are required but if we sample this number randomly we cannot obtain accurate results. This is due to the fact that by employing clustering we remove only the trajectories that are present many times while with a random sampling of the input tractogram we likely lose some of the necessary paths. It is worth noticing that the proposed representation is independent of the clustering technique employed, so one could replace QuickBundlesX (Garyfallidis et al., 2012, 2016) with more sophisticated algorithms, e.g., (Siless et al., 2018; Vázquez et al., 2020; Zhang et al., 2020). In future studies we will try to find a systematic way to quantify the optimal cardinality of the tractogram for an input data set.

Selecting the appropriate clustering threshold for a given tractogram is not straightforward; for the scope of this work, in our experiments we chose the first value that enabled us to drastically decrease the redundancy without affecting the quality of the reconstructions, and we did not further explore more sophisticated solutions to identify the optimal threshold. Moreover, the naive method that we employed to filter out outliers from the input tractogram may have side effects in specific situations. For example, as reported in Figure 3.7 A, using a small threshold the condition number is already surprisingly low. Since the streamlines resulting from iFOD2 reconstructions are very wavy, the mean distance between streamlines with the same principal trajectory can be high, in our case greater than t_o, resulting in a lot of clusters, each containing very few streamlines. Therefore, the majority of streamlines are wrongly considered as geometrical outliers and then filtered out from the tractogram. In this way, we do not have all the streamlines needed to properly cover the WM and consequently to explain the acquired signal (as shown in the bundle sections in Supp. Fig. 3.7 A). This highlights that to identify the best value for the clustering threshold *it is not sufficient to look at the condition number alone* but we also need to visually check that the blurred signal contributions of the centroids represent equally well the WM as before. Future research will evaluate the benefits of using more sophisticated approaches to remove outliers (like Aydogan, 2022; Côté et al., 2015), which could then allow us to better estimate the optimal threshold to be used for a given input tractogram.

Importantly, the spatial extent of the blur does not carry a direct anatomical interpretation, as it is introduced as a geometrical regularization mechanism rather than a biophysical model of fiber displacement. Future studies should assess how the choice of blur parameters interacts with factors such as bundle size, tract geometry, and image resolution, and whether systematic scaling rules can be established across datasets with different spatial characteristics.

In future investigations we plan to explore the possibility of using the blurred streamlines representation to combine together tractograms obtained from different tractography algorithms with the aim of increasing further the anatomical accuracy of the reconstructions. In fact, on the one hand merging multiple tractograms might lower the risk of false negatives but, on the other hand, this operation might as well dramatically increase the total number of redundant streamlines, thus worsening even more the collinearity effects described in this work. Thanks to the blurred streamlines representation we believe that this problem can be properly solved, since we can improve the quality of the set of candidate streamlines, we could obtain more biologically relevant tractograms and more accurate quantification estimates.

Finally, it would be very interesting to investigate the improvements that the blurred streamlines representation could bring when applied to other microstructure informed tractography methods based on linear formulations, like SIFT (Smith et al., 2013, 2015a), LiFE (Pestilli et al., 2014) and the more advanced versions of COMMIT (Ocampo-Pineda et al., 2021; Schiavi et al., 2022, 2020). Additionally, future efforts will intent to further investigate the impact of this novel streamline representation on other in vivo brain data, both for normal aging and for different diseases, analyzing the effects on structural connectivity metrics and the possible advantages in adopting it for clinical applications. Indeed, by employing the proposed representation, the number of objects under analysis is drastically reduced, substantially simplifing tractogram visualization and bundle extraction procedures. In particular, this dimensionality reduction opens the possibility of adopting more sophisticated clustering algorithms than those typically used, such as QuickBundles, which relies on the “Basic Sequential Algorithmic Scheme” (BSAS). As a result, more accurate and anatomically meaningful bundle segmentation strategies could become computationally feasible.

3.4 Conclusion

In this work, we called the attention of tractography users to the problematic presence of redundancy among the reconstructed streamlines and to the ramifications this may have when using tractography filtering techniques to boost the anatomical accuracy of the reconstructions. To mitigate this problem, we have introduced a novel way to define how a streamline contributes to the signal in the voxels, called *blurred streamlines*, and tested it in combination with COMMIT. Our results look very promising and suggest that our novel streamline representation represents a viable and effective solution to further improve the quality of tractography reconstructions and enable more advanced methodological developments, like those presented in the following Chapters (4 and 5).

Chapter 4

Synergy of different algorithms for improved tractography

4.1 Motivation

Despite its advantages, tractography faces some known limitations and challenges, which arise from its being an ill-posed inverse problem that aims to map the complex architecture of WM (Daducci et al., 2025; Rheault et al., 2025a,c; Zhang et al., 2022) (see Section 2.3.2.5 for more details). One of the main issues is the high variability of the reconstructed fiber trajectories, which derives from the choices made throughout the preprocessing and tracking pipeline (Bastiani et al., 2012; Nath et al., 2020; Schilling et al., 2019a, 2021; Thomas et al., 2014). Currently, numerous tractography algorithms exist, each with peculiar strengths and weaknesses, and each requiring the setting of various parameters that influence the tracking process. Some international challenges have shown that, starting from the same data, the methods and procedures employed can radically alter the outcomes of connectivity studies, bundle segmentation, and microstructural feature estimation (Schilling et al., 2025). As illustrated in Figure 4.1, this variability leads to poor anatomical reliability, with individual tractography reconstructions typically providing only a partial or biased view of the actual brain organization. This problem is further complicated by the lack of a ground truth (GT) to compare the results, which limits the ability to validate tractography methods (Rheault et al., 2025c). Moreover, there is no agreement on the optimal tractography pipeline to use in any experimental setting, but the choice of methods and parameters must be tailored to the specific application (Schilling et al., 2025).

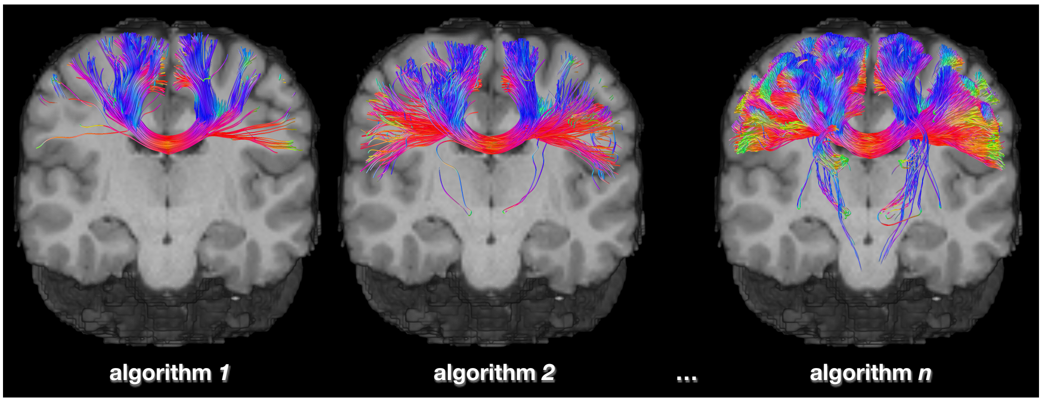

Figure 4.1: *Issue addressed in this study.* In brain tractography, several algorithms have been developed, each with specific strengths and limitations. This leads to considerable anatomical variability in the reconstructed pathways, with outcomes highly influenced by the method chosen for tractogram generation. The problem of low anatomical reliability becomes more evident when extracting a specific bundle from the whole-brain tractogram.

As mentioned before in Sections 2.3.2.5 and 2.4.2, to improve the anatomical accuracy of tractography, it is of paramount importance to reconstruct all the TP fiber bundles while reducing the FP ones to a minimum (Zalesky et al., 2016). Effective solutions exist to identify and filter out spurious connections (Ocampo-Pineda et al., 2021; Schiavi et al., 2020), but the TPs are limited to those recovered by the algorithm chosen to generate the tractogram. So, our proposed idea to enhance the set of candidate streamlines and reduce algorithm- and parameter-dependency in tractography is to merge multiple reconstructions generated using different techniques. This approach draws inspiration from ensemble methods used in statistics and machine learning to improve predictive performance compared with that of any individual algorithm constituting the ensemble (Mienye and Sun, 2022; Sagi and Rokach, 2018). This idea was previously explored in the context of tractography by

Takemura et al. (2016), where multiple tractograms obtained from varying parameters of the same algorithm were merged together. However, recent studies have highlighted two critical challenges associated with this simple merging strategy that were previously overlooked. In fact, merging several tractograms naturally tend to increase the number of FP connections (Maier-Hein et al., 2017), necessitating adequate filtering solutions to remove the trajectories that are not compatible with brain anatomy. Furthermore, since pathways that are easier to reconstruct will appear repeatedly across algorithms, this over-representation leads to a significant increase in redundancy in the final tractogram and, as demonstrated by recent studies, to a reduced performance of filtering techniques in removing FPs in the latter (Gabusi et al., 2024; Persson and Moreno, 2024).

In this study, we propose a novel approach designed to decrease the high variability present in tractography reconstructions obtained from the same dMRI data by allowing different methods to work in synergy[1]. We begin by detailing the processing pipeline used to generate the so-called *synergy tractogram*, including specific measures to handle FPs and reduce redundancy. By incorporating multiple tractograms, we aim to leverage algorithmic diversity to achieve synergy, thereby increasing the quality of true connections and producing more biologically plausible estimates that better reflect the brain's actual WM structure. Next, we present a quantitative evaluation of the proposed method's performance, comparing it with three widely used individual algorithms through numerical simulations. Finally, we apply our method to in vivo data and assess the improvements in the final reconstructions and the resulting robustness.

4.2 Materials and methods

The proposed approach (Figure 4.2) constructs the *synergy tractogram* by merging multiple tractography reconstructions obtained with different algo-

---

[1] *Synergy* refers to the phenomenon in which the combined action of two or more elements working together produces an effect greater than the sum of their individual components.

rithms, and subsequently refining this combined set of streamlines through microstructure informed filtering to produce a robust, biologically plausible, and quantitative representation of WM pathways. We first generate various tractograms using different fiber-tracking algorithms, each exhibiting distinct strengths and limitations. For example, deterministic methods often yield streamlines with high anatomical plausibility but are limited in their ability to recover complex trajectories, which can lead to false negatives. Conversely, probabilistic techniques explore a wider range of possible pathways, increasing sensitivity at the cost of introducing more false positives due to reduced specificity. To mitigate the variability arising from methodological differences, we merge all generated tractograms into a single combined one. This provides an expanded set of candidate streamlines, with the more easily reconstructed pathways represented multiple times. We then refine the combined tractogram using a multi-step procedure to simultaneously addresses redundancy among streamlines, discards FP bundles incompatible with the acquired signal, and yields accurate quantitative estimates of structural connectivity.

Among the available microstructure informed tractography techniques, in this work we employ the recent advancements implemented in the COMMIT framework (Daducci et al., 2013, 2015) because its formulation is powerful and highly adaptable, allowing the use of various additive multi-compartment models and multi-modal data (Sections 2.4.1.3 and 2.4.1.4). In our study, we rely on two extensions of COMMIT — COMMIT2 (Schiavi et al., 2020) and the blurred streamlines representation (Gabusi et al., 2024) — to respectively address the issues of FPs and redundancy. As explained in Section 2.4.1.4, COMMIT2 incorporates anatomical priors on WM and adds an adaptive group lasso regularization term to the standard formulation (Eq. 2.32), allowing the removal of entire bundles when unsupported by the data (Schiavi et al., 2020). Instead, the blurred streamlines representation mitigates collinearity-related issues that arise in the linear formulations due to the high redundancy present in the input tractograms (Gabusi et al., 2024). The details about how $\text{COMMIT}_{\text{blur}}$ operates are carefully delineated in Chapter 3.

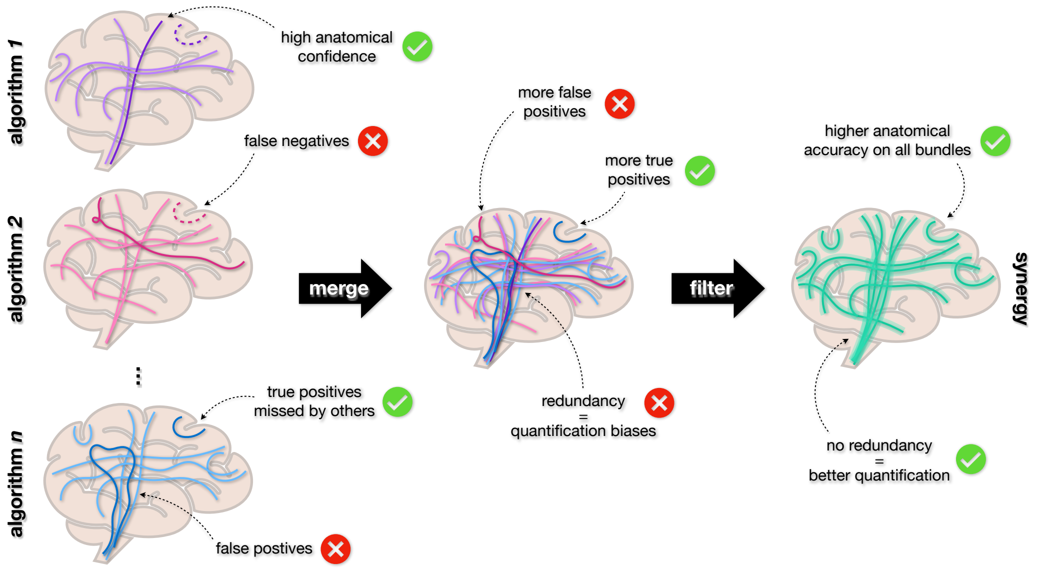

Figure 4.2: *Proposed approach.* The synergy tractogram is generated by combining multiple tractograms reconstructed with different algorithms and parameter settings, each with distinct advantages and limitations. The combined tractogram is refined using microstructure informed tractography to reduce redundancy and filter out false positives. The resulting tractogram achieves higher anatomical accuracy in bundle estimation, enabling a more reliable quantification of structural connectivity.

4.2.1 Combining reconstructions by different algorithms

The workflow for constructing the synergy tractogram begins with the generation of multiple tractograms using different tractography algorithms and/or parameter settings. Then, it is necessary to remove redundancy among streamlines in two distinct moments of the pipeline. First, before merging the individual tractograms into a single one, we introduce a preprocessing step to mitigate potential strong differences in local streamline density between different tracking approaches, which may negatively impact the accuracy of later stages.

As illustrated at the top of Figure 4.3, when considering the streamlines representing a single fiber population within a small WM region (approximately 2–3 voxels), its coverage can vary substantially between algorithms.

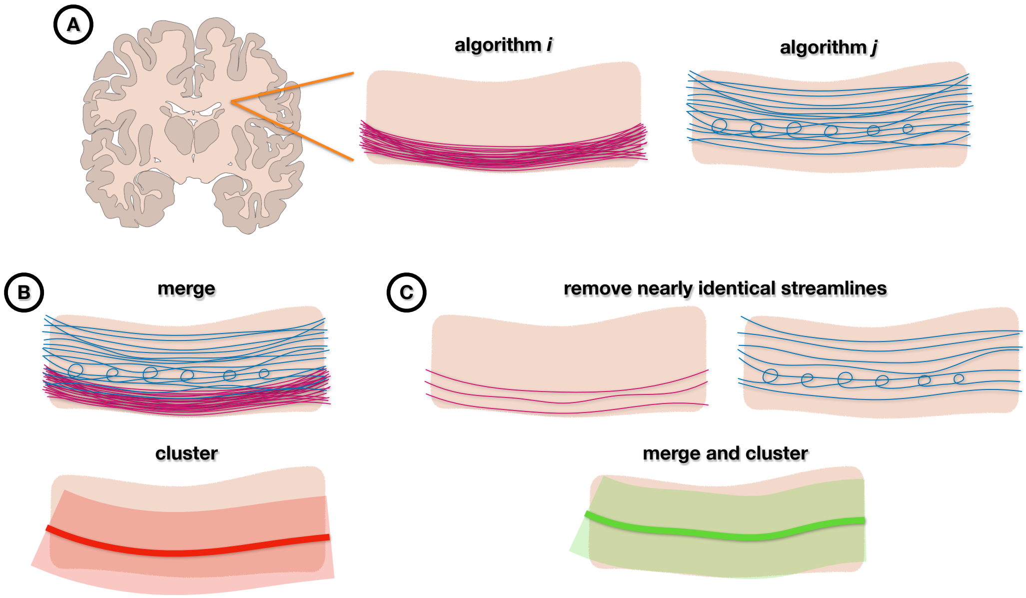

Figure 4.3: *Possible strategies for combining the individual reconstructions.* At the top, an example is shown of how streamlines belonging to the same anatomical tract are distributed, as generated by two different algorithms within a small WM region ($\approx$ 2–3 voxels). As illustrated on the left, simply combining the two sets and then running clustering directly shifts the centroid toward the lower area, where the majority of streamlines are located. Instead, balancing the distributions by removing nearly identical streamlines before merging yields a better-positioned centroid that represents the original covered area when blurred (bottom right).

Even when the same number of streamlines is generated, deterministic algorithms tend to produce localized groups of highly similar streamlines, yielding a narrower spatial distribution than that obtained from probabilistic methods. If the streamlines from different tractograms were merged directly, the subsequent clustering would likely produce a centroid that poorly reflects the actual distribution of the streamlines. Indeed, the centroid is computed as the point-wise mean of all the streamlines in the considered cluster. As shown in the bottom left panel of Figure 4.3, its trajectory will be biased toward the denser area, e.g., over-represented by deterministic streamlines, leaving the opposite WM side not covered.

To address this issue, we apply QuickBundles (Garyfallidis et al., 2012) clustering with a small threshold (t_1) to each tractogram prior to merging (Figure 4.3, bottom right). For each cluster, we retain only one of the closest streamline to the corresponding centroid, while discarding the remaining ones, which can be considered nearly identical. As a result, each individual tractogram now contains only a subset of the initial streamlines, and their distribution in the combined tractogram will be more balanced.

4.2.2 Refining the combined tractogram

After removing nearly identical streamlines from the individual tractograms and merging them into a single one, we apply a microstructure informed tractography method to obtain the synergy tractogram. To simultaneously address redundancy and filter out FP connections, we combine the blurred streamlines representation (Gabusi et al., 2024) with COMMIT2 (Schiavi et al., 2020).

In this method, the combined tractogram is first processed to remove geometrical outliers, i.e., streamlines with implausible trajectories, using *purifibre* (Aydogan, 2022). This processing step improves the robustness of the subsequent clustering used to reduce redundancy (Gabusi et al., 2024). Thanks to the adoption of the strategy detailed in Section 4.2.1, when all the streamlines derived from the different individual tractograms are clustered together, the resulting centroids provide a more faithful representation (as shown in the bottom right panel of Figure 4.3). After clustering the tractogram using a threshold t_2, as representative streamlines for each cluster, we retain the average centroid but replace its ending points with those of a streamline in the same cluster that are closest to the computed ones. This adjustment ensures that the trajectories connect to the appropriate GM regions, and we apply a subtle smoothing to avoid sharp angles. These centroids are then spatially blurred to guarantee proper WM coverage while reducing collinearity in the linear operator $\mathbf{A}$ (Eq. 2.29). Fitting is subsequently performed using COMMIT2 formulation (Eq. 2.32), where groups are defined according to the pair of GM regions connected.

The group lasso regularization, modulated by the λ parameter, removes the majority of FP connections. In particular, because sparsity is promoted at the group level, streamlines belonging to bundles not compatible with the acquired signal are assigned zero weights, while the remaining streamlines have positive values. We therefore apply thresholding at zero to preserve only relevant groups in the tractogram. However, lasso regularization is known to shrink non-zero coefficients toward zero, introducing bias in the retained estimates. To mitigate this effect, we adopt a two-stage process inspired by relaxed lasso (Meinshausen, 2007): after employing the group lasso regularization, we perform a second fit using the standard NNLS formulation (Eq. 2.29). This *debiasing step* on the reduced problem yields streamline weights that are less biased toward zero and provide more accurate estimates of their actual contributions to the acquired signal.

The tractogram obtained through this filtering step constitutes the final synergy reconstruction, which is then evaluated according to the experiments detailed in the following sections.

4.2.3 Experiments

4.2.3.1 Dataset and processing

We evaluated the performance of the proposed method using both numerical simulations and in vivo data. Specifically, we used the *ISBI2013* phantom as a synthetic dataset, while the in vivo experiments included data from 10 healthy subjects sourced from the HCP test-retest dataset. These two datasets are the same used to evaluate the blurred streamlines representation; for more details, please refer to Section 3.2.3.

Tractography estimation was performed on FODs computed in each voxel using Constrained Spherical Deconvolution (Tournier et al., 2007); for the HCP dataset, we applied its multi-shell multi-tissue variant (Jeurissen et al., 2014). We employed three different tractography methods, using default parameters unless otherwise specified: one deterministic algorithm, *SD_STREAM* (Tournier et al., 2012), and two probabilistic, *iFOD2* (Tournier et al., 2010) and *Trekker* (Aydogan and Shi, 2021). For the ISBI2013 dataset, we generated 1 million streamlines per tractogram, seeding within the WM mask. For the HCP dataset, 3 million streamlines were reconstructed for each tractogram (1 million for Trekker), limiting their length between 5 mm and 250 mm, and retaining only streamlines connecting GM regions. For the seeding, we used the WM mask except for the reconstructions with iFOD2, where we employed Anatomically-Constrained Tractography to mitigate the number of spurious trajectories (Smith et al., 2012). The cutoff values were set to 0.06 for iFOD2 and 0.05 for SD_STREAM, with a step size of 0.25 mm for SD_STREAM and a maximum curvature angle of 70° for both.

4.2.3.2 Quantitative validation on sythetic data

In the quantitative evaluation on synthetic data, we generated the synergy tractogram following the procedure outlined above, and we compared the accuracy of its estimates with those of the three individual tractograms used to construct it. Specifically, we set the initial clustering threshold t_1 to 0.25 mm and discarded 3% of streamlines from the combined tractogram using purifibre with a voxel dimension of 1 mm. For the blurred streamlines representation, we used $t_r = 0.8$ mm, $r_c = 0.8$ mm, and $r_g = 0.5$ mm, and group sparsity was promoted using $\lambda = 0.03$. The three individual tractograms were also processed applying COMMIT2 with the blurred streamlines representation using the same parameters, except for $\lambda = 0.025$ and different clustering thresholds: $t_r = 0.4$ mm for SD_STREAM and $t_r = 0.8$ mm for iFOD2 and Trekker. QuickBundles (Garyfallidis et al., 2012) is a sequential algorithm whose results depend on the order of streamlines processing. To mitigate this bias, we repeated the entire procedure 10 times and computed the following evaluation metrics for each run.

To assess the accuracy of the reconstructed connectomes, we computed the L1 distance between the estimated connectome ($\tilde{C}$) and the ground-truth one (C), defined as:

$$L1\left(\tilde{C}, C\right) = \sum_{i,j=1}^{N} \left|\tilde{C}_{i,j} - C_{i,j}\right| \;, \tag{4.1}$$

where N is the number of nodes in the connectome. To evaluate specificity and sensitivity, we examined the number of TP and FP connections. TP bundles correspond to the 27 connections present in the ISBI2013 dataset configuration, whereas FP bundles are those reconstructed by tractography algorithms that are not anatomically plausible, as their trajectories are not supported by the ground-truth structure. Finally, the fitting error of the model was estimated by calculating the Root Mean Squared Error (RMSE) between the estimated signal ($\tilde{S}$) and the ground-truth signal (S) across all WM voxels (V), as follows:

$$RMSE\left(\tilde{S}, S\right) = \sqrt{\frac{\sum_{v=1}^{V}\left(\tilde{S}_v - S_v\right)^2}{V}}\,. \tag{4.2}$$

4.2.3.3 Robustness evaluation on in vivo data

As discussed in (Dyrby et al., 2025), since validating tractography methods in vivo remains an open challenge due to the lack of GT, their reproducibility should be inspected. We therefore evaluated the performance of the proposed method on real brain data by comparing its robustness with that of the three individual algorithms used to construct it.

First, to assess intra-subject reproducibility, we examined the effect of the variability introduced by the tracking process. To this end, we focused on a single subject from the HCP dataset, specifically the baseline scan of subject 103818, for which we reconstructed and processed each tractogram type 10 times (details in Section 4.2.3.1). We generated the synergy tractogram with the following parameters: $t_1 = 1.0$ mm, 20% and a voxel size of 2 mm for purifibre, $t_r = 2.25$ mm ($t_r = 2.00$ mm for individual tractograms), $r_c = 2.0$ mm, and $r_g = 0.75$ mm. Regarding the promotion of group-level sparsity, we tested different values of the regularization parameter, and we report here the optimal results obtained using $\lambda = 8 \times 10^{-5}$ for the synergy tractogram and $\lambda = 6 \times 10^{-6}$, $\lambda = 7 \times 10^{-5}$ and $\lambda = 10^{-4}$ for SD_STREAM, iFOD2, and Trekker, respectively.

To evaluate the results, we first investigated the voxelwise fitting error ($E = \left|\tilde{S}_v - S_v\right|$) by computing the average and standard deviation maps across the 10 repetitions. Instead, to analyse the inter-subject robustness, we considered the Dice coefficient across the 10 repetitions for all bundles defined by the GM parcellation. Specifically, we extracted the streamlines connecting each pair of GM regions from each tractogram. Then, we isolated the contribution map corresponding only to the bundle under consideration from the overall streamline density estimated by COMMIT. For each bundle, we finally computed the Dice coefficient between all pairs of runs as:

$$D\left(IC_a, IC_b\right) = \frac{2\left|IC_a \cap IC_b\right|}{\left|IC_a\right| + \left|IC_b\right|}\ , \tag{4.3}$$

where IC_a and IC_b are two maps of the same bundle obtained by different repetitions.

Finally, we investigate the variability between multiple acquisitions of different subjects of the HCP dataset. In particular, we processed both baseline and retest scans of the selected 10 subjects (details in Section 4.2.3.1). For each of them, the synergy tractogram has been generated using the same parameter setting employed for the single-subject analysis described above. Beyond evaluating the fitting error (Eq. 4.2) of each run of the COMMIT optimization, we focused our robustness analysis on the Corpus Callosum tract. We followed the Tractostorm 2 guidelines (Rheault et al., 2022) to virtually dissect it from each of the filtered tractograms. Then, as before, we extracted the intra-cellular signal contribution of the streamlines belonging to this bundle, as estimated by COMMIT2 with the blurred streamlines representation. For each subject, we aligned the estimated retest maps to the baseline space using FSL linear registration (Jenkinson et al., 2002), and we computed the Dice coefficient (Eq. 4.3) to quantify the interscan bundle similarity.

4.3 Results and discussion

4.3.1 Performance assessment on synthetic data

We first validated our approach using the ISBI2013 synthetic data. Specifically, we examined both the fitting error and the accuracy of the resulting estimates, comparing the performance of synergy tractogram against that of the three individual tractograms used to construct it. As described in Section 4.2.3.2, we repeated the analysis 10 times by randomly shuffling the streamlines' order to mitigate its impact on the estimates, due to the sequential nature of QuickBundles clustering. Results are therefore presented in Figure 4.4 as barplots, showing the average value of each metric together with the corresponding standard deviation.

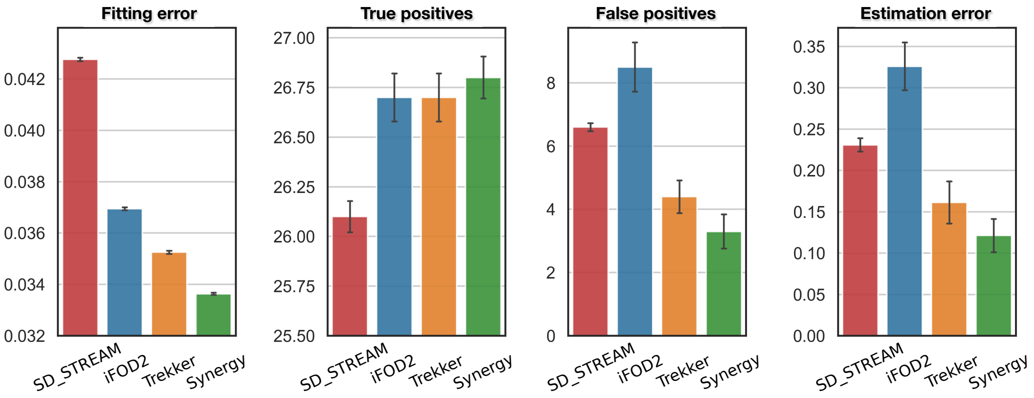

Figure 4.4: *Method validation on synthetic dataset.* The plots compare the results obtained for the four tractograms: three individual and the synergy one. Reported metrics include fitting error (i.e., RMSE), the number of true-positive and false-positive bundles, and the estimation error (i.e., L1 distance), shown as mean values with standard deviations across 10 repetitions.

The first plot shows that the fitting error (RMSE) obtained with the synergy tractogram is lower than that of the three individual tractograms. This indicates that the proposed approach yields an estimated signal that more closely matches the acquired one, thereby reducing the overall error in WM. When considering the number of TP and FP connections, the synergy tractogram again demonstrates superior performance. It more consistently identifies all 27 TP bundles while minimizing spurious pathways, thereby improving both sensitivity and specificity. Similarly, the lower average values of L1 distance reveal that the synergy tractogram achieves a smaller estimation error in the reconstructed bundle organization compared to each individual tractogram. This demonstrates that combining multiple reconstructions yields more quantitative estimates closer to the GT than any single tractogram.

Overall, the synergy tractogram outperformed all individual approaches across every metrics. In Figure 4.5, we also report the results in terms of the L2 distance and the weighted mean coefficient of variation (computed following the definition in (Smith et al., 2015b)). The proposed approach consistently produced more accurate quantitative estimates, characterized by smaller distances from the GT, fewer FPs, and a greater number of true connections, while maintaining a lower fitting error. These findings indicate that merging multiple tractograms generates more truthful and reliable reconstructions than using any single algorithm alone.

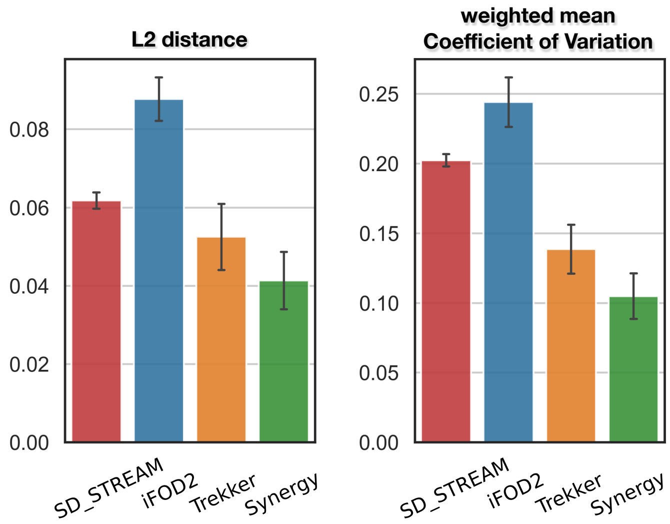

Figure 4.5: *Additional results of the method validation.* We report in these plots two additional metrics considered in the quantitative evaluation on synthetic data. Specifically, we employed the L2 distance between the estimated connectome and the GT and the weighted mean coefficient of variation (computed following the definition in (Smith et al., 2015b)). For both metrics, the synergy tractogram provides lower values than those of individual methods, indicating a more accurate connectome estimation.

4.3.2 Reliability analysis on in vivo data

4.3.2.1 Intra-subject variability

After validating the method on synthetic data, we examined intra-subject robustness in vivo. Specifically, we first analysed the variability due to the tracking process by considering a single subject and repeating tractogram generation 10 times. On the resulting data, we investigated the voxel-wise fitting error across repetitions, reporting the average and the standard deviation in Figure 4.6. For both metrics, we compare the synergy tractogram with the three individual tractograms used to construct it.

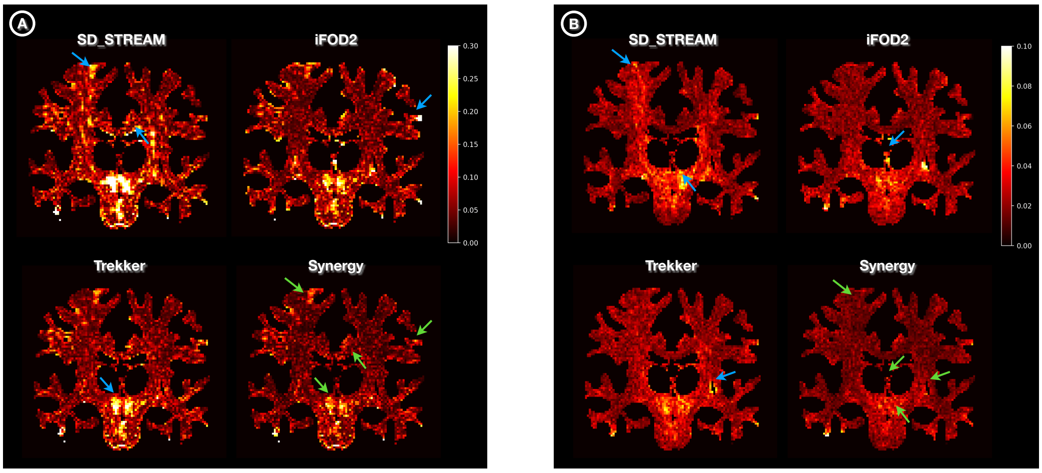

Figure 4.6: *Intra-subject variability in the fitting error.* For each tractogram, voxelwise maps of the average (A) and standard deviation (B) of the fitting error across 10 repetitions. Arrows highlight regions with notable improvement when using the synergy tractogram compared to individual reconstructions.

In panel (A), the map corresponding to the synergy tractogram clearly exhibits lower average voxel-wise fitting error than the individual tractograms across the 10 repetitions, as highlighted by green arrows. In Figure 4.6(B), light blue arrows indicate regions of high variability in the individual tractograms, while the corresponding regions in the synergy map (highlighted in green) display clearly reduced standard deviation values. These results demontrate that the proposed approach offers a better fit to the acquired signal, indicating that the estimates are less variable and less influenced by the specific streamline displacements generated by individual runs of a given algorithm.

To further investigate robustness, we examined the Dice coefficient of individual bundles to assess spatial consistency across repetitions. We considered two categories: bundles retrieved in all 10 repetitions (100%) and bundles retrieved in at least five (≥50%). The results are shown in Figure 4.7, where violin plots illustrate the distribution of Dice values, highlighting the median and quartile values.

Figure 4.7: *Tract-level reproducibility across repetitions.* Dice coefficient for all connections defined by the GM parcellation. Bundles were grouped into those present in all 10 repetitions (100%) and those retrieved in at least half (≥ 50%). Violin plots show the distribution for each tractogram, with the median and quartiles indicated.

Among the four tractograms, SD_STREAM displays the highest Dice values for both groups of bundles (0.759 ± 0.155 for always-retrieved bundles and 0.195 ± 0.138 for the others), indicating lower variability in tract reconstruction. However, as shown earlier in Figure 4.6, this algorithm also yielded the highest fitting error. This outcome can be attributed to the deterministic nature of SD_STREAM, which results in reconstructing major WM tracts with higher anatomical confidence but produces many false negatives. Considering the remaining methods, the synergy tractogram achieved higher median and quartile values compared to iFOD2 and Trekker, indicating better tract-specific reliability across both categories (always-retrieved bundles: 0.712 ± 0.174 vs. 0.700 ± 0.188 and 0.694 ± 0.175; other group: 0.155 ± 0.132 vs. 0.123 ± 0.117 and 0.147 ± 0.130 for iFOD2 and Trekker, respectively). Notably, the lower bound for the 100% category in the synergy tractogram exceeds that of all other methods. These findings confirm that synergy tractogram yields lower intra-subject variability and greater robustness to tracking-related differences.

4.3.2.2 Inter-scan robustness

We next assessed inter-scan reproducibility using 10 subjects with baseline and retest acquisitions. We first computed the RMSE for each baseline data to confirm the improvements obtained with the previous tests. This analysis established that the synergy tractogram achieved a lower average fitting error of 0.076, compared to employing individual tractograms: 0.160, 0.101, and 0.085 for SD_STREAM, iFOD2, and Trekker, respectively.

Then, we focused our examination on the reconstruction of a well-known WM tract, i.e., the Corpus Callosum. Figure 4.8 shows results for a representative subject, where the estimated density map of the streamlines belonging to this tract is displayed. The synergy reconstruction provides improved coverage and density characterization, producing a representation that more faithfully reflects the anatomy of the Corpus Callosum. In contrast, individual tractograms show more pronounced differences in the estimated maps, with some expected branching and fanning often missing from the final reconstructions.

Finally, we evaluated the similarity between the estimates obtained from the two scans of each subject. After registering the Corpus Callosum contribution image resulting from the second time-point acquisition (i.e., retest data) in the baseline space, we computed the Dice coefficients between these streamline density maps. The synergy tractogram achieved a similarity of 0.881 ± 0.0414, exceeding that of individual methods (0.751 ± 0.0629 for iFOD2, 0.864 ± 0.0402 for SD_STREAM, and 0.875 ± 0.0487 for Trekker)

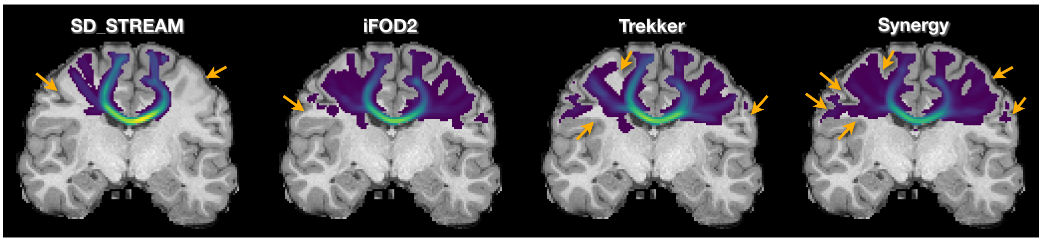

Figure 4.8: *Inter-scan robustness in vivo.* Example of the Corpus Callosum from a representative subject, comparing reconstructions from the three individual tractograms and the synergy one. As highlighted by the arrows, the synergy method enhances the spatial coverage of the tract.

across the 10 subjects. These results demonstrate that the proposed method is more robust to variations in the input data beyond those introduced by the tracking process alone, and it is able to improve the anatomical estimations of tractography.

4.3.3 Advantages of combining different algorithms in synergy

The proposed tractography method builds upon the concept of integrating information from multiple tracking algorithms belonging to distinct classes, thus capitalising on their respective strengths while mitigating their weaknesses. By taking advantage of various tracking algorithms that work in synergy, the proposed method is able to reduce anatomical variability, thereby increasing the accuracy of WM architecture reconstructions.

The validation tests demonstrated that the proposed synergy approach enhances the performance compared to standard tractography. In particular, this improvement is achieved by effectively lowering the fitting error and providing more accurate estimates in terms of both sensitivity and specificity, as well as overall distance from the GT. Furthermore, in vivo evaluations confirmed these advantages: the synergy tractogram exhibited higher anatomical reliability than individual ones. The provided estimates are more robust not only to the variability introduced by the tracking process itself (intra-subject analysis) but also to the differences present when performing multiple acquisitions (inter-scan examination).

Overall, these results indicate that the proposed approach reduces dependence on a single tracking algorithm and produces reconstructions that are both more accurate and more reproducible. By combining complementary information from independent algorithms and leveraging the redundancy reduction and advanced filtering provided by COMMIT2 and the blurred streamlines representation, the resulting tractograms better capture the underlying WM structure while limiting variability. The method presented in this work, therefore, represents a promising step toward more robust and reliable quantitative estimates of structural connectivity.

4.3.4 Limitations and future works

A first limitation of the proposed method is related to computational time. Because the method relies on combining tractograms with different characteristics, multiple runs of the tracking process are required to generate the input tractograms for the synergy generation. However, the processing with the COMMIT extension takes approximately the same time whether applied to an individual or combined tractogram, and therefore does not substantially increase the overall runtime of the pipeline.

Another aspect concernes the prefiltering step used to balance streamline distributions before merging individual tractograms. This is essential for obtaining accurate, representative streamlines when removing the redundancy introduced by the merging process. As demonstrated in Figure 4.9, employing a naive approach that simply concatenates all streamlines without prefiltering leads to poorer performance compared to the proposed strategy. In this work, clustering with a small threshold provided a simple yet effective solution to reduce imprecise centroids. Future developments will explore more advanced techniques for balancing streamline distributions to further improve the quality of combined tractograms.

Additional refinements could also be achieved by testing different combinations of tractography algorithms, including both commonly used and less

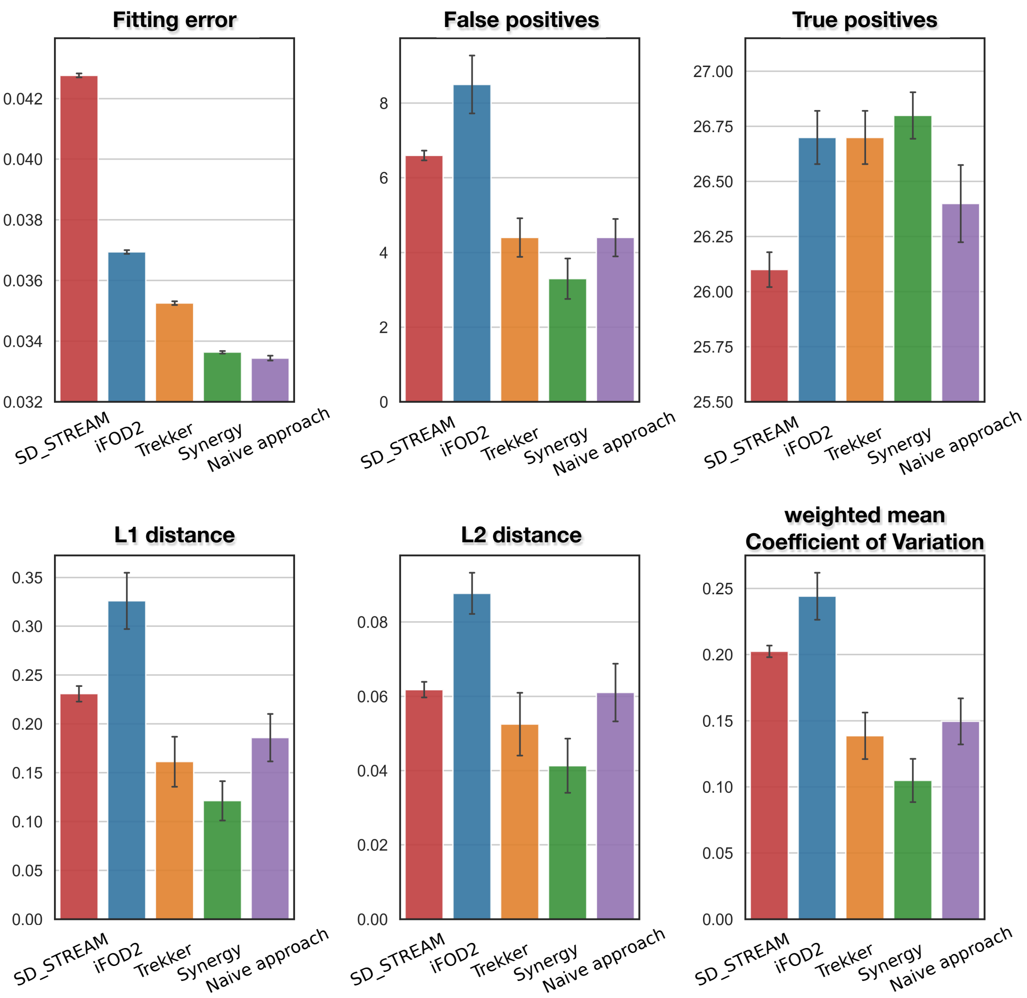

Figure 4.9: *Proof of concept for the prefiltering step during the merging.* We tested the performance of a more naive approach for the reconstruction of the synergy tractogram. Specifically, we simply merged the different individual tractograms, without performing the pre-filtering step to balance the streamlines' distributions, and then we filtered the resulting tractogram using COMMIT2 with the blurerd streamlines representation (as explained in Section 4.2.2). In the reported results, we used the label "Synergy" to reflect the outcomes obtained using the proposed pipeline (outlined in Section 4.2). Instead, the results referred to as "Naive approach" represent those from the simpler approach. For all metrics, the proposed pipeline provides better results compared to the more intuitive approach, which in some cases performs worse than the individual tractograms.

conventional techniques. Moreover, varying the parameter settings of the algorithms included in the synergy construction may help identify configurations that optimise accuracy and applicability for specific research or clinical contexts.

Finally, since the present evaluation was conducted on the high-quality HCP dataset, future studies will apply the proposed approach to clinical-like data. These images are typically acquired with less advanced protocols, leading to lower resolution, reduced SNR, and fewer diffusion directions. Such conditions will provide a more realistic context in which to assess the practical benefits of the synergy tractogram.

4.4 Conclusion

In this work, we addressed the challenge of anatomical variability in tractography arising from algorithm- and parameter- dependency. We proposed a novel approach that integrates information from different tracking algorithms, which, working in synergy, improve the accuracy and robustness of the final WM reconstructions. This method leverages the advanced filtering capabilities of COMMIT extensions to refine the combined tractogram and provide reliable quantitative estimates of structural connectivity. Validation experiments demonstrated enhanced accuracy, characterized by a notable improvement in all the considered metrics when employing the proposed synergy tractogram compared to standard reconstruction techniques. In vivo analyses further confirmed the increased robustness of the synergy tractogram to both intra-subject and inter-scan variability, yielding a more consistent representation of the underlying WM organisation. Overall, our findings indicate that the proposed method provides an effective and solid strategy for mitigating algorithmic bias and improving reproducibility in dMRI tractography. By integrating complementary information across algorithms, this approach presents a promising foundation for future methodological refinements and for applications in both research and clinical settings.

Chapter 5

Emerging research directions from this thesis

The blurred streamlines representation, beyond the benefits discussed in Chapter 3, allows the development of novel methods that are particularly valuable for real-world applications. By leveraging the substantial reduction in the number of streamlines required when using the blur, it becomes feasible to implement more advanced techniques that overcome some of the limitations of microstructure informed tractography (Section 2.4.2). As a result, these methods enable a more accurate estimation of brain structural connectivity, not only in healthy subjects, but also in cases of pathological conditions.

5.1 Adaptive tractography

Bundle-o-graphy (Battocchio et al., 2022) is a novel tractography method that combines the strengths of generative and discriminative strategies (see Section 2.3.2.4 for more details on the categories) to improve the anatomical accuracy of structural connectivity estimation. Starting from an input tractogram, the method introduces a *bundle-based representation* of the WM architecture, in which groups of coherent streamlines are modeled jointly rather than individually. As mentioned in Section 2.4.2, standard filtering approaches assume a static set of streamlines. In contrast, the bundles in

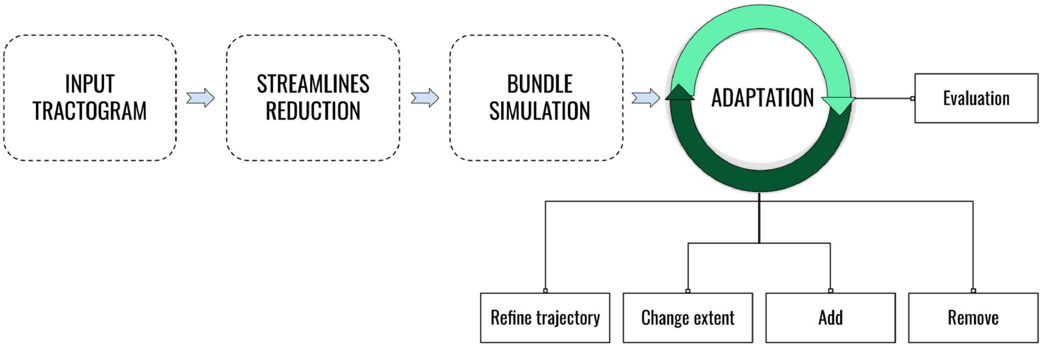

Figure 5.1: Schematic overview of Bundle-o-graphy. The method proceeds through hierarchical clustering and streamline simplification, the assignment of a volumetric extent via a blurring function, and a global optimization using a Markov-Chain Monte Carlo framework. From (Battocchio et al., 2022).

Bundle-o-graphy are not constrained to fixed trajectories: their position, shape, and extent can be iteratively adapted to better fit the measured diffusion signal (Battocchio et al., 2022). This adaptive capability is made computationally feasible by the *blurred streamlines representation*, which drastically reduces the number of parameters to optimize.

In more detail, Bundle-o-graphy proceeds in three main stages, as shown in Figure 5.1. First, redundant streamlines are reduced through hierarchical clustering, keeping only a few representative trajectories for each connection between GM regions. Each retained streamline is then *simplified* using spline interpolation to minimize the number of control points required for its description, resulting in a compact yet anatomically consistent set of candidate pathways.

In the second step, the blurred representation plays a central role in modeling the bundles. Each simplified streamline is assigned a volumetric extent by means of a *blurring function*, a concept that directly stems from the blurred streamlines representation introduced in Chapter 3. This blurring represents each streamline as the centroid of a cylindrical volume whose signal contribution decreases radially following a Gaussian profile (Figure 5.2). The resulting blurred bundles effectively capture the spatial uncertainty at bundle boundaries and mimic the contribution of groups of aligned fascicles, without

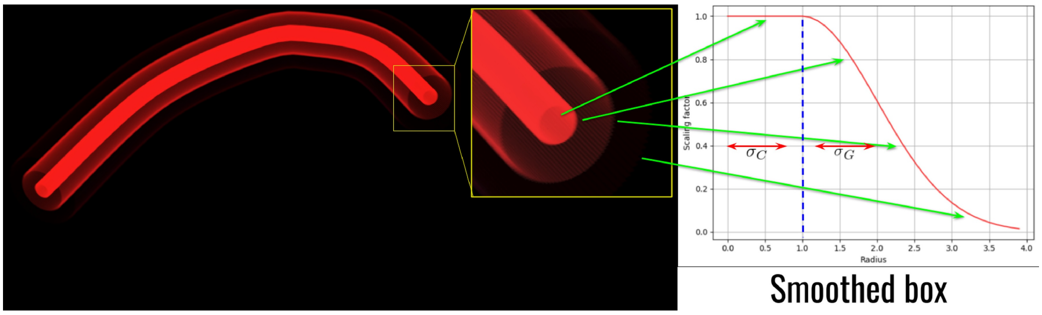

Figure 5.2: Volumetric modeling of bundles in Bundle-o-graphy. Each simplified streamline acts as the centroid of a tubular structure whose contribution to the diffusion signal decreases radially following a Gaussian profile. Replicas are distributed on concentric circles around each point of the fiber. From (Battocchio et al., 2022).

the need to explicitly track multiple neighboring streamlines. This volumetric modeling not only provides a biologically more plausible representation of WM pathways but also reduces the sensitivity to local tractography noise and seeding variability. With respect to the final version of the blurred streamlines detailed in Section 3.2.2, in Bundle-o-graphy, the replicas of the centroid are not displaced according to a Cartesian grid. Instead, they are distributed equidistantly over concentric circles of increasing radius (up to r) centered around each point of the fiber. The circle discretization, i.e., the number of replicas created and the number of circles used to sample the space, is empirically fixed. Instead, the scaling factor used for computing the signal contribution is the same as that in Eq. 3.2, accounting for both core and Gaussian regions.

Finally, the bundle configuration is *optimized globally* within a Bayesian framework. Using a Markov-Chain Monte Carlo (MCMC) sampling strategy combined with simulated annealing, both the trajectory and the blur extent of each bundle are iteratively updated to maximize agreement between the predicted and measured diffusion signals. The likelihood term is evaluated through the COMMIT forward model, which quantifies the contribution of each bundle to the observed signal, while prior terms regularize the overall number of bundles and connections. At each iteration, different types of moves are proposed, such as adding or removing a connection, refining the trajectory of a bundle, or changing its blur extent, thereby allowing the algorithm to explore a wide range of possible configurations while progressively converging toward the most plausible global solution.

The introduction of the blurred representation was crucial in making this adaptive formulation computationally tractable. By grouping multiple streamlines into a single blurred bundle, the parameter space is drastically reduced by nearly two orders of magnitude compared with traditional tractography, making MCMC optimization feasible. This *reduction in complexity* enabled the implementation of Bundle-o-graphy, which successfully demonstrates how a global, adaptive framework can improve the accuracy of tractography reconstructions. By jointly optimizing the geometry and microstructural contribution of bundles, this method achieves higher WM coverage, reduces the number of FP connections, and produces more anatomically consistent connectivity estimates across different tractography algorithms and datasets (Battocchio et al., 2022). These results clearly highlight the advantages of combining generative and discriminative principles within a representation of the WM based on blurred bundles.

Although the formulation employed in Bundle-o-graphy was preliminary, it clearly demonstrated the *potential* of the blurred streamlines representation as a fundamental methodological component for the development of adaptive tractography approaches. By providing a compact and physically grounded way to characterize the collective contribution of neighboring fibers, the blurred streamlines representation makes possible a new class of methods capable of simultaneously refining the shape, position, and cross-sectional extent of WM bundles.

5.2 Modeling pathological conditions

Building upon the blurred streamlines representation introduced in Chapter 3, further methodological developments have explored how this formulation can enable the study of pathological conditions within the framework of microstructure informed tractography. As mentioned in Section 2.4.2, a key limitation of all existing techniques, including COMMIT (Daducci et al., 2015) and its extensions, lies in the assumption that each streamline represents a group of axons with *constant* microstructural properties along its path. This simplification is plausible in healthy WM, where tissue characteristics such as axonal density and myelination vary smoothly at the scale detectable by dMRI. However, in the presence of disease, this assumption no longer holds. Pathological alterations, whether localized or diffuse, introduce spatial heterogeneity in the acquired signal, violating the hypothesis of constant streamline contribution and ultimately leading to biases in the estimated connectivity (Bosticardo et al., 2025).

A recent work has highlighted the consequences of this limitation in the context of *focal lesions* (Bosticardo et al., 2025). When lesions are present, the mismatch between the measured and predicted signal in affected voxels can trigger global compensation mechanisms in the optimization process, altering the estimated weights of healthy bundles as well. This so-called "butterfly effect" (Bosticardo et al., 2025; Daducci and Schiavi, 2025) arises because traditional microstructure informed tractography methods minimize the total fitting error across all voxels, leading to spurious over- or under-estimation of connections throughout the whole network. To address this issue, Bosticardo et al. (2025) proposed a *multi-compartment model* that augments the COMMIT signal equation with an explicit compartment representing lesion-related signal loss. By decoupling the contributions of healthy fibers from those of damaged tissue, this model prevents error propagation (see Figure 5.3) and yields unbiased estimates of structural connectivity in the presence of focal pathology, such as multiple sclerosis.

However, this method relies on two conditions that are not always met: the input tractogram must contain streamlines passing through the lesions, and a mask indicating the lesion locations must be provided. Combining this model with the blurred streamlines representation could help mitigate the first constraint. Indeed, blurred streamlines contribute not only to the voxels they traverse but also to neighboring ones (depending on the chosen

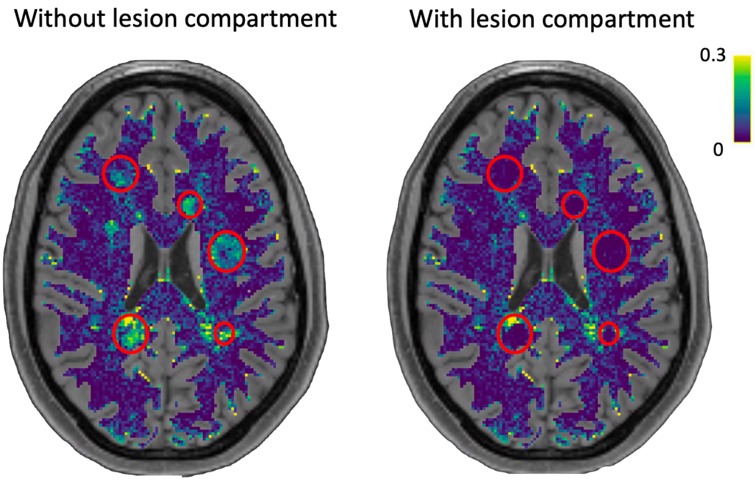

Figure 5.3: A comparison of fitting errors (root mean square error) obtained using the standard COMMIT formulation (left) and the multi-compartment model extension (right). The red circles clearly indicate a high error in the location of focal lesions, but a significant reduction when the pathology is modelled with the appropriate compartment. From (Bosticardo et al., 2025).

extent), potentially improving the coverage of focal lesions and leading to more accurate connectivity estimations. In this sense, the blurring acts as a spatial regularization mechanism that enhances the quality of the tractogram and, in turn, facilitates the distinction between lesions and partial volume effects.

While the multi-compartment formulation effectively handles localized lesions, it still assumes that streamline contributions remain constant outside those regions. This becomes a major limitation when modeling *diffuse axonal degeneration*, as observed in progressive neurodegenerative conditions or in the normal aging process, where microstructural deterioration occurs gradually along the tracts rather than being confined to well-defined lesions. In such cases, the contribution of each streamline to the diffusion signal may vary along its trajectory, reflecting the underlying gradient of tissue integrity.

To capture these spatially varying effects, we are working on a new method called $COMMIT_{pro}$ (Mari et al., 2025). This extension of the COMMIT framework allows the streamline contribution to vary along its path using

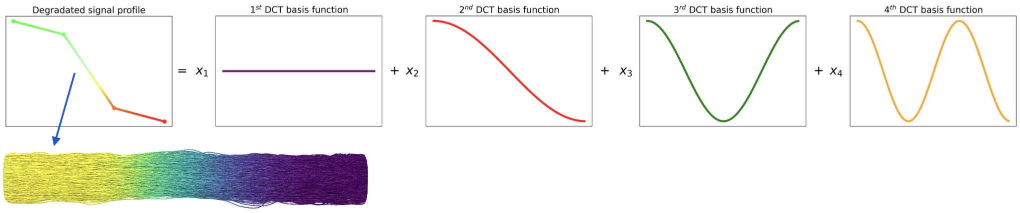

Figure 5.4: Example of a signal affected by degeneration. The image at the bottom shows a bundle of streamlines colored according to the simulated degeneration profile. The signal profile estimated by COMMIT$_{\text{pro}}$ is obtained by scaling each DCT basis function (here $N = 4$) by its corresponding coefficient x_i, thereby capturing the measured along-tract variation in signal intensity.

the Discrete Cosine Transform (DCT). Each streamline is represented as a weighted sum of cosine profiles, defined by a set of DCT basis functions oscillating at different frequencies, whose combination determines its signal contribution:

$$X_k = \sum_{n=0}^{N-1} x_n \cos\left[\frac{\pi}{n}\left(n+\frac{1}{2}\right)k\right] \quad \text{for } k = 0,\ 1,\ \ldots,\ N-1 \tag{5.1}$$

In this way, COMMIT$_{\text{pro}}$ can model both smooth and localized variations in axonal integrity along WM pathways.

Formally, the forward model is extended by representing every streamline with multiple columns in the linear operator $\mathbf{A}$ (Eq. 2.29). Each of these columns contains the potential signal contribution of that streamline, scaled along its trajectory according to one of the N DCT basis functions. As illustrated in Figure 5.4, the $\mathbf{x}$ coefficients estimated by COMMIT$_{\text{pro}}$ (N weights per streamline) are then combined to reconstruct the actual signal profile of the tract. A term for the weighted lasso regularization is added to the original COMMIT cost function (Eq. 2.30) in order to favor low-frequency components, promoting smooth, physiologically plausible profiles while avoiding overfitting.

The practical feasibility of this formulation depends on an efficient representation of the tractogram. Without controlling for redundancy, the number of columns in the operator $\mathbf{A}$ would grow prohibitively large, leading to excessive memory usage and unstable results. This issue is effectively mitigated by adopting the *blurred streamlines representation* introduced in Chapter 3, which enables the reduction of redundant streamlines and the compact modeling of fiber bundles. By leveraging this representation, $\text{COMMIT}_{\text{pro}}$ can maintain computational efficiency while employing a richer, position-dependent signal model.

We tested the proposed approach on synthetic data from the ISBI2013 phantom (Caruyer et al., 2014), simulating a realistic WM architecture that connects 53 GM regions through 27 bundles. Controlled signal degradations, both linear, Gaussian, and sigmoid, were applied along selected tracts to simulate different patterns of diffuse degeneration. As indicated in Figure 5.5, results showed that using $N = 5$ DCT basis functions achieved an optimal balance between model flexibility and stability. $\text{COMMIT}_{\text{pro}}$ accurately reconstructed the spatial profiles of degradation while preserving the contributions of unaffected bundles, confirming its ability to disentangle healthy and damaged pathways in a unified optimization framework. To fully assess its applicability, additional evaluations should be conducted across a wider range of conditions, including real in vivo data from patients with WM pathology manifesting through diffuse signal alterations along specific tracts. Achieving this also requires handling FP connections, which is possible by combining $\text{COMMIT}_{\text{pro}}$ with the group-lasso regularization introduced in COMMIT2 (see Section 2.4.1.4).

Taken together, the multi-compartment model (Bosticardo et al., 2025) and $\text{COMMIT}_{\text{pro}}$ (Mari et al., 2025) represent two complementary extensions of microstructure informed tractography for modeling *pathological conditions*. The former explicitly accounts for focal lesions through an additional signal compartment, while the latter introduces position-dependent streamline contributions to describe diffuse axonal degeneration. Both developments benefit from the blurred streamlines representation, which provides the necessary efficiency and stability to support more realistic models of WM connectivity in health and disease.

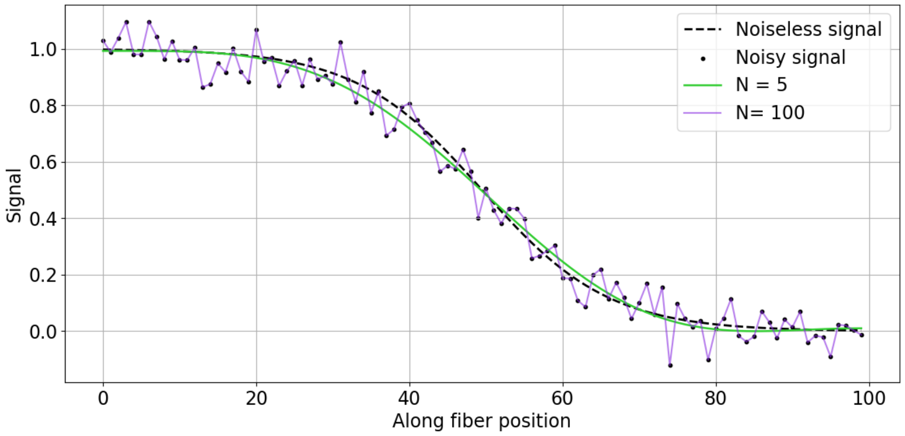

Figure 5.5: Reconstruction of along-tract signal profiles using Discrete Cosine Transform (DCT) coefficients in $\text{COMMIT}_{\text{pro}}$. The noiseless reference profile (dashed black line), noisy signal samples (black dots), and reconstructions obtained with 5 (green) and 100 (purple) DCT basis functions are shown. A small number of basis functions can accurately reproduce smooth signal variations along a streamline, whereas increasing their number also captures the high-frequency variations associated with noise. From (Mari et al., 2025)

Chapter 6

Conclusion

In recent years, dMRI has become an essential tool to non-invasively investigate the structural organization of the human brain and its role in connectivity. Through *tractography*, WM pathways of fiber bundles can be inferred from the directional information encoded in the diffusion signal, enabling unprecedented *in vivo* exploration of the brain architecture. Despite its widespread use, tractography remains an indirect and model-dependent technique: it relies on estimated fiber orientations rather than directly visualizing axons, making it sensitive to noise, algorithmic choices, and acquisition parameters. As a consequence, tractograms often suffer from a lack of biological specificity, large redundancy, and a limited quantitative relationship to the underlying tissue microstructure. These limitations affect the anatomical accuracy and interpretability of tractography-derived estimates in both healthy and pathological conditions.

To address these challenges, research has increasingly shifted toward *microstructure informed tractography*, such as the COMMIT framework, which combines the reconstructed tractogram with biophysical signal models to assign each streamline a quantitatively meaningful contribution to the measured diffusion signal. Although these advances represent a major step forward, they also highlight the need for more compact methods that directly link streamline geometry to the local diffusion signal in a consistent and efficient manner. The *primary goal* of my PhD thesis was to contribute to this effort by developing, validating, and applying the blurred streamlines representation, a new approach that redefines how tractography reconstructions are modeled and used to estimate how different brain regions are structurally connected to one another.

The first part of the thesis (Chapter 3) introduced the *blurred streamlines representation*, the central methodological contribution of this work. Traditional tractography encodes WM pathways as simple polylines in 3D space, and to increase the chances of reconstructing all the true positive connections, a very large number of streamlines is typically generated. This results in high redundancy and introduces biases in the final quantitative estimates. The proposed representation overcomes these issues by replacing clusters of redundant streamlines with the centroid of a spatially extended volume whose contribution to the diffusion signal decreases radially according to a blurring function. This formulation provides a compact yet physically grounded description of WM architecture, drastically reducing redundancy while preserving anatomical detail. Comprehensive evaluations on synthetic and in vivo datasets demonstrated that blurred streamlines improve numerical stability and reduce sensitivity to input data variability, maintaining the same accuracy as state-of-the-art methods. In addition, by employing less than 10% of the input streamlines, they significantly decrease the computational complexity of algorithms that process tractography reconstructions and the storage requirements of the resulting tractograms.

Leveraging this representation, Chapter 4 presents a new approach that utilizes the blurred streamlines to enable tractograms generated using different tracking algorithms to work in *synergy*, thereby mitigating their limitations. Because methodological and parameter choices in the processing pipeline introduce substantial variability in the resulting tractograms, combining complementary reconstructions helps reduce algorithm-specific biases. The proposed method produces a unified tractogram with improved anatomical plausibility, greater robustness, and higher intra-subject consistency than any individual reconstruction, highlighting the value of aggregation-based strategies for enhancing the reliability of brain tractography and, consequently, structural connectivity maps.

The flexibility and computational efficiency of the blurred streamlines representation also enabled the investigation of more *advanced developments* (Chapter 5). In the Bundle-o-graphy framework, the blur was used to make global tractography computationally feasible by modeling coherent fiber groups as non-static bundles. This reduced the dimensionality of the parameter space by orders of magnitude and allowed for the joint optimization of bundle geometry and microstructural contributions within a Bayesian formulation, demonstrating the potential of adaptive global tractography. Finally, Section 5.2 extended the use of the blurred streamlines representation to the modeling of pathological conditions within microstructure informed tractography. Standard approaches assume that the signal contribution of a streamline remains constant along its trajectory. A multi-compartment extension of COMMIT was recently proposed to overcome this strong assumption in focal lesions by introducing an explicit compartment for modeling related signal loss. In contrast, to capture diffuse axonal degeneration along specific tracts, we are developing a new formulation that introduces position-dependent streamline contributions using the DCT formalism, enabling the modeling of smooth signal variations along WM pathways.Preliminary experiments on synthetic data confirmed the potential of this method for characterizing diffuse pathological alterations. Both approaches benefited from the blurred streamlines representation, which improved spatial coverage in lesioned areas, stabilized the optimization, and ensured computational tractability even when multiple signal components were estimated per streamline.

Overall, this thesis addressed key limitations of tractography by introducing a compact and physically grounded framework that enhances robustness, interpretability, and computational efficiency. The blurred streamlines representation provides a powerful foundation for reducing redundancy, enhancing numerical formulation, and enabling new methodological developments in both healthy and pathological contexts. Future research will focus on extending these techniques to larger cohorts and clinical populations, integrating additional microstructure models, and exploring longitudinal applications to investigate disease progression.

Publications

Journal papers

- **Ilaria Gabusi**, Matteo Battocchio, Sara Bosticardo, Simona Schiavi, and Alessandro Daducci. **Blurred streamlines: a novel representation to reduce redundancy in tractography**. *Medical Image Analysis*, 2024, DOI: 10.1016/j.media.2024.103101.

  This study proposes a novel streamline representation that reduces redundancy in tractograms while preserving anatomical information, enabling more compact and robust analyses. It constitutes the methodological foundation of this thesis and provides a practical tool for improving efficiency and usability of tractography.

- **Ilaria Gabusi**, Giulia Biolo, Matteo Battocchio, Sara Bosticardo, and Alessandro Daducci. **Improving the anatomical accuracy of tractography by leveraging the unique strengths of different algorithms**. *Medical Image Analysis*, under review.

  This work introduces the synergy-based tractography approach that combines complementary reconstruction strategies to reduce algorithm-specific biases and improve anatomical plausibility. It represents the second methodological advancement of this thesis and a direct application of the blurred streamlines, leveraging the substantial redundancy reduction enabled by that representation.

- G Girard, J Rafael-Patino, R Truffet, D Baran Aydogan, N Adluru, V A Nair, V Prabhakaran, B B Bendlin, A L Alexander, S Bosticardo, **I**

Gabusi, M Ocampo-Pineda, M Battocchio, Z Piskorova, P Bontempi, S Schiavi, A Daducci, A Stafiej, D Ciupek, F Bogusz, T Pieciak, M Frigo, S Sedlar, S Deslauriers-Gauthier, I Kojcic, M Zucchelli, H Laghrissi, Y Ji, R Deriche, K G Schilling, B A Landman, A Cacciola, G A Basile, S Bertino, N Newlin, P Kanakaraj, F Rheault, P Filipiak, T Shepherd, Y C Lin, D G Placantonakis, F E Boada, S H Baete, E Hernández-Gutiérrez, A Ramírez-Manzanares, R Coronado-Leija, P Stack-Sánchez, L Concha, M Descoteaux, S Mansour L, C Seguin, A Zalesky, K Marshall, E J Canales-Rodríguez, Y Wu, S Ahmad, P T Yap, A Théberge, F Gagnon, F Massi, J L Villarreal Haro, M Pizzolato, E Caruyer, and J P Thiran. **Tractography passes the test: Results from the diffusion-simulated connectivity (disco) challenge**. *NeuroImage*, 2023, DOI: 10.1016/j.neuroimage.2023.120231.

  This international challenge benchmarked tractography pipelines using diffusion-simulated ground-truth data. I participated in the challenge together with colleagues from the DICE (Diffusion Imaging and Connectivity Estimation) lab, and our team ranked third overall.

- Alessandra Scaravilli, **Ilaria Gabusi**, Gaia Mari, Matteo Battocchio, Sara Bosticardo, Simona Schiavi, Benjamin Bender, Christoph Kessler, Bernard Brais, Roberta La Piana, Bart P. van de Warrenburg, Mirco Cosottini, Dagmar Timmann, PROSPAX Consortium, Alessandro Daducci, Rebecca Schüle, Matthis Synofzik, Filippo Maria Santorelli, and Sirio Cocozza. **An MRI evaluation of white matter involvement in paradigmatic forms of spastic ataxia: results from the multi-center PROSPAX study**. *Journal of Neurology*, 2024, DOI: 10.1007/s00415-024-12505-y.

  This work investigates white matter alterations across different forms of spastic ataxia within a multicenter study on these rare disorders. My contribution focused on the processing and quantitative analysis of diffusion MRI data, in accordance with the clinical hypotheses.

- Alessandra Scaravilli, Gaia Mari, **Ilaria Gabusi**, Matteo Battocchio, Sara Bosticardo, Simona Schiavi, Benjamin Bender, Christoph Kessler, Bernard Brais, Roberta La Piana, Bart P. van de Warrenburg, Mirco Cosottini, Dagmar Timmann, PROSPAX Consortium, Alessandro Daducci, Rebecca Schüle, Matthis Synofzik, Filippo Maria Santorelli, and Sirio Cocozza. **An Investigation of Corticospinal Tract Microstructural Integrity in ARSACS Using a Profilometry MRI Analysis: Results From the PROSPAX Study**. *European Journal of Neurology*, 2025, DOI: 10.1111/ene.70128.

This study extends the previous publication using the same multicenter dataset and focuses on tract-specific profiling of the corticospinal tract in ARSACS patients. I contributed to the diffusion MRI processing and to the tract-specific microstructural analysis.

Conference abstracts

- **Ilaria Gabusi**, Matteo Battocchio, Sara Bosticardo, Simona Schiavi, and Alessandro Daducci. **Reducing redundancy in tractography using blurred streamlines**. *ISMRM Workshop on Diffusion MRI: From Research to Clinic*, 2022

- **Ilaria Gabusi**, Matteo Battocchio, Sara Bosticardo, Simona Schiavi, and Alessandro Daducci. **A novel streamline representation to reduce redundancy in tractography**. *International Society for Magnetic Resonance in Medicine (ISMRM) annual meeting*, 2023

- **Ilaria Gabusi**, Alessandra Scaravilli, Gaia Mari, Matteo Battocchio, Sara Bosticardo, Simona Schiavi, Benjamin Bender, Christoph Kessler, Bernard Brais, Roberta La Piana, Bart P. van de Warrenburg, Mirco Cosottini, Dagmar Timmann, PROSPAX Consortium, Alessandro Daducci, Rebecca Schüle, Matthis Synofzik, Filippo Maria Santorelli, and Sirio Cocozza. **MRI analysis of white matter in spastic ataxia: insights from the PROSPAX cohort**. *BraYn - 7th Brainstorming Research Assembly for Young Neuroscientists*, 2024

- **Ilaria Gabusi**, Giulia Biolo, Matteo Battocchio, and Alessandro Daducci. **Consensus tractography: decreasing algorithm dependency for improved fiber reconstructions**. *ISMRM Workshop on 40 years of Diffusion: Past, Present & Future Perspectives*, 2025

- **Ilaria Gabusi**, Giulia Biolo, Matteo Battocchio, and Alessandro Daducci. **Consensus tractography: decreasing algorithm dependency to improve fiber reconstructions**. *International Society for Magnetic Resonance in Medicine (ISMRM) annual meeting*, 2025

- Alessandra Scaravilli, **Ilaria Gabusi**, Gaia Mari, Matteo Battocchio, Sara Bosticardo, Simona Schiavi, Benjamin Bender, Christoph Kessler, Bernard Brais, Roberta La Piana, Bart P. van de Warrenburg, Mirco Cosottini, Dagmar Timmann, PROSPAX Consortium, Alessandro Daducci, Rebecca Schüle, Matthis Synofzik, Filippo Maria Santorelli, and Sirio Cocozza. **An investigation of white matter involvement in paradigmatic forms of spastic ataxia: results from the international PROSPAX study**. *International Congress for Ataxia Research*, 2024

- Alessandra Scaravilli, Gaia Mari, **Ilaria Gabusi**, Matteo Battocchio, Sara Bosticardo, Simona Schiavi, Benjamin Bender, Christoph Kessler, Roberta La Piana, Bart P. van de Warrenburg, Mirco Cosottini, Dagmar Timmann, PROSPAX Consortium, Alessandro Daducci, Rebecca Schüle, Matthis Synofzik, Filippo Maria Santorelli, and Sirio Cocozza. **Microstructural damage of the corticospinal tract in ARSACS: results of a profilometry analysis of data collected within the PROSPAX study**. *International Congress for Ataxia Research*, 2024

- Gaia Mari, Alessandra Scaravilli, **Ilaria Gabusi**, Matteo Battocchio, Sara Bosticardo, Simona Schiavi, Benjamin Bender, Christoph Kessler, Roberta La Piana, Bart P. van de Warrenburg, Mirco Cosottini, Dagmar Timmann, PROSPAX Consortium, Alessandro Daducci, Rebecca Schüle, Matthis Synofzik, Filippo Maria Santorelli, and Sirio Cocozza. **Microstructural Changes and Damage in ARSACS Corticospinal**

Tracts: PROSPAX Cohort Insights. *BraYn - 7th Brainstorming Research Assembly for Young Neuroscientists*, 2024

- Gaia Mari, Matteo Battocchio, Sara Bosticardo, **Ilaria Gabusi**, and Alessandro Daducci. **Accurate modeling of diffuse axonal fiber degeneration with the Discrete Cosine Transform**. *ISMRM Workshop on 40 years of Diffusion: Past, Present & Future Perspectives*, 2025

- Gaia Mari, Matteo Battocchio, Sara Bosticardo, **Ilaria Gabusi**, and Alessandro Daducci. **COMMITpro: accurate modeling of diffuse axonal fiber degeneration using the Discrete Cosine Transform**. *International Society for Magnetic Resonance in Medicine (ISMRM) annual meeting*, 2025

Bibliography

Alexander, A. L., J. E. Lee, M. Lazar, and A. S. Field (2007). "Diffusion tensor imaging of the brain". In: *Neurotherapeutics* 4.3, pp. 316–329. DOI: `10.1016/j.nurt.2007.05.011`.

Alexander, D. C., T. B. Dyrby, M. Nilsson, and H. Zhang (2019). "Imaging brain microstructure with diffusion MRI: practicality and applications". In: *NMR in Biomedicine* 32.4. e3841 NBM-16-0261.R1, e3841. DOI: `10.1002/nbm.3841`.

Assaf, Y. and P. J. Basser (2005). "Composite hindered and restricted model of diffusion (CHARMED) MR imaging of the human brain". In: *NeuroImage* 27.1, pp. 48–58. DOI: `10.1016/j.neuroimage.2005.03.042`.

Assaf, Y., T. Blumenfeld-Katzir, Y. Yovel, and P. J. Basser (2008). "Axcaliber: A method for measuring axon diameter distribution from diffusion MRI". In: *Magnetic Resonance in Medicine* 59.6, pp. 1347–1354. DOI: `10.1002/mrm.21577`.

Aydogan, D. B. (2022). "Fiber coupling (FICO) measure using anisotropic smoothing of track orientation density images for tractogram filtering". In: *International Society of Magnetic Resonance in Medicine (ISMRM)*.

Aydogan, D. B. and Y. Shi (2021). "Parallel Transport Tractography". In: *IEEE Transactions on Medical Imaging* 40.2, pp. 635–647. DOI: `10.1109/TMI.2020.3034038`.

Barakovic, M., G. Girard, S. Schiavi, D. Romascano, M. Descoteaux, C. Granziera, D. K. Jones, G. M. Innocenti, J.-P. Thiran, and A. Daducci (2021a). "Bundle-Specific Axon Diameter Index as a New Contrast to

Differentiate White Matter Tracts”. In: *Frontiers in Neuroscience* Volume 15 - 2021. DOI: 10.3389/fnins.2021.646034.

Barakovic, M., C. M. Tax, U. Rudrapatna, M. Chamberland, J. Rafael-Patino, C. Granziera, J.-P. Thiran, A. Daducci, E. J. Canales-Rodríguez, and D. K. Jones (2021b). “Resolving bundle-specific intra-axonal T2 values within a voxel using diffusion-relaxation tract-based estimation”. In: *NeuroImage* 227, p. 117617. DOI: 10.1016/j.neuroimage.2020.117617.

Basser, P., J. Mattiello, and D. Lebihan (1994a). “Estimation of the Effective Self-Diffusion Tensor from the NMR Spin Echo”. In: *Journal of Magnetic Resonance, Series B* 103.3, pp. 247–254. DOI: 10.1006/jmrb.1994.1037.

Basser, P. J. and E. Özarslan (2009). “Chapter 1 - Introduction to Diffusion MR”. In: *Diffusion MRI*. Ed. by H. Johansen-Berg and T. E. Behrens. San Diego: Academic Press, pp. 2–10. DOI: 10.1016/B978-0-12-374709-9.00001-8.

Basser, P. J., S. Pajevic, C. Pierpaoli, J. Duda, and A. Aldroubi (2000). “In vivo fiber tractography using DT-MRI data”. In: *Magnetic Resonance in Medicine* 44.4, pp. 625–632. DOI: 10.1002/1522-2594(200010)44:4<625::AID-MRM17>3.0.CO;2-O.

Basser, P. J. and C. Pierpaoli (1996). “Microstructural and Physiological Features of Tissues Elucidated by Quantitative-Diffusion-Tensor MRI”. In: *Journal of Magnetic Resonance, Series B* 111.3, pp. 209–219. DOI: 10.1006/jmrb.1996.0086.

Basser, P., J. Mattiello, and D. LeBihan (1994b). “MR diffusion tensor spectroscopy and imaging”. In: *Biophysical journal* 66.1, pp. 259–267. DOI: 10.1016/s0006-3495(94)80775-1.

Bassett, D. S. and M. S. Gazzaniga (2011). “Understanding complexity in the human brain”. In: *Trends in Cognitive Sciences* 15.5, pp. 200–209. DOI: 10.1016/j.tics.2011.03.006.

Bastiani, M., N. J. Shah, R. Goebel, and A. Roebroeck (2012). “Human cortical connectome reconstruction from diffusion weighted MRI: The effect of tractography algorithm”. In: *NeuroImage* 62.3, pp. 1732–1749. DOI: 10.1016/j.neuroimage.2012.06.002.

Battocchio, M., S. Schiavi, M. Descoteaux, and A. Daducci (2022). "Bundle-o-graphy: improving structural connectivity estimation with adaptive microstructure-informed tractography". In: *NeuroImage* 263, p. 119600. DOI: `10.1016/j.neuroimage.2022.119600`.

Behrens, T., H. J. Berg, S. Jbabdi, M. Rushworth, and M. Woolrich (2007). "Probabilistic diffusion tractography with multiple fibre orientations: What can we gain?" In: *NeuroImage* 34.1, pp. 144–155. DOI: `10.1016/j.neuroimage.2006.09.018`.

Behrens, T., M. Woolrich, M. Jenkinson, H. Johansen-Berg, R. Nunes, S. Clare, P. Matthews, J. Brady, and S. Smith (2003). "Characterization and propagation of uncertainty in diffusion-weighted MR imaging". In: *Magnetic Resonance in Medicine* 50.5, pp. 1077–1088. DOI: `10.1002/mrm.10609`.

Belaroussi, B., J. Milles, S. Carme, Y. M. Zhu, and H. Benoit-Cattin (2006). "Intensity non-uniformity correction in MRI: Existing methods and their validation". In: *Medical Image Analysis* 10.2, pp. 234–246. DOI: `10.1016/j.media.2005.09.004`.

Bells, S., M. Cercignani, S. Deoni, Y. Assaf, O. Pasternak, C. J. Evans, A. Leemans, and D. K. Jones (2011). ""Tractometry" – comprehensive multi-modal quantitative assessment of white matter along specific tracts". In: *Proceedings of the International Society for Magnetic Resonance in Medicine*.

Belsley, D., E. Kuh, and R. Welsch (1980). *Regression Diagnostics: Identifying Influential Data and Sources of Collinearity*. Wiley Series in Probability and Statistics. Wiley.

Berger, A. (2002). "Magnetic resonance imaging". In: *BMJ* 324.7328, p. 35. DOI: `10.1136/bmj.324.7328.35`.

Bihan, D. L., R. Turner, and P. Douek (1993). "Is water diffusion restricted in human brain white matter? An echo-planar NMR imaging study". In: *NeuroReport* 4.7.

Bitar, R., G. Leung, R. Perng, S. Tadros, A. R. Moody, J. Sarrazin, C. McGregor, M. Christakis, S. Symons, A. Nelson, and T. P. Roberts (2006). "MR Pulse Sequences: What Every Radiologist Wants to Know but Is

Afraid to Ask". In: *RadioGraphics* 26.2. PMID: 16549614, pp. 513–537. DOI: 10.1148/rg.262055063.

Bosticardo, S., M. Battocchio, S. Schiavi, A. Zalesky, C. Granziera, and A. Daducci (2025). "A multi-compartment model for pathological connectomes". In: *Network Neuroscience*, pp. 1–19. DOI: 10.1162/netn.a.30.

Bullmore, E. and O. Sporns (2009). "Complex brain networks: graph theoretical analysis of structural and functional systems". In: *Nature Reviews Neuroscience* 10.3, pp. 186–198.

Bullmore, E. and O. Sporns (2012). "The economy of brain network organization". In: *Nature Reviews Neuroscience* 13.5, pp. 336–349. DOI: 10.1038/nrn3214.

Bullmore, E. T. and D. S. Bassett (2011). "Brain Graphs: Graphical Models of the Human Brain Connectome". In: *Annual Review of Clinical Psychology* 7.Volume 7, 2011, pp. 113–140. DOI: 10.1146/annurev-clinpsy-040510-143934.

Caan, M. W. A. (2016). "DTI Analysis Methods: Fibre Tracking and Connectivity". In: *Diffusion Tensor Imaging: A Practical Handbook*. Ed. by W. Van Hecke, L. Emsell, and S. Sunaert. New York, NY: Springer New York, pp. 205–228. DOI: 10.1007/978-1-4939-3118-7_11.

Callaghan, P. T., C. D. Eccles, and Y. Xia (1988). "NMR microscopy of dynamic displacements: k-space and q-space imaging". In: *Journal of Physics E: Scientific Instruments* 21.8, p. 820. DOI: 10.1088/0022-3735/21/8/017.

Callaghan, P. (1996). "NMR imaging, NMR diffraction and applications of pulsed gradient spin echoes in porous media". In: *Magnetic Resonance Imaging* 14.7. Proceedings of the Third International Meeting on Recent Advances in MR Applications to Porous Media, pp. 701–709. DOI: 10.1016/S0730-725X(96)00152-X.

Cammoun, L., X. Gigandet, D. Meskaldji, J. P. Thiran, O. Sporns, K. Q. Do, P. Maeder, R. Meuli, and P. Hagmann (2012). "Mapping the human connectome at multiple scales with diffusion spectrum MRI". In: *Journal of Neuroscience Methods* 203.2, pp. 386–397. DOI: 10.1016/j.jneumeth.2011.09.031.

Caruyer, E., A. Daducci, M. Descoteaux, J.-C. Houde, J.-P. Thiran, and R. Verma (2014). “Phantomas: a flexible software library to simulate diffusion MR phantoms”. In: *International Society of Magnetic Resonance in Medicine (ISMRM)*.

Catani, M. (2025). “Chapter 1 - The brain and its pathways”. In: *Handbook of Diffusion MR Tractography*. Ed. by F. Dell’Acqua, M. Descoteaux, and A. Leemans. Academic Press, pp. 3–18. DOI: 10.1016/B978-0-12-818894-1.00034-3.

Catani, M. and M. Thiebaut de Schotten (2012). *Atlas of Human Brain Connections*. Oxford University Press. DOI: 10.1093/med/9780199541164.001.0001.

Colby, J. B., L. Soderberg, C. Lebel, I. D. Dinov, P. M. Thompson, and E. R. Sowell (2012). “Along-tract statistics allow for enhanced tractography analysis”. In: *NeuroImage* 59.4, pp. 3227–3242. DOI: 10.1016/j.neuroimage.2011.11.004.

Colom, R., S. Karama, R. E. Jung, and R. J. Haier (2010). “Human intelligence and brain networks”. In: *Dialogues in Clinical Neuroscience* 12.4. PMID: 21319494, pp. 489–501. DOI: 10.31887/DCNS.2010.12.4/rcolom.

Conturo, T. E., N. F. Lori, T. S. Cull, E. Akbudak, A. Z. Snyder, J. S. Shimony, R. C. McKinstry, H. Burton, and M. E. Raichle (1999). “Tracking neuronal fiber pathways in the living human brain”. In: *Proceedings of the National Academy of Sciences* 96.18, pp. 10422–10427. DOI: 10.1073/pnas.96.18.10422.

Côté, M.-A., E. Garyfallidis, H. Larochelle, and M. Descoteaux (2015). “Cleaning up the mess: tractography outlier removal using hierarchical QuickBundles clustering”. In: *International Society of Magnetic Resonance in Medicine (ISMRM)*.

Daducci, A., A. Dal Palù, A. Lemkaddem, and J. Thiran (2013). “A convex optimization framework for global tractography”. In: *2013 IEEE 10th International Symposium on Biomedical Imaging*, pp. 524–527. DOI: 10.1109/ISBI.2013.6556527.

Daducci, A., A. Dal Palù, A. Lemkaddem, and J. Thiran (2015). “COMMIT: Convex Optimization Modeling for Microstructure Informed Tractography”.

In: *IEEE Transactions on Medical Imaging* 34.1, pp. 246–257. DOI: 10.1109/TMI.2014.2352414.

Daducci, A., A. Dal Palú, M. Descoteaux, and J.-P. Thiran (2016). "Microstructure Informed Tractography: Pitfalls and Open Challenges". In: *Frontiers in Neuroscience* 10. DOI: 10.3389/fnins.2016.00247.

Daducci, A. and S. Schiavi (2025). "Quantitative tractography: joys and sorrows". In: *Brain Structure and Function* 230.6, p. 88. DOI: 10.1007/s00429-025-02939-z.

Daducci, A., S. Schiavi, D. Christiaens, R. Smith, and D. C. Alexander (2025). "Chapter 16 - Global tractography". In: *Handbook of Diffusion MR Tractography*. Ed. by F. Dell'Acqua, M. Descoteaux, and A. Leemans. Academic Press, pp. 297–314. DOI: 10.1016/B978-0-12-818894-1.00014-8.

Dell'Acqua, F., M. Descoteaux, and A. Leemans, eds. (2025). *Handbook of Diffusion MR Tractography*. Academic Press.

Dell'Acqua, F. and J.-D. Tournier (2019). "Modelling white matter with spherical deconvolution: How and why?" In: *NMR in Biomedicine* 32.4. e3945 NBM-17-0226.R1, e3945. DOI: 10.1002/nbm.3945.

Dell'Acqua, F., A. Leemans, M. Dawson, and M. Descoteaux (2025). "Chapter 10 - Single-shell diffusion models: From DTI to HARDI". In: *Handbook of Diffusion MR Tractography*. Ed. by F. Dell'Acqua, M. Descoteaux, and A. Leemans. Academic Press, pp. 177–200. DOI: 10.1016/B978-0-12-818894-1.00010-0.

Descoteaux, M. (2008). "High angular resolution diffusion MRI: from local estimation to segmentation and tractography". PhD thesis. Nice: Université Nice Sophia Antipolis.

Descoteaux, M., R. Deriche, T. R. Knösche, and A. Anwander (2009). "Deterministic and probabilistic tractography based on complex fibre orientation distributions". en. In: *IEEE Trans. Med. Imaging* 28.2, pp. 269–286.

Desikan, R. S., F. Ségonne, B. Fischl, B. T. Quinn, B. C. Dickerson, D. Blacker, R. L. Buckner, A. M. Dale, R. P. Maguire, B. T. Hyman, M. S. Albert, and R. J. Killiany (2006). "An automated labeling system for subdividing the human cerebral cortex on MRI scans into gyral based regions of interest".

In: *NeuroImage* 31.3, pp. 968–980. DOI: `10.1016/j.neuroimage.2006.01.021`.

Destrieux, C., B. Fischl, A. Dale, and E. Halgren (2010). “Automatic parcellation of human cortical gyri and sulci using standard anatomical nomenclature”. In: *NeuroImage* 53.1, pp. 1–15. DOI: `10.1016/j.neuroimage.2010.06.010`.

Drakesmith, M., K. Caeyenberghs, A. Dutt, G. Lewis, A. David, and D. K. Jones (2015). “Overcoming the effects of false positives and threshold bias in graph theoretical analyses of neuroimaging data”. In: *NeuroImage* 118, pp. 313–333. DOI: `10.1016/j.neuroimage.2015.05.011`.

Dyrby, T. B., S. Sarubbo, F. Rheault, E. Fieremans, A. W. Anderson, M. Palombo, P. Neher, K. S. Rockland, and K. G. Schilling (2025). “Chapter 26 - Tractography validation Part 2: The use of anatomical model systems and measures for validation”. In: *Handbook of Diffusion MR Tractography.* Ed. by F. Dell’Acqua, M. Descoteaux, and A. Leemans. Academic Press, pp. 511–542. DOI: `10.1016/B978-0-12-818894-1.00020-3`.

Fan, L. (2021). “Mapping the human brain: what is the next frontier?” In: *The Innovation* 2.1. DOI: `10.1016/j.xinn.2020.100073`.

Fields, R. D. (2010). “Change in the Brain’s White Matter”. In: *Science* 330.6005, pp. 768–769. DOI: `10.1126/science.1199139`.

Fillard, P., C. Poupon, and J.-F. Mangin (2009). “A Novel Global Tractography Algorithm Based on an Adaptive Spin Glass Model”. In: *Medical Image Computing and Computer-Assisted Intervention – MICCAI 2009.* Ed. by G.-Z. Yang, D. Hawkes, D. Rueckert, A. Noble, and C. Taylor. Berlin, Heidelberg: Springer Berlin Heidelberg, pp. 927–934.

Fischl, B., D. H. Salat, E. Busa, M. Albert, M. Dieterich, C. Haselgrove, A. van der Kouwe, R. Killiany, D. Kennedy, S. Klaveness, A. Montillo, N. Makris, B. Rosen, and A. M. Dale (2002). “Whole Brain Segmentation: Automated Labeling of Neuroanatomical Structures in the Human Brain”. In: *Neuron* 33.3, pp. 341–355. DOI: `10.1016/S0896-6273(02)00569-X`.

Florack, L., R. Sengers, and A. Fuster (2025). “Chapter 15 - Geodesic tractography”. In: *Handbook of Diffusion MR Tractography.* Ed. by F. Dell’Acqua,

M. Descoteaux, and A. Leemans. Academic Press, pp. 275–295. DOI: 10.1016/B978-0-12-818894-1.00028-8.

Fornito, A., A. Zalesky, and E. Bullmore (2016). *Fundamentals of brain network analysis*. Academic press. DOI: 10.1016/C2012-0-06036-X.

Fürtjes, A. E., J. H. Cole, B. Couvy-Duchesne, and S. J. Ritchie (2023). "A quantified comparison of cortical atlases on the basis of trait morphometricity". In: *Cortex* 158, pp. 110–126. DOI: 10.1016/j.cortex.2022.11.001.

Gabusi, I., M. Battocchio, S. Bosticardo, S. Schiavi, and A. Daducci (2024). "Blurred streamlines: A novel representation to reduce redundancy in tractography". In: *Medical Image Analysis* 93, p. 103101. DOI: 10.1016/j.media.2024.103101.

Garyfallidis, E., M. Brett, M. M. Correia, G. B. Williams, and I. Nimmo-Smith (2012). "QuickBundles, a Method for Tractography Simplification". In: *Frontiers in Neuroscience* 6. DOI: 10.3389/fnins.2012.00175.

Garyfallidis, E., M.-A. Côté, F. Rheault, and M. Descoteaux (2016). "QuickBundlesX: Sequential clustering of millions of streamlines in multiple levels of detail at record execution time". In: *International Society of Magnetic Resonance in Medicine (ISMRM)*.

Gauvin, A. (2016). "Assurance qualité en dissection virtuelle des faisceaux de la matière blanche par tractographie". MA thesis. Sherbrooke, Québec, Canada: Universite de Sherbrooke.

Giannelli, M., M. Cosottini, M. C. Michelassi, G. Lazzarotti, G. Belmonte, C. Bartolozzi, and M. Lazzeri (2010). "Dependence of brain DTI maps of fractional anisotropy and mean diffusivity on the number of diffusion weighting directions". In: *Journal of Applied Clinical Medical Physics* 11.1, pp. 176–190. DOI: 10.1120/jacmp.v11i1.2927.

Girard, G., D. B. Aydogan, F. Dell'Acqua, A. Leemans, M. Descoteaux, and S. N. Sotiropoulos (2025). "Chapter 14 - Probabilistic tractography". In: *Handbook of Diffusion MR Tractography*. Ed. by F. Dell'Acqua, M. Descoteaux, and A. Leemans. Academic Press, pp. 257–274. DOI: 10.1016/B978-0-12-818894-1.00030-6.

Girard, G., R. Caminiti, A. Battaglia-Mayer, E. St-Onge, K. S. Ambrosen, S. F. Eskildsen, K. Krug, T. B. Dyrby, M. Descoteaux, J.-P. Thiran, and

G. M. Innocenti (2020). “On the cortical connectivity in the macaque brain: A comparison of diffusion tractography and histological tracing data”. In: *NeuroImage* 221, p. 117201. DOI: `10.1016/j.neuroimage.2020.117201`.

Girard, G., K. Whittingstall, R. Deriche, and M. Descoteaux (2014). “Towards quantitative connectivity analysis: reducing tractography biases”. In: *NeuroImage* 98, pp. 266–278. DOI: `10.1016/j.neuroimage.2014.04.074`.

Gray, H. and W. Lewis (1918). *Anatomy of the human body. Philadelphia: Lea & Febiger, 1918; Bartleby. com, 2000.*

Grebenkov, D. S. (2007). “NMR survey of reflected Brownian motion”. In: *Rev. Mod. Phys.* 79 (3), pp. 1077–1137. DOI: `10.1103/RevModPhys.79.1077`.

Grenier, G., C. Poirier, and J. H. Legarreta (2025). “Appendix D - Spherical harmonics”. In: *Handbook of Diffusion MR Tractography*. Ed. by F. Dell’Acqua, M. Descoteaux, and A. Leemans. Academic Press, pp. 711–715. DOI: `10.1016/B978-0-12-818894-1.09994-8`.

Grover, V. P. B., J. M. Tognarelli, M. M. E. Crossey, I. J. Cox, S. D. Taylor-Robinson, and M. J. W. McPhail (2015). “Magnetic Resonance Imaging: Principles and Techniques: Lessons for Clinicians”. In: *Journal of Clinical and Experimental Hepatology* 5.3, pp. 246–255.

Haehn, D., L. Franke, F. Zhang, S. Cetin-Karayumak, S. Pieper, L. J. O’Donnell, and Y. Rathi (2020). “TRAKO: Efficient Transmission of Tractography Data for Visualization”. In: *Medical Image Computing and Computer Assisted Intervention – MICCAI 2020*. Ed. by A. L. Martel, P. Abolmaesumi, D. Stoyanov, D. Mateus, M. A. Zuluaga, S. K. Zhou, D. Racoceanu, and L. Joskowicz. Cham: Springer International Publishing, pp. 322–332. DOI: `10.1007/978-3-030-59728-3_32`.

Hagmann, P., J.-P. Thiran, L. Jonasson, P. Vandergheynst, S. Clarke, P. Maeder, and R. Meuli (2003). “DTI mapping of human brain connectivity: statistical fibre tracking and virtual dissection”. In: *NeuroImage* 19.3, pp. 545–554. DOI: `10.1016/S1053-8119(03)00142-3`.

Hagmann, P. (2005). “From diffusion MRI to brain connectomics”. PhD thesis. Lausanne: EPFL. DOI: `10.5075/epfl-thesis-3230`.

Hagmann, P., L. Cammoun, X. Gigandet, R. Meuli, C. J. Honey, V. J. Wedeen, and O. Sporns (2008). “Mapping the Structural Core of Human Cerebral

Cortex”. In: *PLOS Biology* 6.7, pp. 1–15. DOI: `10.1371/journal.pbio.0060159`.

Hagmann, P., M. Kurant, X. Gigandet, P. Thiran, V. J. Wedeen, R. Meuli, and J.-P. Thiran (2007). “Mapping Human Whole-Brain Structural Networks with Diffusion MRI”. In: *PLOS ONE* 2.7, pp. 1–9. DOI: `10.1371/journal.pone.0000597`.

Hahn, E. L. (1950). “Spin Echoes”. In: *Phys. Rev.* 80 (4), pp. 580–594. DOI: `10.1103/PhysRev.80.580`.

Hofman, M. A. (2014). “Evolution of the human brain: when bigger is better”. In: *Frontiers in neuroanatomy* 8, p. 15. DOI: `10.3389/fnana.2014.00015`.

Hubbard, P. L. and G. J. Parker (2014). “Chapter 20 - Validation of Tractography”. In: *Diffusion MRI (Second Edition)*. Ed. by H. Johansen-Berg and T. E. Behrens. Second Edition. San Diego: Academic Press, pp. 453–480. DOI: `10.1016/B978-0-12-396460-1.00020-2`.

Iglesias, J. E., K. Van Leemput, P. Bhatt, C. Casillas, S. Dutt, N. Schuff, D. Truran-Sacrey, A. Boxer, and B. Fischl (2015). “Bayesian segmentation of brainstem structures in MRI”. In: *NeuroImage* 113, pp. 184–195. DOI: `10.1016/j.neuroimage.2015.02.065`.

Jbabdi, S., P. Bellec, R. Toro, J. Daunizeau, M. Pélégrini-Issac, and H. Benali (2008). “Accurate Anisotropic Fast Marching for Diffusion-Based Geodesic Tractography”. In: *International Journal of Biomedical Imaging* 2008.1, p. 320195. DOI: `10.1155/2008/320195`.

Jbabdi, S. and H. Johansen-Berg (2011). “Tractography: Where Do We Go from Here?” In: *Brain Connectivity* 1.3. PMID: 22433046, pp. 169–183. DOI: `10.1089/brain.2011.0033`.

Jelescu, I. O., M. Zurek, K. V. Winters, J. Veraart, A. Rajaratnam, N. S. Kim, J. S. Babb, T. M. Shepherd, D. S. Novikov, S. G. Kim, and E. Fieremans (2016). “In vivo quantification of demyelination and recovery using compartment-specific diffusion MRI metrics validated by electron microscopy”. In: *NeuroImage* 132, pp. 104–114. DOI: `10.1016/j.neuroimage.2016.02.004`.

Jenkinson, M., P. Bannister, M. Brady, and S. Smith (2002). “Improved Optimization for the Robust and Accurate Linear Registration and Motion

Correction of Brain Images". In: *NeuroImage* 17.2, pp. 825–841. DOI: 10.1006/nimg.2002.1132.

Jeurissen, B., M. Descoteaux, S. Mori, and A. Leemans (2019). "Diffusion MRI fiber tractography of the brain". In: *NMR in Biomedicine* 32.4. e3785 NBM-17-0045.R2, e3785. DOI: 10.1002/nbm.3785.

Jeurissen, B., A. Leemans, J.-D. Tournier, D. K. Jones, and J. Sijbers (2013). "Investigating the prevalence of complex fiber configurations in white matter tissue with diffusion magnetic resonance imaging". In: *Human Brain Mapping* 34.11, pp. 2747–2766. DOI: 10.1002/hbm.22099.

Jeurissen, B., J.-D. Tournier, T. Dhollander, A. Connelly, and J. Sijbers (2014). "Multi-tissue constrained spherical deconvolution for improved analysis of multi-shell diffusion MRI data". In: *NeuroImage* 103, pp. 411–426. DOI: 10.1016/j.neuroimage.2014.07.061.

Jones, D. K. (2010a). "Challenges and limitations of quantifying brain connectivity in vivo with diffusion MRI". In: *Imaging in Medicine* 2.3. Cited by: 260, pp. 341–355. DOI: 10.2217/iim.10.21.

Jones, D. K., T. R. Knösche, and R. Turner (2013). "White matter integrity, fiber count, and other fallacies: The do's and don'ts of diffusion MRI". In: *NeuroImage* 73, pp. 239–254. DOI: 10.1016/j.neuroimage.2012.06.081.

Jones PhD, D. K. (2010b). *Diffusion MRI: Theory, Methods, and Applications*. Oxford University Press. DOI: 10.1093/med/9780195369779.001.0001.

Kaden, E., T. R. Knösche, and A. Anwander (2007). "Parametric spherical deconvolution: Inferring anatomical connectivity using diffusion MR imaging". In: *NeuroImage* 37.2, pp. 474–488. DOI: 10.1016/j.neuroimage.2007.05.012.

Kaden, E., F. Kruggel, and D. C. Alexander (2016). "Quantitative mapping of the per-axon diffusion coefficients in brain white matter". In: *Magnetic Resonance in Medicine* 75.4, pp. 1752–1763. DOI: 10.1002/mrm.25734.

Kreher, B., I. Mader, and V. Kiselev (2008). "Gibbs tracking: A novel approach for the reconstruction of neuronal pathways". In: *Magnetic Resonance in Medicine* 60.4, pp. 953–963. DOI: 10.1002/mrm.21749.

Lauterbur, P. C. (1973). "Image Formation by Induced Local Interactions: Examples Employing Nuclear Magnetic Resonance". In: *Nature* 242.5394, pp. 190–191.

Le Bihan, D., E. Breton, D. Lallemand, P. Grenier, E. Cabanis, and M. Laval-Jeantet (1986). "MR imaging of intravoxel incoherent motions: application to diffusion and perfusion in neurologic disorders." In: *Radiology* 161.2. PMID: 3763909, pp. 401–407. DOI: `10.1148/radiology.161.2.3763909`.

Le Bihan, D. (1991). "Molecular diffusion nuclear magnetic resonance imaging." In: *Magnetic resonance quarterly* 7.1, pp. 1–30.

Leemans, A., F. Dell'Acqua, and M. Descoteaux (2025). "Chapter 13 - Deterministic fiber tractography". In: *Handbook of Diffusion MR Tractography*. Ed. by F. Dell'Acqua, M. Descoteaux, and A. Leemans. Academic Press, pp. 241–255. DOI: `10.1016/B978-0-12-818894-1.00029-X`.

Maffei, C., G. Girard, K. G. Schilling, D. B. Aydogan, N. Adluru, A. Zhylka, Y. Wu, M. Mancini, A. Hamamci, A. Sarica, A. Teillac, S. H. Baete, D. Karimi, F.-C. Yeh, M. E. Yildiz, A. Gholipour, Y. Bihan-Poudec, B. Hiba, A. Quattrone, A. Quattrone, T. Boshkovski, N. Stikov, P.-T. Yap, A. de Luca, J. Pluim, A. Leemans, V. Prabhakaran, B. B. Bendlin, A. L. Alexander, B. A. Landman, E. J. Canales-Rodríguez, M. Barakovic, J. Rafael-Patino, T. Yu, G. Rensonnet, S. Schiavi, A. Daducci, M. Pizzolato, E. Fischi-Gomez, J.-P. Thiran, G. Dai, G. Grisot, N. Lazovski, S. Puch, M. Ramos, P. Rodrigues, V. Prčkovska, R. Jones, J. Lehman, S. N. Haber, and A. Yendiki (2022). "Insights from the IronTract challenge: Optimal methods for mapping brain pathways from multi-shell diffusion MRI". In: *NeuroImage* 257, p. 119327. DOI: `10.1016/j.neuroimage.2022.119327`.

Maier-Hein, K. H., P. F. Neher, J.-C. Houde, M.-A. Côté, E. Garyfallidis, J. Zhong, M. Chamberland, F.-C. Yeh, Y.-C. Lin, Q. Ji, W. E. Reddick, J. O. Glass, D. Q. Chen, Y. Feng, C. Gao, Y. Wu, J. Ma, R. He, Q. Li, C.-F. Westin, S. Deslauriers-Gauthier, J. O. O. González, M. Paquette, S. St-Jean, G. Girard, F. Rheault, J. Sidhu, C. M. W. Tax, F. Guo, H. Y. Mesri, S. Dávid, M. Froeling, A. M. Heemskerk, A. Leemans, A. Boré, B. Pinsard, C. Bedetti, M. Desrosiers, S. Brambati, J. Doyon, A. Sarica, R. Vasta, A. Cerasa, A. Quattrone, J. Yeatman, A. R. Khan, W. Hodges,

S. Alexander, D. Romascano, M. Barakovic, A. Auría, O. Esteban, A. Lemkaddem, J.-P. Thiran, H. E. Cetingul, B. L. Odry, B. Mailhe, M. S. Nadar, F. Pizzagalli, G. Prasad, J. E. Villalon-Reina, J. Galvis, P. M. Thompson, F. D. S. Requejo, P. L. Laguna, L. M. Lacerda, R. Barrett, F. Dell'Acqua, M. Catani, L. Petit, E. Caruyer, A. Daducci, T. B. Dyrby, T. Holland-Letz, C. C. Hilgetag, B. Stieltjes, and M. Descoteaux (2017). "The challenge of mapping the human connectome based on diffusion tractography". In: *Nature Communications* 8.1, p. 1349.

Mangin, J.-F., P. Fillard, Y. Cointepas, D. Le Bihan, V. Frouin, and C. Poupon (2013). "Toward global tractography". In: *NeuroImage* 80. Mapping the Connectome, pp. 290–296. DOI: `10.1016/j.neuroimage.2013.04.009`.

Mangin, J.-F., C. Poupon, Y. Cointepas, D. Rivière, D. Papadopoulos-Orfanos, C. A. Clark, J. Régis, and D. Le Bihan (2002). "A framework based on spin glass models for the inference of anatomical connectivity from diffusion-weighted MR data – a technical review". In: *NMR in Biomedicine* 15.7-8, pp. 481–492. DOI: `10.1002/nbm.780`.

Mansfield, P. (1977). "Multi-planar image formation using NMR spin echoes". In: *Journal of Physics C: Solid State Physics* 10.3, p. L55. DOI: `10.1088/0022-3719/10/3/004`.

Mansour L, S., C. Seguin, R. E. Smith, and A. Zalesky (2022). "Connectome spatial smoothing (CSS): Concepts, methods, and evaluation". In: *NeuroImage* 250, p. 118930. DOI: `10.1016/j.neuroimage.2022.118930`.

Mansour L., S., M. A. Di Biase, R. E. Smith, A. Zalesky, and C. Seguin (2023). "Connectomes for 40,000 UK Biobank participants: A multi-modal, multi-scale brain network resource". In: *NeuroImage* 283, p. 120407. DOI: `10.1016/j.neuroimage.2023.120407`.

Mari, G., M. Mattocchio, S. Bosticardo, I. Gabusi, and A. Daducci (2025). "COMMITpro: accurate modeling of diffuse axonal fiber degeneration using the Discrete Cosine Transform". In: *Proceedings of the ISMRM Annual Meeting*.

Meinshausen, N. (2007). "Relaxed Lasso". In: *Computational Statistics & Data Analysis* 52.1, pp. 374–393. DOI: `10.1016/j.csda.2006.12.019`.

Messaritaki, E., S. I. Dimitriadis, and D. K. Jones (2019). “Optimization of graph construction can significantly increase the power of structural brain network studies”. In: *NeuroImage* 199, pp. 495–511. DOI: `10.1016/j.neuroimage.2019.05.052`.

Mienye, I. D. and Y. Sun (2022). “A Survey of Ensemble Learning: Concepts, Algorithms, Applications, and Prospects”. In: *IEEE Access* 10, pp. 99129–99149. DOI: `10.1109/ACCESS.2022.3207287`.

Miller, K. L., F. Alfaro-Almagro, N. K. Bangerter, D. L. Thomas, E. Yacoub, J. Xu, A. J. Bartsch, S. Jbabdi, S. N. Sotiropoulos, J. L. Andersson, et al. (2016). “Multimodal population brain imaging in the UK Biobank prospective epidemiological study”. In: *Nature neuroscience* 19.11, pp. 1523–1536. DOI: `10.1038/nn.4393`.

Mori, S., B. J. Crain, V. P. Chacko, and P. C. M. Van Zijl (1999). “Three-dimensional tracking of axonal projections in the brain by magnetic resonance imaging”. In: *Annals of Neurology* 45.2, pp. 265–269. DOI: `10.1002/1531-8249(199902)45:2<265::AID-ANA21>3.0.CO;2-3`.

Mori, S. and J.-D. Tournier (2014). “Chapter 8 - Moving Beyond DTI: High Angular Resolution Diffusion Imaging (HARDI)”. In: *Introduction to Diffusion Tensor Imaging (Second Edition)*. Ed. by S. Mori and J.-D. Tournier. Second Edition. San Diego: Academic Press, pp. 65–78. DOI: `10.1016/B978-0-12-398398-5.00008-4`.

Moyer, D., B. A. Gutman, J. Faskowitz, N. Jahanshad, and P. M. Thompson (2017). “Continuous representations of brain connectivity using spatial point processes”. In: *Medical Image Analysis* 41. Special Issue on the 2016 Conference on Medical Image Computing and Computer Assisted Intervention (Analog to MICCAI 2015), pp. 32–39. DOI: `10.1016/j.media.2017.04.013`.

Moyer, D. C., P. Thompson, and G. V. Steeg (2019). “Measures of Tractography Convergence”. In: *Computational Diffusion MRI, International Medical Image Computing and Computer Assisted Intervention (MICCAI) workshop*. Ed. by E. Bonet-Carne, F. Grussu, L. Ning, F. Sepehrband, and C. M. W. Tax. Cham: Springer International Publishing, pp. 295–307. DOI: `10.1007/978-3-030-05831-9_23`.

Nath, V., K. G. Schilling, P. Parvathaneni, Y. Huo, J. A. Blaber, A. E. Hainline, M. Barakovic, D. Romascano, J. Rafael-Patino, M. Frigo, G. Girard, J.-P. Thiran, A. Daducci, M. Rowe, P. Rodrigues, V. Prčkovska, D. B. Aydogan, W. Sun, Y. Shi, W. A. Parker, A. A. Ould Ismail, R. Verma, R. P. Cabeen, A. W. Toga, A. T. Newton, J. Wasserthal, P. Neher, K. Maier-Hein, G. Savini, F. Palesi, E. Kaden, Y. Wu, J. He, Y. Feng, M. Paquette, F. Rheault, J. Sidhu, C. Lebel, A. Leemans, M. Descoteaux, T. B. Dyrby, H. Kang, and B. A. Landman (2020). "Tractography reproducibility challenge with empirical data (TraCED): The 2017 ISMRM diffusion study group challenge". In: *Journal of Magnetic Resonance Imaging* 51.1, pp. 234–249. DOI: `10.1002/jmri.26794`.

Neher, P., P. Poulin, D. Jörgens, M. Reisert, I. Benou, and K. Maier-Hein (2025). "Chapter 17 - Machine learning in tractography". In: *Handbook of Diffusion MR Tractography*. Ed. by F. Dell'Acqua, M. Descoteaux, and A. Leemans. Academic Press, pp. 315–345. DOI: `10.1016/B978-0-12-818894-1.00032-X`.

Novikov, D. S., E. Fieremans, S. N. Jespersen, and V. G. Kiselev (2019). "Quantifying brain microstructure with diffusion MRI: Theory and parameter estimation". In: *NMR in Biomedicine* 32.4, e3998. DOI: `10.1002/nbm.3998`.

Novikov, D. S., E. Fieremans, and H.-H. Lee (2025). "Chapter 5 - Physics of diffusion imaging: Fundamentals". In: *Handbook of Diffusion MR Tractography*. Ed. by F. Dell'Acqua, M. Descoteaux, and A. Leemans. Academic Press, pp. 77–101. DOI: `10.1016/B978-0-12-818894-1.00031-8`.

Ocampo-Pineda, M., S. Schiavi, F. Rheault, G. Girard, L. Petit, M. Descoteaux, and A. Daducci (2021). "Hierarchical Microstructure Informed Tractography". In: *Brain Connectivity* 11.2. PMID: 33512262, pp. 75–88. DOI: `10.1089/brain.2020.0907`.

St-Onge, E., A. Daducci, G. Girard, and M. Descoteaux (2018). "Surface-enhanced tractography (SET)". In: *NeuroImage* 169, pp. 524–539. DOI: `10.1016/j.neuroimage.2017.12.036`.

Panagiotaki, E., T. Schneider, B. Siow, M. G. Hall, M. F. Lythgoe, and D. C. Alexander (2012). "Compartment models of the diffusion MR signal in brain white matter: A taxonomy and comparison". In: *NeuroImage* 59.3, pp. 2241–2254. DOI: `10.1016/j.neuroimage.2011.09.081`.

Parker, G. J. M. and D. C. Alexander (2003). "Probabilistic Monte Carlo Based Mapping of Cerebral Connections Utilising Whole-Brain Crossing Fibre Information". In: *Information Processing in Medical Imaging*. Ed. by C. Taylor and J. A. Noble. Berlin, Heidelberg: Springer Berlin Heidelberg, pp. 684–695.

Parker, G. J. M., C. A. M. Wheeler-Kingshott, and G. J. Barker (2002). "Estimating distributed anatomical connectivity using fast marching methods and diffusion tensor imaging". en. In: *IEEE Trans. Med. Imaging* 21.5, pp. 505–512. DOI: `10.1109/TMI.2002.1009386`.

Persson, S. and R. Moreno (2024). "Bounding tractogram redundancy". In: *Frontiers in Neuroscience* Volume 18 - 2024. DOI: `10.3389/fnins.2024.1403804`.

Pestilli, F., J. Yeatman, A. Rokem, K. Kay, and B. Wandell (2014). "Evaluation and statistical inference for human connectomes". In: *Nature Methods*, pp. 1058–63. DOI: `10.1038/nmeth.3098`.

Pierpaoli, C., P. Jezzard, P. J. Basser, A. Barnett, and G. Di Chiro (1996). "Diffusion tensor MR imaging of the human brain." In: *Radiology* 201.3. PMID: 8939209, pp. 637–648. DOI: `10.1148/radiology.201.3.8939209`.

Poulin, P., D. Jörgens, P.-M. Jodoin, and M. Descoteaux (2019). "Tractography and machine learning: Current state and open challenges". In: *Magnetic Resonance Imaging* 64. Artificial Intelligence in MRI, pp. 37–48. DOI: `10.1016/j.mri.2019.04.013`.

Poupon, C., C. Clark, V. Frouin, J. Régis, I. Bloch, D. Le Bihan, and J.-F. Mangin (2000). "Regularization of Diffusion-Based Direction Maps for the Tracking of Brain White Matter Fascicles". In: *NeuroImage* 12.2, pp. 184–195. DOI: `10.1006/nimg.2000.0607`.

Presseau, C., P.-M. Jodoin, J.-C. Houde, and M. Descoteaux (2015). "A new compression format for fiber tracking datasets". In: *NeuroImage* 109, pp. 73–83. DOI: `10.1016/j.neuroimage.2014.12.058`.

Purves, D., G. J. Augustine, D. Fitzpatrick, W. C. Hall, A.-S. LaMantia, J. o. McNamara, and S. M. Williams, eds. (2004). *Neuroscience*. 3rd ed. Sinauer Associates.

Rabi, I. I., J. R. Zacharias, S. Millman, and P. Kusch (1938). "A New Method of Measuring Nuclear Magnetic Moment". In: *Phys. Rev.* 53 (4), pp. 318–318. DOI: `10.1103/PhysRev.53.318`.

Reid, L. B., M. I. Cespedes, and K. Pannek (2020). "How many streamlines are required for reliable probabilistic tractography? Solutions for microstructural measurements and neurosurgical planning". In: *NeuroImage* 211, p. 116646. DOI: `10.1016/j.neuroimage.2020.116646`.

Reisert, M., I. Mader, C. Anastasopoulos, M. Weigel, S. Schnell, and V. Kiselev (2011). "Global fiber reconstruction becomes practical". In: *NeuroImage* 54.2, pp. 955–962. DOI: `10.1016/j.neuroimage.2010.09.016`.

Rheault, F., H. Mayberg, M. T. de Schotten, A. Roebroeck, and S. J. Forkel (2025a). "The scientific value of tractography: accuracy vs usefulness". In: *Brain Structure and Function* 230.4, p. 59. DOI: `10.1007/s00429-025-02921-9`.

Rheault, F., P. Poulin, A. V. Caron, E. St-Onge, and M. Descoteaux (2020). "Common misconceptions, hidden biases and modern challenges of dMRI tractography". In: *Journal of Neural Engineering* 17.1, p. 011001. DOI: `10.1088/1741-2552/ab6aad`.

Rheault, F., P. Poulin, A. V. Caron, E. St-Onge, K. G. Schilling, L. Petit, F. Dell'Acqua, A. Leemans, and M. Descoteaux (2025b). "Chapter 28 - Current challenges and opportunities for tractography". In: *Handbook of Diffusion MR Tractography*. Ed. by F. Dell'Acqua, M. Descoteaux, and A. Leemans. Academic Press, pp. 565–580. DOI: `10.1016/B978-0-12-818894-1.00037-9`.

Rheault, F., P. Poulin, A. V. Caron, E. St-Onge, K. G. Schilling, L. Petit, F. Dell'Acqua, A. Leemans, and M. Descoteaux (2025c). "Chapter 28 - Current challenges and opportunities for tractography". In: *Handbook of Diffusion MR Tractography*. Ed. by F. Dell'Acqua, M. Descoteaux, and A. Leemans. Academic Press, pp. 565–580. DOI: `10.1016/B978-0-12-818894-1.00037-9`.

Rheault, F., K. G. Schilling, A. Valcourt-Caron, A. Théberge, C. Poirier, G. Grenier, G. I. Guberman, J. Begnoche, J. H. Legarreta, L. Y. Cai, M. Roy, M. Edde, M. P. Caceres, M. Ocampo-Pineda, N. Al-Sharif, P. Karan, P. Bontempi, S. Obaid, S. Bosticardo, S. Schiavi, V. Sairanen, A. Daducci, L. E. Cutting, L. Petit, M. Descoteaux, and B. A. Landman (2022). "Tractostorm 2: Optimizing tractography dissection reproducibility with segmentation protocol dissemination". In: *Human Brain Mapping* 43.7, pp. 2134–2147. DOI: `10.1002/hbm.25777`.

Roberts, J. (1959). "Nuclear magnetic resonance: Applications to Organic Chemistry". In: *McGraw-Hill Series in Advanced Chemistry*.

Rockland, K. S. (2002). "Axon". In: *Encyclopedia of the Human Brain*. Ed. by V. Ramachandran. New York: Academic Press, pp. 349–365. DOI: `10.1016/B0-12-227210-2/00051-0`.

Roine, T., B. Jeurissen, D. Perrone, J. Aelterman, W. Philips, J. Sijbers, and A. Leemans (2019). "Reproducibility and intercorrelation of graph theoretical measures in structural brain connectivity networks". In: *Medical Image Analysis* 52, pp. 56–67. DOI: `10.1016/j.media.2018.10.009`.

Sagi, O. and L. Rokach (2018). "Ensemble learning: A survey". In: *WIREs Data Mining and Knowledge Discovery* 8.4, e1249. DOI: `10.1002/widm.1249`.

Schiavi, S., P.-J. Lu, M. Weigel, A. Lutti, D. K. Jones, L. Kappos, C. Granziera, and A. Daducci (2022). "Bundle myelin fraction (BMF) mapping of different white matter connections using microstructure informed tractography". In: *NeuroImage* 249, p. 118922. DOI: `10.1016/j.neuroimage.2022.118922`.

Schiavi, S., M. Ocampo-Pineda, M. Barakovic, L. Petit, M. Descoteaux, J.-P. Thiran, and A. Daducci (2020). "A new method for accurate in vivo mapping of human brain connections using microstructural and anatomical information". In: *Science Advances* 6.31, eaba8245. DOI: `10.1126/sciadv.aba8245`.

Schilling, K., Y. Gao, V. Janve, I. Stepniewska, B. A. Landman, and A. W. Anderson (2018). "Confirmation of a gyral bias in diffusion MRI fiber tractography". In: *Human Brain Mapping* 39.3, pp. 1449–1466. DOI: `10.1002/hbm.23936`.

Schilling, K. G., D. Archer, F.-C. Yeh, F. Rheault, L. Y. Cai, C. Hansen, Q. Yang, K. Ramdass, A. T. Shafer, S. M. Resnick, et al. (2022a). "Aging and white matter microstructure and macrostructure: a longitudinal multi-site diffusion MRI study of 1218 participants". In: *Brain Structure and Function* 227.6, pp. 2111–2125. DOI: 10.1007/s00429-022-02503-z.

Schilling, K. G., A. Daducci, K. Maier-Hein, C. Poupon, J.-C. Houde, V. Nath, A. W. Anderson, B. A. Landman, and M. Descoteaux (2019a). "Challenges in diffusion MRI tractography – Lessons learned from international benchmark competitions". In: *Magnetic Resonance Imaging* 57, pp. 194–209. DOI: 10.1016/j.mri.2018.11.014.

Schilling, K. G., V. Nath, C. Hansen, P. Parvathaneni, J. Blaber, Y. Gao, P. Neher, D. B. Aydogan, Y. Shi, M. Ocampo-Pineda, S. Schiavi, A. Daducci, G. Girard, M. Barakovic, J. Rafael-Patino, D. Romascano, G. Rensonnet, M. Pizzolato, A. Bates, E. Fischi, J.-P. Thiran, E. J. Canales-Rodríguez, C. Huang, H. Zhu, L. Zhong, R. Cabeen, A. W. Toga, F. Rheault, G. Theaud, J.-C. Houde, J. Sidhu, M. Chamberland, C.-F. Westin, T. B. Dyrby, R. Verma, Y. Rathi, M. O. Irfanoglu, C. Thomas, C. Pierpaoli, M. Descoteaux, A. W. Anderson, and B. A. Landman (2019b). "Limits to anatomical accuracy of diffusion tractography using modern approaches". In: *NeuroImage* 185, pp. 1–11. DOI: 10.1016/j.neuroimage.2018.10.029.

Schilling, K. G., F. Rheault, and T. B. Dyrby (2025). "Chapter 27 - Tractography validation part 3: Lessons learned through validation studies". In: *Handbook of Diffusion MR Tractography*. Ed. by F. Dell'Acqua, M. Descoteaux, and A. Leemans. Academic Press, pp. 543–564. DOI: 10.1016/B978-0-12-818894-1.00004-5.

Schilling, K. G., C. M. W. Tax, F. Rheault, B. A. Landman, A. W. Anderson, M. Descoteaux, and L. Petit (2022b). "Prevalence of white matter pathways coming into a single white matter voxel orientation: The bottleneck issue in tractography". In: *Human Brain Mapping* 43.4, pp. 1196–1213. DOI: 10.1002/hbm.25697.

Schilling, K. G. et al. (2021). "Tractography dissection variability: What happens when 42 groups dissect 14 white matter bundles on the same dataset?" In: *NeuroImage* 243, p. 118502. DOI: `10.1016/j.neuroimage.2021.118502`.

Sengers, R., L. Florack, and A. Fuster (2021). "Geodesic Uncertainty in Diffusion MRI". In: *Frontiers in Computer Science* Volume 3 - 2021. DOI: `10.3389/fcomp.2021.718131`.

Seunarine, K. K. and D. C. Alexander (2014). "Chapter 6 - Multiple Fibers: Beyond the Diffusion Tensor". In: *Diffusion MRI (Second Edition)*. Ed. by H. Johansen-Berg and T. E. Behrens. Second Edition. San Diego: Academic Press, pp. 105–123. DOI: `10.1016/B978-0-12-396460-1.00006-8`.

Shaffer, J. J., M. Mani, S. L. Schmitz, J. Xu, N. Owusu, D. Wu, V. A. Magnotta, and J. A. Wemmie (2020). "Proton Exchange Magnetic Resonance Imaging: Current and Future Applications in Psychiatric Research". In: *Frontiers in Psychiatry* Volume 11 - 2020. DOI: `10.3389/fpsyt.2020.532606`.

Siless, V., K. Chang, B. Fischl, and A. Yendiki (2018). "AnatomiCuts: Hierarchical clustering of tractography streamlines based on anatomical similarity". In: *NeuroImage* 166, pp. 32–45. DOI: `10.1016/j.neuroimage.2017.10.058`.

Sinke, M. R., W. M. Otte, D. Christiaens, O. Schmitt, A. Leemans, A. van der Toorn, R. A. Sarabdjitsingh, M. Joëls, and R. M. Dijkhuizen (2018). "Diffusion MRI-based cortical connectome reconstruction: dependency on tractography procedures and neuroanatomical characteristics". In: *Brain Structure and Function* 223.5, pp. 2269–2285. DOI: `10.1007/s00429-018-1628-y`.

Smith, R. E., D. Raffelt, J.-D. Tournier, and A. Connelly (2022). "Quantitative streamlines tractography: methods and inter-subject normalisation". In: *Aperture Neuro* 2, pp. 1–25. DOI: `10.52294/ApertureNeuro.2022.2.NEOD9565`.

Smith, R. E., J.-D. Tournier, F. Calamante, and A. Connelly (2012). "Anatomically-constrained tractography: Improved diffusion MRI streamlines tractography through effective use of anatomical information". In: *NeuroImage* 62.3, pp. 1924–1938. DOI: `10.1016/j.neuroimage.2012.06.005`.

Smith, R. E., J.-D. Tournier, F. Calamante, and A. Connelly (2013). “SIFT: Spherical-deconvolution informed filtering of tractograms”. In: *NeuroImage* 67, pp. 298–312. DOI: `10.1016/j.neuroimage.2012.11.049`.

Smith, R. E., J.-D. Tournier, F. Calamante, and A. Connelly (2015a). “SIFT2: Enabling dense quantitative assessment of brain white matter connectivity using streamlines tractography”. In: *NeuroImage* 119, pp. 338–351. DOI: `10.1016/j.neuroimage.2015.06.092`.

Smith, R. E., J.-D. Tournier, F. Calamante, and A. Connelly (2015b). “The effects of SIFT on the reproducibility and biological accuracy of the structural connectome”. In: *NeuroImage* 104, pp. 253–265. DOI: `10.1016/j.neuroimage.2014.10.004`.

Sotiropoulos, S. N. and A. Zalesky (2019). “Building connectomes using diffusion MRI: why, how and but”. In: *NMR in Biomedicine* 32.4. e3752 NBM-16-0139.R1, e3752. DOI: `10.1002/nbm.3752`.

Sporns, O. (2014). “Chapter 18 - The Human Connectome: Linking Structure and Function in the Human Brain”. In: *Diffusion MRI (Second Edition)*. Ed. by H. Johansen-Berg and T. E. Behrens. Second Edition. San Diego: Academic Press, pp. 401–428. DOI: `10.1016/B978-0-12-396460-1.00018-4`.

Sporns, O., G. Tononi, and R. Kötter (2005). “The Human Connectome: A Structural Description of the Human Brain”. In: *PLOS Computational Biology* 1.4, null. DOI: `10.1371/journal.pcbi.0010042`.

Stejskal, E. O. and J. E. Tanner (1965). “Spin Diffusion Measurements: Spin Echoes in the Presence of a Time-Dependent Field Gradient”. In: *The Journal of Chemical Physics* 42.1, pp. 288–292. DOI: `10.1063/1.1695690`.

Strang, G. (1980). *Linear Algebra and its Applications*. Second Edition. Academic Press.

Takemura, H., C. F. Caiafa, B. A. Wandell, and F. Pestilli (2016). “Ensemble Tractography”. In: *PLOS Computational Biology* 12.2, pp. 1–22. DOI: `10.1371/journal.pcbi.1004692`.

Thomas, C., F. Q. Ye, M. O. Irfanoglu, P. Modi, K. S. Saleem, D. A. Leopold, and C. Pierpaoli (2014). “Anatomical accuracy of brain connections derived from diffusion MRI tractography is inherently limited”. In: *Proceedings* *of the National Academy of Sciences* 111.46, pp. 16574–16579. DOI: 10.1073/pnas.1405672111.

Tournier, J.-D., F. Calamante, and A. Connelly (2007). "Robust determination of the fibre orientation distribution in diffusion MRI: Non-negativity constrained super-resolved spherical deconvolution". In: *NeuroImage* 35.4, pp. 1459–1472. DOI: 10.1016/j.neuroimage.2007.02.016.

Tournier, J.-D., F. Calamante, and A. Connelly (2012). "MRtrix: Diffusion Tractography in Crossing Fiber Regions". In: *Int. J. Imaging Syst. Technol.* 22.1, pp. 53–66. DOI: 10.1002/ima.22005.

Tournier, J. D., F. Calamante, and A. Connelly (2010). "Improved probabilistic streamlines tractography by 2nd order integration over fibre orientation distributions". In: *Proceedings of the ISMRM Annual Meeting*. Vol. 1670. John Wiley & Sons, Inc. New Jersey, USA.

Tournier, J.-D., F. Calamante, and A. Connelly (2013). "Determination of the appropriate b value and number of gradient directions for high-angular-resolution diffusion-weighted imaging". In: *NMR in Biomedicine* 26.12, pp. 1775–1786. DOI: 10.1002/nbm.3017.

Tournier, J.-D., F. Calamante, D. G. Gadian, and A. Connelly (2004). "Direct estimation of the fiber orientation density function from diffusion-weighted MRI data using spherical deconvolution". In: *NeuroImage* 23.3, pp. 1176–1185. DOI: 10.1016/j.neuroimage.2004.07.037.

Tournier, J.-D., S. Mori, and A. Leemans (2011). "Diffusion tensor imaging and beyond". In: *Magnetic Resonance in Medicine* 65.6, pp. 1532–1556. DOI: 10.1002/mrm.22924.

Tuch, D. S. (2004). "Q-ball imaging". In: *Magnetic Resonance in Medicine* 52.6, pp. 1358–1372. DOI: 10.1002/mrm.20279.

Tuch, D. S., T. G. Reese, M. R. Wiegell, N. Makris, J. W. Belliveau, and V. J. Wedeen (2002). "High angular resolution diffusion imaging reveals intravoxel white matter fiber heterogeneity". In: *Magnetic Resonance in Medicine* 48.4, pp. 577–582. DOI: 10.1002/mrm.10268.

Van Essen, D. C., S. M. Smith, D. M. Barch, T. E. Behrens, E. Yacoub, and K. Ugurbil (2013a). "The WU-Minn Human Connectome Project: An overview". In: *NeuroImage* 80. Mapping the Connectome, pp. 62–79. DOI: `10.1016/j.neuroimage.2013.05.041`.

Van Essen, D. C., S. M. Smith, D. M. Barch, T. E. Behrens, E. Yacoub, and K. Ugurbil (2013b). "The WU-Minn Human Connectome Project: An overview". In: *NeuroImage* 80. Mapping the Connectome, pp. 62–79. DOI: `10.1016/j.neuroimage.2013.05.041`.

Vázquez, A., N. López-López, A. Sánchez, J. Houenou, C. Poupon, J.-F. Mangin, C. Hernández, and P. Guevara (2020). "FFClust: Fast fiber clustering for large tractography datasets for a detailed study of brain connectivity". In: *NeuroImage* 220, p. 117070. DOI: `10.1016/j.neuroimage.2020.117070`.

Wassermann, D., L. Bloy, E. Kanterakis, R. Verma, and R. Deriche (2010). "Unsupervised white matter fiber clustering and tract probability map generation: Applications of a Gaussian process framework for white matter fibers". In: *NeuroImage* 51.1, pp. 228–241. DOI: `10.1016/j.neuroimage.2010.01.004`.

Wassermann, D., Y. Rathi, S. Bouix, M. Kubicki, R. Kikinis, M. Shenton, and C.-F. Westin (2011). "White Matter Bundle Registration and Population Analysis Based on Gaussian Processes". In: *Information Processing in Medical Imaging*. Ed. by G. Székely and H. K. Hahn. Berlin, Heidelberg: Springer Berlin Heidelberg, pp. 320–332.

Wickens, A. P. (2014). *A history of the brain: from stone age surgery to modern neuroscience*. Psychology Press.

Wycoco, V., M. Shroff, S. Sudhakar, and W. Lee (2013). "White matter anatomy: what the radiologist needs to know". In: *Neuroimaging clinics of North America* 23.2, pp. 197–216. DOI: `10.1016/j.nic.2012.12.002`.

Yeatman, J. D., R. F. Dougherty, N. J. Myall, B. A. Wandell, and H. M. Feldman (2012). "Tract Profiles of White Matter Properties: Automating Fiber-Tract Quantification". In: *PLOS ONE* 7.11, pp. 1–15. DOI: `10.1371/journal.pone.0049790`.

Yeh, C.-H., D. K. Jones, X. Liang, M. Descoteaux, and A. Connelly (2021). "Mapping Structural Connectivity Using Diffusion MRI: Challenges and

Opportunities". In: *Journal of Magnetic Resonance Imaging* 53.6, pp. 1666–1682. DOI: `10.1002/jmri.27188`.

Yeh, C.-H., R. E. Smith, T. Dhollander, F. Calamante, and A. Connelly (2019). "Connectomes from streamlines tractography: Assigning streamlines to brain parcellations is not trivial but highly consequential". In: *NeuroImage* 199, pp. 160–171. DOI: `10.1016/j.neuroimage.2019.05.005`.

Zalesky, A. (2008). "DT-MRI fiber tracking: a shortest paths approach". en. In: *IEEE Trans. Med. Imaging* 27.10, pp. 1458–1471. DOI: `10.1109/TMI.2008.923644`.

Zalesky, A., A. Fornito, L. Cocchi, L. L. Gollo, M. P. van den Heuvel, and M. Breakspear (2016). "Connectome sensitivity or specificity: which is more important?" In: *NeuroImage* 142, pp. 407–420. DOI: `10.1016/j.neuroimage.2016.06.035`.

Zalesky, A., T. Sarwar, and K. Ramamohanarao (2020). "A cautionary note on the use of SIFT in pathological connectomes". In: *Magnetic Resonance in Medicine* 83.3, pp. 791–794. DOI: `10.1002/mrm.28037`.

Zalesky, A., S. N. Sotiropoulos, S. Jbabdi, and A. Fornito (2025). "Chapter 24 - Connectivity and connectomics". In: *Handbook of Diffusion MR Tractography*. Ed. by F. Dell'Acqua, M. Descoteaux, and A. Leemans. Academic Press, pp. 451–484. DOI: `10.1016/B978-0-12-818894-1.00007-0`.

Zhang, F., S. Cetin Karayumak, N. Hoffmann, Y. Rathi, A. J. Golby, and L. J. O'Donnell (2020). "Deep white matter analysis (DeepWMA): Fast and consistent tractography segmentation". In: *Medical Image Analysis* 65, p. 101761. DOI: `10.1016/j.media.2020.101761`.

Zhang, F., A. Daducci, Y. He, S. Schiavi, C. Seguin, R. E. Smith, C.-H. Yeh, T. Zhao, and L. J. O'Donnell (2022). "Quantitative mapping of the brain's structural connectivity using diffusion MRI tractography: A review". In: *NeuroImage* 249, p. 118870. DOI: `10.1016/j.neuroimage.2021.118870`.

Zhang, H., T. Schneider, C. A. Wheeler-Kingshott, and D. C. Alexander (2012). "NODDI: Practical in vivo neurite orientation dispersion and density imaging of the human brain". In: *NeuroImage* 61.4, pp. 1000–1016. DOI: `10.1016/j.neuroimage.2012.03.072`.